SPECTRAL AND SPATIAL CONTROL OF BROADBAND LIGHT USING WAVEFRONT SHAPING

A THESIS SUBMITTED TO
THE GRADUATE SCHOOL OF NATURAL AND APPLIED SCIENCES
OF
MIDDLE EAST TECHNICAL UNIVERSITY

BY

ALİM YOLALMAZ

IN PARTIAL FULFILLMENT OF THE REQUIREMENTS
FOR
THE DEGREE OF DOCTOR OF PHILOSOPHY
IN
MICRO AND NANOTECHNOLOGY

FEBRUARY 2022

Approval of the thesis:

SPECTRAL AND SPATIAL CONTROL OF BROADBAND LIGHT USING WAVEFRONT SHAPING

submitted by **ALİM YOLALMAZ** in partial fulfillment of the requirements for the degree of **Doctor of Philosophy in Micro and Nanotechnology Department, Middle East Technical University** by,

Prof. Dr. Halil Kalıpçılar
Dean, Graduate School of **Natural and Applied Sciences** _______________

Prof. Dr. Deniz Üner
Head of Department, **Micro and Nanotechnology** _______________

Assoc. Prof. Dr. Emre Yüce
Supervisor, **Micro and Nanotechnology, METU** _______________

Assoc. Prof. Dr. Selçuk Yerci
Co-supervisor, **Electrical and Electronics Engineering, METU** _______________

Examining Committee Members:

Prof. Dr. Alper Kiraz
Electrical and Electronics Engineering, Koç University _______________

Assoc. Prof. Dr. Emre Yüce
Micro and Nanotechnology, METU _______________

Prof. Dr. Hakan Altan
Physics, METU _______________

Assoc. Prof. Dr. Alpan Bek
Physics, METU _______________

Assist. Prof. Dr. Hasan Yılmaz
National Nanotechnology Research Center, Bilkent University _______________

Date: 09/02/2022

I hereby declare that all information in this document has been obtained and presented in accordance with academic rules and ethical conduct. I also declare that, as required by these rules and conduct, I have fully cited and referenced all material and results that are not original to this work.

Name, Surname: Alim Yolalmaz

Signature :

ABSTRACT

SPECTRAL AND SPATIAL CONTROL OF BROADBAND LIGHT USING WAVEFRONT SHAPING

Yolalmaz, Alim
Ph.D., Department of Micro and Nanotechnology
Supervisor: Assoc. Prof. Dr. Emre Yüce
Co-Supervisor: Assoc. Prof. Dr. Selçuk Yerci

February 2022, 131 pages

Spectral and spatial control of light strongly influences central fields such as solar energy, spectroscopy, holography, and imaging. Enhanced control of propagation, diffraction, scattering, and interference of light using micro-and nano-structures leads to superior performance in these fields. This thesis presents light control in spectral and spatial domains using wavefront control for solar energy, spectroscopy, holography, and imaging applications.

Spectral splitting of the sunlight using diffractive optical elements (DOEs) is an effective method to increase the amount of converted solar energy. In this thesis, we design phase-only DOEs by using an iterative optimization algorithm to spectrally split and simultaneously concentrate the solar spectrum. We introduce the effective bandwidth approach, which reduces the computational time of DOEs from 89 days to 8 days while preserving the spectral splitting efficiency. Using our effective bandwidth method, we manage to spectrally split light into two separate bands between 400 nm - 700 nm and 701 nm - 1100 nm, with splitting efficiencies of 56% and 63%, respectively.

Next, we present a hybrid design scheme, which relies on a deep learning model, the DOENet, and the local search optimization algorithm, to optimize a DOE that performs spectral splitting and spatial concentration of broadband light for solar cells. Our hybrid design approach both speeds up optimization of DOEs as well as provides better performance, at least 57% excess light concentration with spectral splitting.

Here, we also design DOEs that concentrate and split the broadband light for angled illumination to minimize the variation of intensity on the targets when the angle of incident light changes leading to a decrease in the intensity of light for solar cells applications. We observe that spectral splitting of the broadband light with a DOE is less sensitive to variation of incident angle of the solar radiation once the DOE optimization is performed for the area which is half of the output plane. What's interesting is that less than 0.6% deviation in output intensity can be observed when a single DOE is illuminated at an angle that spans from 0 to 80 degrees.

Then, we develop a neural network model to experimentally design and validate SpliCons, a special type of diffractive optical element that can achieve spectral splitting and simultaneous concentration of broadband light. Our results show that the neural network model, the SpliConNet, yields enhanced spectral splitting performance for the SpliCons with quantitative assessment compared to the SpliCons that are optimized via the local search optimization algorithm. The capabilities of the SpliCons optimized via the neural network are experimentally validated by comparing the intensity distribution at the output plane. Once the neural networks are trained, we manage to design the SpliCons with $96.6 \pm 2.3\%$ accuracy within 2 seconds, which is orders of magnitude faster than iterative search algorithms.

Later, we present a DOE spectrometer design that performs spectral decomposition of the broadband light. Compared to an optical spectrometer constructed with a single prism or a diffraction grating, our DOE spectrometer consists of many DOEs which are designed for each wavelength of light and are placed on a moving part. With the moving part, the position of each DOE is altered to obtain desired spectral light from the broadband light. Each DOE in the DOE spectrometer splits the broadband light into a specific wavelength of light, so our DOE spectrometer operates under broadband light compared to conventional spectrometers. We believe that the DOE

spectrometer will yield high throughput thanks to a single wavelength-based DOE design.

We also focus on designing optical holograms to generate holographic images at multiple observation planes and colors via a deep learning model, the CHoLoNet. The CHoLoNet produces optical holograms, which show multitasking performance as multiplexing color holographic image planes by tuning holographic structures. Furthermore, our deep learning model retrieves an object/hologram information from an intensity holographic image without requiring phase and amplitude information from the intensity image. We see that reconstructed objects/holograms show excellent agreement with the ground-truth objects/holograms.

Keywords: Wavefront shaping, holography, imaging, deep learning, solar energy, spectroscopy, computer-generated hologram, diffractive optical element, spectral splitting, neural network, artificial intelligence.

ÖZ

DALGA ÖNÜ ŞEKİLLENDİRME İLE GENİŞ BANT IŞIĞIN SPEKTRAL VE UZAYSAL KONTROLÜ

Yolalmaz, Alim
Doktora, Mikro ve Nanoteknoloji Bölümü
Tez Yöneticisi: Doç. Dr. Emre Yüce
Ortak Tez Yöneticisi: Doç. Dr. Selçuk Yerci

Şubat 2022, 131 sayfa

Işığın spektral ve uzaysal kontrolü, güneş enerjisi, spektroskopi, holografi ve görüntüleme gibi dikkat çeken bilimsel alanları önemli ölçüde etkilemektedir. Mikro ve nano yapılar kullanılarak ışığın ilerlemesinin, kırınımının, saçılmasının ve girişiminin gelişmiş kontrolü, bu alanlarda üstün performans elde edilmesini sağlar. Bu tezde, güneş enerjisi, spektroskopi, holografi ve görüntüleme uygulamaları için dalga önü kontrol edilerek ışığın hem spektral hem de uzaysal kontrolünü sunuyoruz.

Kırınım optik elemanları (KOE'ları) kullanılarak güneş ışığının spektral bölünmesi, güneşten elde edilen enerji miktarını artırmak için etkili bir yöntemdir. Bu tezde, güneş spektrumunu spektral olarak bölmek ve aynı anda odaklamak için yinelemeli bir optimizasyon algoritması kullanarak sadece ışığın fazını kontrol eden KOE'ları tasarlıyoruz. Spektral bölme verimliliğini korurken KOE'larının hesaplama süresini 89 günden 8 güne indiren etkin bant genişliği yaklaşımı sunuyoruz. Etkin bant genişliği yöntemimizi kullanarak ışığı spektral olarak 400 nm - 700 nm ve 701 nm - 1100 nm arasında, sırasıyla %56 ve %63 ayırma verimleriyle iki ayrı banda ayırmayı başarıyo-

ruz.

Ayrıca, güneş pilleri için geniş bant ışığın spektral bölünmesini ve uzaysal konsantrasyonunu gerçekleştiren bir KOE'ı optimize etmek için bir derin öğrenme modeline, DOENet'e ve yerel arama optimizasyon algoritmasına dayanan bir hibrit tasarım algoritması sunuyoruz. Hibrit algoritmamız hem KOE'larının optimizasyonunu hızlandırıyor hem de spektral bölme ile %57'den daha fazla ışığın konsantrasyonunu sağlıyor.

Işığın geliş açısının değişimi elektriğe dönüşen güneş enerjisi miktarında azalmaya neden olmaktadır. Bu etkiyi azaltmak için bu tezde geniş bant ışığı odaklamak ve spektral bölmek için KOE'ları tasarlıyoruz. Çıkış düzleminin yarısı olan alan için KOE'ı tasarımı yapıldığında, geniş bant ışığın spektral bölünmesinin güneş ışığının geliş açısındaki değişime daha az duyarlı olduğunu gözlemliyoruz. İlginç olan ise, ışığın geliş açısı 0 ile 80 derecelik bir açı aralığında değişmesine rağmen tek bir KOE'ı hedef ekranda ışığın şiddetinde %0,6'dan daha az sapma göstermektedir.

Bu tezde ayrıca geniş bant ışığı spektral ayırmak ve aynı zamanda odaklamak için özel bir kırınım optik eleman türü olan SpliCons'u deneysel olarak tasarlamak ve doğrulamak için bir sinir ağı modeli geliştirdik. Sonuçlarımız, sinir ağı modeli olan SpliConNet ile tasarlanmış SpliCon'ların, yerel arama optimizasyon algoritması aracılığıyla optimize edilen SpliCon'lara kıyasla aynı sürede daha yüksek performans sağladığını göstermektedir. Sinir ağı aracılığıyla optimize edilen SpliCon'ların performansı, çıkış düzlemindeki ışık şiddetinin deneysel sonucuyla doğrulanmaktadır. Sinir ağları eğitildikten sonra, 2 saniye içinde %96,6 ± %2,3 doğrulukla SpliCons tasarlamayı başarmaktayız; bu süre yerel arama optimizasyon algoritmalarından çok daha kısadır.

Daha sonra geniş bant ışığın spektral ayrıştırmasını gerçekleştiren bir KOE spektrometre tasarımı sunuyoruz. Tek bir prizma veya kırınım ızgarası ile oluşturulmuş bir optik spektrometre ile karşılaştırıldığında, KOE spektrometremiz ışığın her dalga boyu için tasarlanmış ve hareketli bir parça üzerine yerleştirilmiş birçok KOE'ından oluşmaktadır. Hareketli parça kullanılarak geniş bant ışıktan istenilen spektral ışığı elde etmek için her KOE'nın konumu değiştirilmektedir. KOE spektrometresindeki her KOE'ı, geniş bant ışığı belirli bir ışık dalga boyuna bölmektedir ve böylece KOE

spektrometremiz geleneksel spektrometrelere kıyasla geniş bant ışığı spektral ayrıştırmak için kullanılabilmektedir. Her dalga boyu için tasarlanmış KOE'ları kullanan spektrometremizin yüksek performans sağlayacağına inanıyoruz.

Ayrıca, bu tezde derin öğrenme modeli olan CHoLoNet aracılığıyla çoklu gözlem düzlemlerinde ve renklerde holografik görüntüler oluşturmak için optik hologramlar tasarlıyoruz. CHoLoNet, birden fazla görüntü düzleminde renkli holografik görüntü oluşturan hologramlar üretebilmektedir. Dahası, derin öğrenme modelimiz, ışığın faz ve genlik bilgisine gerek duymadan sadece ışığın şiddet görüntüsünden nesne/hologram bilgisini elde edebilmektedir. Sonuçlar derin öğrenme modeliyle elde edilmiş nesnelerin/hologramların referanslarla mükemmel uyumunu gösteriyor.

Anahtar Kelimeler: Dalga önü şekillendirme, holografi, görüntüleme, derin öğrenme, güneş enerjisi, spektroskopi, bilgisayarla oluşturulmuş hologram, kırınım optik elemanı, spektral ayrıştırma, sinir ağları, yapay zeka.

Beauty of science and nature

ACKNOWLEDGMENTS

Arnold Sommerfeld, Francesco Maria Grimaldi, Christian Huygens, Augustin-Jean Fresnel, Gustav Kirchhoff, John William Strutt, James Clerk Maxwell, Friedrich Kottler, Max Planck, and Isaac Newton made many outstanding contributions to Optics and Photonics. Without their ground-breaking efforts, solar energy, spectroscopy, imaging, and chiefly holography would not have shone vivid and discrete.

Assoc. Prof. Dr. Emre Yüce is my advisor who supports, informs, and enlightens me during my Ph.D. period. I have overcome many scientific issues with his help and our brainstorming sessions. Without his invaluable guidance, helpful suggestions, and endless support, fields of holography, imaging, optical spectroscopy, digital optics, and solar energy are not benefit from our novel ideas and ground-breaking results.

Through my thesis study, we have developed many novel ideas and discussions with Assoc. Prof. Dr. Alpan Bek and Assist. Prof. Dr. Ihor Pavlov, especially at the meetings for thesis monitoring presentations. Our peer-reviewed journal papers and the Turkish patents are improved and take much attention thanks to their contributions.

The members of the thesis examining committee: Prof. Dr. Alper Kiraz, Prof. Dr. Hakan Altan, Assist. Prof. Dr. Hasan Yılmaz, Assoc. Prof. Dr. Alpan Bek, and Assoc. Prof. Dr. Selçuk Yerci share their time for reading and commenting on this thesis. I am sincerely delighted for their efforts and suggestions.

Since my first step for a Ph.D. degree, I have met many great friends and colleagues. I am pleased with their friendship and acknowledge them for discussing science.

I would like to express my endless thanks to my parents for their love, patience, encouragement, support, and care.

I acknowledge reviewers who evaluated the results of our works presented in this thesis and published in the scientific peer-reviewed journals.

This study is financially supported by The Scientific and Technological Research Council of Turkey (TUBITAK), grant no 118F075, 118M199, 118E995, and with a grant program of 2211-A. Also, the Higher Education Council of Turkey (YOK) funds my Ph.D. study with the program of 100/2000. The Center for Solar Energy Research and Applications (ODTÜ-GÜNAM) at Middle East Technical University partially funds the research presented here. We also would like to thank the Turkish Academy of Sciences for the support provided via the TÜBA-GEBİP project.

TABLE OF CONTENTS

CHAPTERS

LIST OF TABLES

TABLES

LIST OF FIGURES

FIGURES

LIST OF ABBREVIATIONS

DOE	Diffractive optical element
SpliCon	Spectral splitter and Concentrator
CGH	Computer-generated hologram
CCD	Charge-coupled device
CMOS	Complementary metal-oxide-semiconductor
SOE	Spectral optical efficiency

CHAPTER 1

INTRODUCTION

The light that stays at a central point of our life exists in every aspect of nature. The control of light is becoming more of a necessity to support the advancements in science and technology. We have a variety of light sources as the Sun, lasers, light bulbs, etc. that are utilized to develop novel technologies. Each source presents its own properties in terms of amplitude, phase, polarization, intensity, wavelength, coherency, repetition rate, and wavefront. Sometimes the current specifications of a light source are not suitable for an application of interest. Besides, the light demonstrates essential phenomena: scattering, transmission, absorption, refraction, reflection, and diffraction. Combined control of the light source specifications and the aforementioned physical phenomena will pave the way for novel and disruptive technologies.

1.1 Control of light

Spectral and spatial control of light has a strong influence in central fields such as imaging [1, 2] (see Fig. 1.1), sensing [3], communications [4], holography [5, 6], light focusing [7], spectral control [8], microscopy [9], aberration correction [10], wavelength-multiplexing [11], and solar energy [12, 13, 14, 15, 16] which directly affect the advancement of humanity. Traditional optical elements for controlling light such as lenses, mirrors, lamellar gratings, etc. are too bulky for compact applications and expensive for large scale applications. However, modern approach of using spatially controlled pixels close to the wavelength of light drastically increases our ability to gain control on light.

Enhanced control of propagation, diffraction, scattering, and interference of light us-

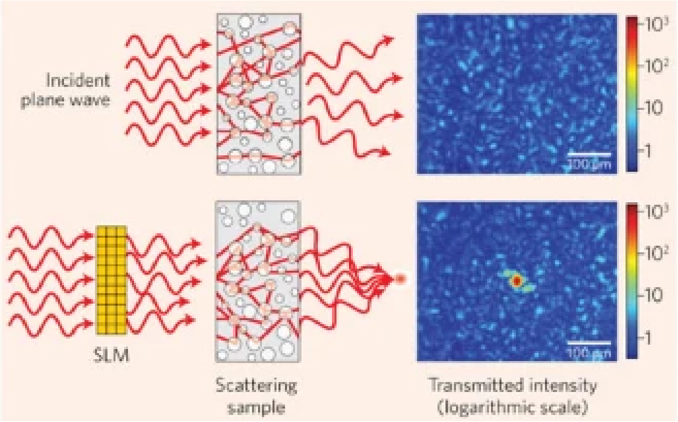

Figure 1.1: A scheme shows focusing light through a scattering sample using a spatial light modulator (SLM) on a camera. The image is adapted from Ref. [1].

ing micro-and nano-structures plays an important role in tailoring light for specific applications [17, 18]. Phase plates can modulate direction, amplitude, phase, and polarization of the light or a combination of these properties, which makes them superior to conventional optical structures [19, 20, 21]. The multi-dimensional control provided by the phase plates yields to versatile performance increases in imaging [22], holography [5, 6], light focusing [7], spectral control [8], microscopy [9], aberration correction [10], wavelength-multiplexing [11], and solar energy [23]. Although the control on phase provides numerous advantages, the phase being sensitive at dimensions close to the wavelength of incident light brings extra challenges to overcome. The increased resolution requirement in designing phase plates also increases the number of parameters to be optimized for efficient control of light. Below I share phase control elements that show great performance in the control of light.

1.1.1 Spatial light modulator

Spatial Light Modulator (SLM) is a liquid crystal-based device that produces high-resolution and high-speed phase and amplitude modulation with individually addressable pixels (see Fig. 1.2a). The SLMs present precise and dynamic shaping of light beams via a computer interface. The SLMs offer a finite number of independently controllable pixels, which dictate how efficiently the SLMs utilize the power of light. Because liquid crystals in the SLMs perform light modulation in a particular wave-

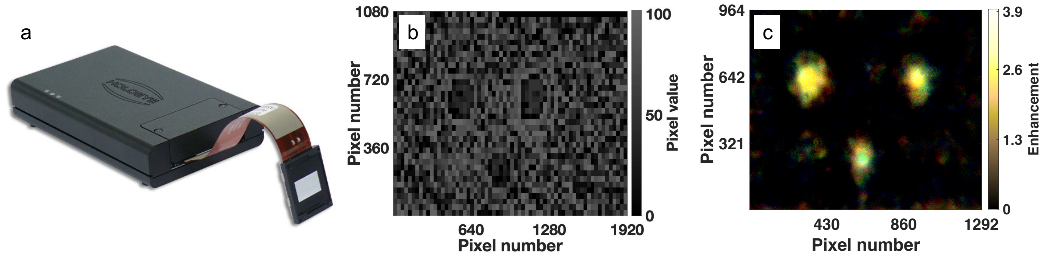

Figure 1.2: (a) A photograph of an SLM. The image is adapted from Ref. [28]. (b) An example hologram displayed on an SLM for modulation of light and (c) corresponding holographic image on a color CCD camera.

length spectrum of light, specifications of SLMs as pixel size, operating wavelength, and anti-reflective coating material for reflective SLMs are variant. The SLMs are currently used in various applications such as optical filtering [24], holographic image projection [25], spatial Fourier filtering of images [26], and projecting structured light fields [27].

Light modulation with the SLMs is accomplished by applying an electric field across a liquid crystal (LC) layer within the SLMs. Light propagating through the anisotropic LC material experiences a phase difference due to difference in refraction index that is a function of the applied voltage. Driving the LC material between two polarizers can lead to the intensity and/or phase modulation for the incident light beam. Thank to the computer interface the SLMs enable, the phase and amplitude of the light are modulated with a gray-scale image as an example in Fig. 1.2b and its corresponding color CCD image in Fig. 1.2c. This gray-scale image is called a computer-generated hologram (CGH). By designing this CGH, modulation of light for applications of interest will be possible.

1.1.2 Digital micromirror device

A deformable mirror device which is also called a digital micromirror device (DMD), is a spatial light modulator based on a micro-electro-mechanical system (MEMS) technology product (see Fig. 1.3). The DMDs control an array of movable microscopic mirrors for phase retardation and redirecting incident light. Individual mirror

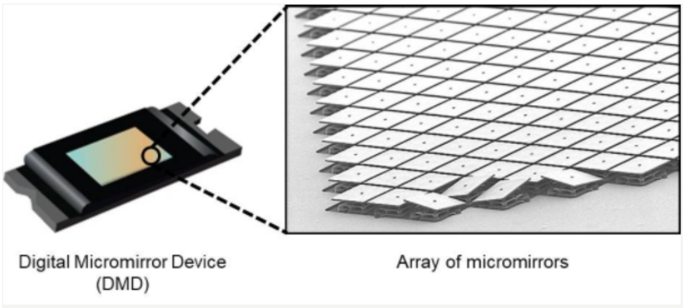

Figure 1.3: A scheme of a DMD. Inset shows close look on the DMD mirrors. The image is adapted from Ref. [35].

deflection is induced electrically [29]. The DMDs operate as purely binary amplitude modulators but perform phase modulation by igniting super-pixel method [30]. The amplitude and phase modulation of light by using the DMDs can be performed by a hologram with 2-bit pixel-wise information. The DMDs modulate light under a specific wavelength range due to their reflective coating. Due to the capability and functionality that the DMDs offer in scientific and technological areas, the DMDs are utilized for such as beam shaping [31], structured illumination microscopy [32], lithography [33], and optical coherence tomography [34].

1.1.3 Diffractive optical element

Diffractive optical elements (DOEs) [36, 37, 38, 39, 40] are thin, compact, and multipurpose optical devices that manipulate and modulate light in a variety of ways (see an example DOE and corresponding intensity distribution at the target plane in Fig. 1.4). The DOEs utilize diffraction and interference of light with preferably minimal light scattering. Their importance is shown with the use of DOEs in plenty of application areas of science for improving beam quality of a laser [41], controlling modes of a light source [42], suppressing speckle in a compact laser projection [43], increasing numerical aperture in a confocal microscopy [44], and enhancing the performance of solar cells [45, 46, 13, 47]. The broad accommodation reasons of the DOEs can be attributed to their simplicity in modeling, thin-geometry, relatively efficient structures, and low-cost manufacturability. The DOEs initiate diffraction of light as a result of the wavelength-comparable size of the structures. It is the heart of the DOEs to control the phases and directions of multiple light beams. In the meantime, they shape the wavefront of light to the desired form. Compared to refractive structures, the DOEs eliminate chromatic aberration via design and optimization of the geometric variables of the structures [48]. The DOEs can be designed by computational tools [36], experimentally with the SLMs [25] and the DMDs [30]. This light modulation which is performed by the DOEs, the SLMs, and the DMDs, follows the same light phenomena. A variety of the DOE profiles exist as fork grating [49], diffractive axicon [50], supplying an extended depth of focus compared to Gaussian beams, and blazed diffractive optic [51]. Their performance increases with the number of controlled parameters that form the structural properties. Thanks to recent developments in science and technology, fabrication of the DOEs becomes more accessible using photolithography [52], E-beam lithography [53], and direct laser writing [54].

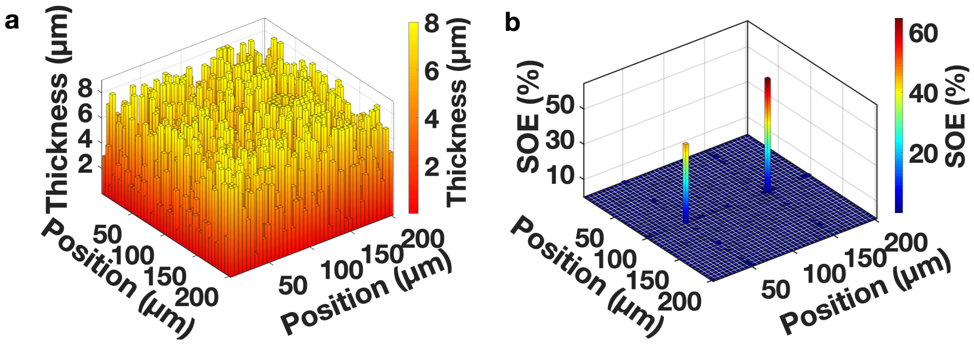

Figure 1.4: (a) A scheme of a diffractive optical element and (b) corresponding intensity distribution at the target plane in terms of spectral optical efficiency (SOE), which is the percentage intensity at the target area, see Eq. 3.5. The figure is taken directly from Ref. [8].

1.1.4 Spectral splitter and concentrator

A DOE can spectrally disperse the broadband light and steer individual spectral bands to the relevant target solar cells. We classify these multi-functional diffractive optical elements as spectral splitters and concentrators (SpliCons) [23] to distinguish from the DOEs that can only achieve spectral splitting. Unlike conventional DOEs generally designed for one task, the SpliCons provide simultaneous spectral splitting and concentration of light. These multi-functional structures can be optimized with iterative approaches. Still, iterative optimization requires immense computational resources and limits the application of the SpliCons due to small numbers of controlled parameters that can yield reduced performance. Instead of iterative approaches, the inverse design of the SpliCons can decrease the optimization time. However, the inverse-design presents several significant challenges compared to the iterative: i) phase plates in each frequency of broadband range are needed, ii) combination of these phase plates will still require intermediate phase plates to obtain desired intensity distribution, iii) one-to-many mapping problem [55]. One-to-many mapping is a big problem because a data point may be associated with multiple labels instead of a single class [56, 57]. Thus, spectrally splitting and concentrating the light using the inverse design is still an unaddressed challenge. The neural network architecture of deep learning could figure out one-to-many mapping problem faced in the inverse-design of the SpliCons and provide fast and accurate control over light beams.

1.2 Solar energy

Solar energy is a clean and promising energy source endorsed by the recent developments in this field that provide improved efficiencies at lower costs. The radiation on the Earth received from the Sun is about 162000 TW, and this means that harvesting even a tiny fraction in excess with available technologies helps to decrease our energy need [13]. Solar energy is converted into electricity via photovoltaic cells. Commercial solar cells are monocrystalline and multicrystalline silicon cells whose efficiencies range between 20% [58] to 24.4% [59]. Important reasons for the low conversion efficiencies are the broadband nature of the sunlight, and the photovoltaic cells have a fixed and material-dependent spectral absorption profile [13]. Therefore, light energy whose frequency is lower than the cut-off frequency of the material is not converted into valuable energy. Similarly, photons with higher energy than the bandgap energy of the solar cell cause the generation of excess heat via thermalization through phononic channels [60, 61]. Thermalization leads to degradation of the solar cells performance and shortening the lifetime of the solar cells. Thus, the conversion efficiencies of the solar cells decrease. These two reasons alone cause about 55% decrease in conversion efficiencies of conventional solar cells. Therefore, these reasons reduce the maximum theoretical efficiencies of the solar cells to about 33%. Moreover, they lead to a decrease in the external quantum efficiencies [13]. Using spectral splitting elements, photons that do not generate electricity are guided to a thermal receiver for a hybrid photovoltaic-thermal system that results in significant improvement in heat management [62, 63].

The solutions to increase the conversion efficiencies of the solar cells are concentrating the incoming radiation [64], accommodation of tandem configuration, and splitting the solar spectrum and directing each spectral band to the most efficient converters [13]. Concentrating the incoming radiation with a concentrating system increases the efficiencies of the conventional solar cells by 10%, and overall efficiencies become range between 20% and 25% [64]. Besides, concentrating the sunlight decreases the amount of solar absorbing materials but increases the size and weight of the solar cell systems. Secondly, multi-junction solar cells increase conversion efficiencies. They are a combination of semiconductor materials of different bandgaps to absorb different wavelengths of the sunlight to overcome Shockley's theoretical limitation, and it is believed that theoretical efficiencies up to 86% can be obtained with the multijunction solar cells and concentrated light [65]. Tandem configuration, which gives higher photovoltaic efficiencies, bears a stack of photovoltaic subcells with different bandgaps in a vertical direction. However, the tandem configuration is costly to fabricate due to the complicated epitaxial growth procedure of multiple layers imposing constraints on performance and design [66]. When the inherent broadband radiation from the sun is directed to two or more narrow spectral-sensitive solar energy converters arranged as lateral single-junction architecture via spectral splitting techniques, it leads to a massive increase in functionality and the efficiencies of solar cells. Laterally arranged solar cells that are made from two different materials produce increased energy output by enhancing spectral overlap between the absorption spectra of solar cells and the incident spectrum of the sunlight [67, 46, 68, 69, 13].

1.3 Spectroscopy

Optical spectroscopy is a scientific branch that inspects the interaction of electromagnetic radiation with matters [70]. Spectroscopy covers extensive scientific and technological areas thanks to the development of lasers and optical elements, which supply extraordinary sensitivity and speed for spectrometers. Optical spectroscopy plays essential roles in numerous applications such as medical diagnostics [71], chemical analysis [72, 73, 74, 75], and identification of biological materials [76, 77]. Experimental spectroscopy methods began with the more accessible visible region of the electromagnetic spectrum where the human eye could be used as a photodetector. After Newton performed his famous experiments on the dispersion of white light into a range of colors using a triangular glass prism in 1665, the spectral inspection of matter began to become possible. Later, Bunsen and Kirchhoff developed the prism spectrometer around 1860. Early applications of this spectrometer were to observe the emission spectra of various samples in a flame.

Optical spectrometers are essentially constructed with a light source, a light detector (human eyes, photodetectors, etc.), and a spectral splitting element (prisms, diffraction gratings) to analyze wavelength components of light that are absorbed by, transmitted through, reflected, or scattered from a sample. The performance of the spectrometers is highly affected by the noise of the light source, the spectral resolution of the spectral splitting element, and the detector's sensitivity. The optical spectrometers generally give an intensity-dependent transmission spectrum of light. The interaction of light is presented in terms of wavelength, frequency, and wavenumber. Dependent on the spectral region of light and the design of spectrometers, different spectral splitting elements are operated. They are prisms and diffraction gratings. The prisms refract incoming light into wavelength components by using the dispersion characteristic of the prisms. The diffraction gratings employ the diffraction nature of light which occurs when the size of gratings is comparable to the wavelengths of light. The diffraction gratings consist of parallel grooves ruled on a hard glassy or metallic material. The grooves are extremely closely spaced, and diffraction gratings are usually coated on a reflecting material such as aluminum so that the diffraction gratings also work as a mirror. As mentioned above, these spectral splitting elements operate under narrow-band light. They can be designed considering the overall wavelength components of these narrow-band light, not each wavelength component of the light band. Therefore, the conventional spectrometers suffer from the low performance of spectral splitting elements.

1.4 Holography

In nature, objects that we see present 3-dimensional spatial information, and unfortunately, we record the objects or views in 2-dimension due to the limitations of recording devices. Any recording device such as CCD cameras, CMOS cameras, photographic plates, photochemical, photoelectronic, and biological recording devices stores 3D objects or scenes information in 2D intensity distributions. These devices form intensity information by using a time-averaged intensity of the light field. As a result, we lose the information of phase, polarization, and wavefront of light. Also, all information about the optical paths from different parts of the scenes to the recording devices is lost. Since all recording materials bear only the image in terms of the intensity, it is necessary to convert the phase information into variations of intensity to record the phase and the amplitude of light simultaneously. Holography enables the reconstruction of all information of objects or scenes, which are not possible solely by the recording devices.

Holography that conveys important roles in wide scientific fields dates back to the invention of the first hologram with in-line configuration by Dennis Gabor [78, 79]. Optical holography is a superior tool to retrieve the phase and amplitude of light from an intensity image which bears detailed information of the object as size, shape, and refractive index. Reconstructed object/hologram from the intensity image enables high-security encryption [80], detailed microscopy information [81], data storage [82], 3D object recognition [83], and design of planar solar concentrator [8, 23, 84].

Optical holography also leads to the formation of intensity images at different observation planes or through a sample without requiring any focusing elements or mechanical scanning. Thus, holography is also named a lensless imaging technique. It finds numerous applications such as imaging [18, 85], photo-stimulation [86], printing [87], optical beam steering [27], aberration correction [88], display [89, 90], and augmented reality [91].

There are three different aspects to holograms. When holograms are recorded on photographic films, they are called analog holograms. Instead of photographic films, the holographic images are displayed and recorded on the cameras. This kind of holographic recording is called digital holography. As mentioned previously, the SLMs and DMDs can modulate incident light and generate holographic structures. When the holograms are designed by the SLM, the DMDs, or mathematical tools, the holograms are called computer-generated holograms (CGH), having the same properties as analog and digital holograms.

An image recorded with any recording device is called a hologram with a 2D intensity distribution. Recording the hologram is done using coherent illumination and requires a reference beam derived from the same source. The recording devices mentioned above store the interference pattern produced by this reference beam and the light waves scattered by the object. Since the intensity at any point in this interference pattern also depends on the phase of the object wave, the resulting hologram contains information of the phase and the amplitude of the object wave. If the hologram is illuminated once again with the original reference wave, it reconstructs the original object wave. After the hologram is illuminated with the original collimated beam, it produces two diffracted waves: one for reconstructing an image of the object in its original location and the other for reconstructing a second image with the same amplitude but the opposite phase named a conjugate image. These two images are twin, and the holography suffers from the separation of the twin images. A significant drawback of the holography is the poor quality of the reconstructed image because it is degraded by the conjugate image, which is superimposed on the reconstructed image.

An exciting property of holography is that every part of a hologram contains information about the entire object. Therefore, every part of the hologram has similar information of the object despite the reduction of effective pixel number leading to a reduction of resolution in the reconstructed images [92]. With wide-field holography, the mutual information between pixels may allow simplified phase-contrast mapping in such as confocal optical microscopy [93]. The process of beam interfering demands high levels of light intensity, extreme stability of optical setup, and a relatively narrow bandwidth light source. These limitations have prevented holograms from becoming widely used for many practical applications [94].

1.5 Deep learning

Deep learning is a scientific branch of artificial intelligence that can pull helpful information from a data set with the help of decision-making in an algorithm [95]. The primary aim of deep learning is to allow a machine to discover valuable knowledge just like humans do. Deep learning refers to the architectures which possess multiple hidden layers. Deep learning extracts different characteristics with numerous levels of abstraction after seeking to exploit unknown patterns in input data to discover good representations with higher-level learned features. Although deep learning has been around since the 1980s, it was relatively unpopular for several years because the computational infrastructure, hardware, and software were insufficient. Also, the available data sets were not enough to form a deep learning model. Deep networks made a significant reappearance, proving their high potential after the evolution in hardware and software.

Compared to conventional machine learning techniques, deep learning architectures process the input data to seek the relations between the input data and output data. Deep learning involves learning these relations automatically during a training process instead of designing a set of rules and algorithms to extract attributes from the input data. A deep learning model contains lower layers that decode some essential representation of the relations and higher-level layers build upon these lower layers to understand more complex concepts. Once deep learning networks have more layers and parameters, the networks have the potential to represent more complex inputs.

Deep learning can perform time-consuming operations using multilayered neural networks within shorter time scales. This technique has exhibited outstanding success in various optics and photonics fields such as microscopy [96, 97, 98], imaging [99, 100, 101, 102], wavelength demultiplexing [103], metasurface design [104, 105], reconstruction of ultra-short pulses [106], image classification [107], beam splitting [108], and laser-assisted surface machining [109, 110]. Moreover, deep learning understands Fourier transform function by using neural neurons having a single layer with a linear transfer function [111].

1.6 Outline of this thesis

In this thesis, we present spectral and spatial control of light for applications of solar energy, spectroscopy, holography, and imaging. Firstly the effective bandwidth approach is introduced for decreasing the design duration of the DOEs for the application of solar energy. Then, the detail of a deep learning model, the DOENet, is presented to tune structural parameters of the SpliCons/DOEs. Later, we carried out immersive research for angle-insensitive solar energy harvesting. Next, we experimentally split and spatially concentrate the incoherent broadband light using wavefront shaping. Then, an invention for optical spectroscopy, the DOE spectrometer, is presented for the broadband operation of the optical spectrometers. Lastly, we generate optical holographic images at multiple wavelengths and observation planes without cross-talk in images. We also deliver a deep learning-based fast and high accurate object/hologram retrieval approach.

CHAPTER 2

THEORY

Light is a transverse electromagnetic wave and has many properties such as polarization, wavelength, amplitude, intensity, and wavefront, which describe the behavior of light. The concept of the wavefront is oriented to describe such a three-dimensional spreading of the light waves. The wavefront of the light has an identical phase surface linking the peak of each wave. The wavefront varies while the light propagates and interacts with a substance. When a light-blocking object is present in the traveling direction of the light wave, the light displays the diffraction phenomenon. The principle of diffraction is due to quantum mechanics; spatial obstacle in one direction leads to dispersion in momentum or k-vector. Thus, light shows diffraction. Huygens's principle describes what occurs after the diffraction as the secondary waves are emitted from the place where the light-blocking object is present if a point light source exists on a wavefront at a particular moment. After a specific time elapses, the secondary waves overlap and combine to create a new wavefront. The electric field of the light is expressed by Eq. 2.1 using electric field amplitude $A(r)$ and phase $\phi(r)$ when the light travels, and its electric field oscillates in three dimensions.

$$E(r) = A(r)\exp[-j\phi(r)] \tag{2.1}$$

2.1 An important phenomenon: Diffraction of light

The light demonstrates various scientific phenomena like reflection, absorption, scattering, refraction, and diffraction. The diffraction is of the utmost critical phenomenon to be understood for spectrally and spatially controlling light behavior. The term "diffraction" was first described by Arnold Sommerfeld [112]. The effect of light diffraction considers any deviation of light rays from rectilinear paths. The diffraction arises when the lateral dimensions of the light are confined by a structure whose size is comparable to the size of the radiation. The chronological background of the diffraction was started by Francesco Maria Grimaldi, who constructed the first accurate description. Grimaldi experimented with a light source to illuminate an opaque screen where an aperture exists. He observed that the light intensity transition across the screen is gradual rather than abrupt. The initial step in developing the diffraction theory that defined such a phenomenon was constructed by Christian Huygens in 1678. Huygen described that each point on the input wavefront of a disturbance is assumed a new source of a secondary spherical disturbance after lateral confinement of the light. Augustin-Jean Fresnel computed the distribution of light in diffraction patterns with high accuracy. Gustav Kirchhoff made a firmer mathematical foundation for the diffraction of light by using the ideas of Huygens and Fresnel in 1882. Kirchhoff showed the diffraction of the light is a consequence of the wave nature of the light. The mathematical formulation of Kirchhoff has two assumptions about the boundary values of the light (the assumptions are noted below). Later, these assumptions were confirmed to be inconsistent with each other, although these assumptions allow producing results under most conditions that agree amazingly well with experiment results. Later, Arnold Sommerfeld revised the boundary conditions and developed the Rayleigh-Sommerfeld theory. The Kirchhoff and Rayleigh-Sommerfeld theories facilitate the treatment of light diffraction with the scalar theory of light and ignore the fundamentally vectorial nature of the electromagnetic fields. The Kirchhoff and Rayleigh-Sommerfeld theories also disregard the components of the electric and magnetic fields at boundaries that are coupled through Maxwell's equations and cannot be treated independently. Instead of scalar treatment of the light after a diffracting surface, the vectorial treatment of diffraction may be completed to cover all aspects of the diffraction fully, and Friedrich Kottler firstly conducted the vectorial treatment of diffraction theory.

When a beam of light interacts with a structure whose size is wavelength comparable or passes through a periodic structure, the beam is diffracted into multiple orders. In the grating equation (see Eq. 2.2), the relations among the period of the structure d, the order number n, the wavelength of the beam λ, the incident angle of the beam θ_i, and the diffraction angle of the beam θ_n at the order n are given. The repeated structure and the beam's wavelength determine the angular separation between the orders. A small period constructs significant angular separation, while an extended period results in closely spaced output beams.

$$d(\sin\theta_n - \sin\theta_i) = n\lambda \tag{2.2}$$

2.2 Fourier transformation

A Fourier transform (FT) is a mathematical transform that disintegrates functions expressed in terms of space or time into functions relying on spatial or temporal frequency, respectively [112]. Fourier transform refers to the frequency domain representations, and the mathematical operation associates the frequency domain representations to a function of space or time. The Fourier transform of a function of time is a complex-valued function of frequency, whose magnitude represents the amount of that frequency in the original function and whose argument is the phase offset of the basic sinusoidal in that frequency. The Fourier transform is not limited to time-based functions, but the domain of the original function is generally referred to the time domain. An inverse Fourier transform mathematically synthesizes the original function from its frequency domain representation, as proven by the Fourier inversion theorem. The Fourier transform process may be considered as decomposing a complicated function into a collection of more simple complex exponential functions. In Eq. 2.3, how to compute Fourier transform of a function $U(x, y, 0)$ is revealed where $A\left(f_X, f_Y; 0\right)$ is Fourier transform of the function $U(x, y, 0)$. In the equation (x, y) is coordinate in real space, and (f_X, f_Y) is coordinate in spatial frequency.

$$A\left(f_X, f_Y; 0\right) = \iint_{-\infty}^{\infty} U(x, y, 0) \exp\left[-j2\pi\left(f_X x + f_Y y\right)\right] \mathrm{dxdy} \tag{2.3}$$

Suppose the complex field distribution of a monochromatic disturbance is Fourier-analyzed across any plane. In that case, the various spatial Fourier components can be determined as plane waves traveling in different directions away from that plane.

The field amplitude at any other point (or across any other parallel plane) can be computed by adding the contributions of these plane waves in terms of the phase shifts the plane waves experience during propagation.

2.3 Scalar theory

The scalar theory offers a simple way to treat the behavior of light propagation [112]. It is deployed to study light propagation through a dielectric medium demonstrating linear, isotropic, homogeneous, and nondispersive properties. When a medium fulfills such conditions, all components of the electric and magnetic field of light act identically. Also, their behavior is fully defined by a single scalar wave equation (see Eq. 2.4). In Eq. 2.4, $u(r, t)$ denotes any of the scalar field components which relies on position r and time t. The Laplacian operator, the refractive index of the dielectric medium, and the vacuum velocity of the light are described with symbols ∇, n, and c, respectively.

$$\nabla^2 u(r,t) - \frac{n^2}{c^2}\frac{\partial^2 u(r,t)}{\partial t^2} = 0 \tag{2.4}$$

The scalar field of a monochromatic wave is expressed with Eq. 2.5 where $U(r)$ and ν are complex function of the electric field on position r and the optical frequency, respectively. The complex function of the electric field $U(r)$ is based on phase shift $\phi(r)$ and field amplitude $A(r)$ (see Eq. 2.6). After inserting Eq. 2.5 into the scalar wave equation (see Eq. 2.4), we encounter the Helmholtz equation in Eq. 2.7 where k is wavenumber and equals to $k = 2\pi/\lambda$.

$$u(r,t) = \mathrm{Re}\{U(r)\exp(-j2\pi\nu t)\} \tag{2.5}$$

$$U(r) = A(r)\exp[-j\phi(r)] \tag{2.6}$$

$$\left(\nabla^2 + k^2\right) U = 0 \tag{2.7}$$

A diffraction pattern induced after the light meets an aperture is treated employing the scalar theory of light with some assumptions instead of the fundamentally vectorial nature of the electromagnetic fields. These assumptions are that the diffracting aperture must be large compared with the wavelength of the light, and the diffracting field must not be observed too close to the aperture. When these two criteria are satisfied, the scalar theory delivers accurate results. However, when the diffraction pattern is calculated for high-resolution gratings and tiny pits on optical recording media, important issues exist due to not fulfilling the demanded conditions noted above. In this case, the vectorial nature of the fields must be taken into account. When the vectorial nature of the fields is paid attention to, the E and H fields are adjusted only at the edges of the aperture where the light interacts with the material of which the edges are formed.

2.4 Green's theorem

Light exhibits a complex disturbance after encountering a diffracting structure. The formed complex disturbance can be computed with the aid of Green's theorem [112]. Let $U(r)$ and $G(r)$ be any two complex-valued functions relying on position r, and let S be a closed surface enclosing a volume V. If U, G, and their first and second partial derivatives are single-valued and continuous within and on the closed surface of S, then we reach Eq. 2.8 to express a link between $U(r)$ and $G(r)$. A partial derivative in the normal outward direction at each point on S is expressed with $\frac{\partial}{\partial n}$ in Eq. 2.8. Under different assumptions about Green's function of the problem, diverse solutions to the scalar diffraction problem are acquired.

$$\iiint_V \left(U\nabla^2 G - G\nabla^2 U\right) dv = \iint_S \left(U\frac{\partial G}{\partial n} - G\frac{\partial U}{\partial n}\right) ds \tag{2.8}$$

2.5 The Fresnel-Kirchhoff Diffraction Formula

To find a diffraction field at the point P_0 behind an aperture as seen in Fig. 2.1, we use the integral theorems of Helmholtz, Kirchhoff, and Green [112]. It is now feasible to describe the disturbance at P_0 in terms of the disturbance and its normal derivative over the aperture size S with Eq. 2.9. The screen is opaque, except the aperture has a surface area S. Gustav Kirchhoff invented a formulation for the diffraction problem that possesses a particular integral theorem that conveys the solution of homogeneous wave equation at an arbitrary point in terms of the values of the solution and its first derivative on a random closed surface enclosing that point. Kirchhoff employed the following assumptions for the formulation of the diffraction pattern:

- Across the surface S, the field distribution U and its derivative $\frac{\partial U}{\partial n}$ are the same as they would be in the absence of the screen,
- Over portion of the S that lies in the geometrical shadow of the screen, the field distribution U and its derivative $\frac{\partial U}{\partial n}$ are identically zero.

These conditions are commonly known as Kirchhoff's boundary conditions. The first condition allows us to represent the disturbance incident on the aperture by disregarding the existence of the screen. The second condition allows us to ignore all surface integration, excluding the portion lying directly within the aperture itself.

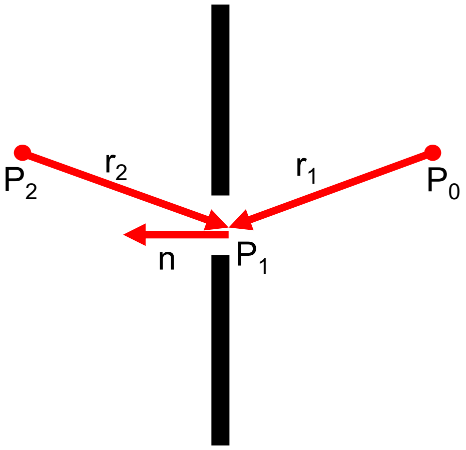

Figure 2.1: A sketch demonstrates a point source illumination to an opaque plane screen with an aperture with a surface area S.

$$U\left(P_0\right) = \frac{1}{4\pi} \iint_S \left(\frac{\partial U}{\partial n} G - U \frac{\partial G}{\partial n} \right) ds \tag{2.9}$$

For the computation of the diffraction pattern, we resume with the expression in Eq. 2.9. We denote the point of observation P_1 as seen in Fig. 2.1 and an auxiliary function G in Eq. 2.9 that is a unit-amplitude spherical wave expanding about the point P_0. This auxiliary function G is named free-space Green's function, and the value of Kirchhoff's G at the point P_1 is given with Eq. 2.10. This diffraction expression is formulated for the cases where a monochromatic light source illuminates the aperture, and the distance r_1 from the aperture to the observation point is assumed as many optical wavelengths; therefore, the wavenumber $k >> 1/r_1$. Also, we assume that the aperture is illuminated by a single spherical wave originating from a point source at P_2, a distance r_2 from the aperture, which is formulated as seen in Eq. 2.11. Similarly, r_2 is many optical wavelengths.

$$G\left(P_1\right) = \frac{\exp\left(jkr_1\right)}{r_1} \tag{2.10}$$

The partial derivative of Eq. 2.11 is given in Eq. 2.12, and it is approximated due to the fact that r_2 is many optical wavelength as stated above. The partial derivative of Eq. 2.10 produces Eq. 2.13, and it is approximated owing to the fact that r_1 is many optical wavelength. After inserting Eq. 2.10, Eq. 2.11, Eq. 2.12, and Eq. 2.13 into Eq. 2.9, we obtain Fresnel-Kirchhoff diffraction formula (see Eq. 2.14). The fully expression of $U'\left(P_1\right)$ is located in Eq. 2.15.

$$U\left(P_1\right) = \frac{A\exp\left(jkr_2\right)}{r_2} \tag{2.11}$$

$$\begin{aligned} \frac{\partial U\left(P_1\right)}{\partial n} &= \cos\left(\vec{n},\vec{r_2}\right)\left(jk - \frac{1}{r_2}\right)\frac{A\exp\left(jkr_2\right)}{r_2} \\ &\approx jk\cos\left(\vec{n},\vec{r_2}\right)\frac{A\exp\left(jkr_2\right)}{r_2} \end{aligned} \tag{2.12}$$

$$\begin{aligned} \frac{\partial G\left(P_1\right)}{\partial n} &= \cos\left(\vec{n},\vec{r_1}\right)\left(jk - \frac{1}{r_1}\right)\frac{\exp\left(jkr_1\right)}{r_1} \\ &\approx jk\cos\left(\vec{n},\vec{r_1}\right)\frac{\exp\left(jkr_1\right)}{r_1} \end{aligned} \tag{2.13}$$

$$U\left(P_0\right) = \iint_S U'\left(P_1\right)\frac{\exp\left(jkr_1\right)}{r_1}ds \tag{2.14}$$

$$U'\left(P_1\right)=\frac{1}{j\lambda}\left[\frac{A\exp\left(jkr_2\right)}{r_2}\right]\left[\frac{\cos\left(\vec{n},\vec{r}_1\right)-\cos\left(\vec{n},\vec{r}_2\right)}{2}\right] \tag{2.15}$$

Eq. 2.14 is symmetrical with respect to the illumination point source at P_2 and the observation point at P_0. Thus a point source at P_0 will yield the same effect at P_2 that a point source of equal intensity placed at P_2 will produce at P_0. This result is expressed with the reciprocity theorem of Helmholtz. Eq. 2.14 may be interpreted as the field at P_0 arises from an infinity of fictitious "secondary" point sources located within the aperture itself. The secondary sources have certain amplitudes and phases defined by $U'\left(P_1\right)$ that is connected to the angles of illumination and observation and the illuminating wavefront.

The Kirchhoff theory, which delivers experimentally accurate results, is widely used in practice. However, there are particular internal inconsistencies in theory since the boundary conditions are used on both the field strength and its normal derivative. As we know that a well-known theorem of the potential theory dictates that if a two-dimensional potential function and its normal derivative vanish together along any finite curve segment, that potential function must vanish over the entire plane. Yet, the two Kirchhoff boundary conditions imply that the field is zero everywhere behind the aperture, so the result contradicts the theorem of the potential theory.

A further indication of the inconsistencies in the boundary conditions is met when the Fresnel-Kirchhoff diffraction formula fails to reproduce the assumed boundary conditions as the observation point approaches the screen or aperture. Later, Sommerfeld eliminated the inconsistencies in the Kirchhoff theory by terminating the necessity of setting boundary values on both the disturbance and its normal derivative simultaneously, and Rayleigh-Sommerfeld's theory was developed. Also, we encounter another failure in the boundary conditions due to the presence of the screen that inevitably perturbs the fields on the surface S to some degree owing to the rim of the aperture. To eliminate these concerns, fully vectorial treatment of the diffraction is required.

2.6 Fundamentals of holography

Phase and amplitude of light after light scattered by an object are stored in terms of intensity with a recording medium called a hologram. While recording the phase and amplitude of the light with a hologram, interference of an object wave U_{Object} (Eq. 2.16) and a reference wave $U_{Reference}$ (Eq. 2.17) is required [112]. $\psi[x, y]$, $\varphi[x, y]$, $A(x, y)$, and $a(x, y)$ are phase distribution of the object wave, phase distribution of the reference wave, amplitude of the object wave, and amplitude of the reference wave at the coordinates (x, y), respectively. The recording medium stores the intensity distribution of the interference field I obtained with Eq. 2.18 while recording the hologram. This equation is derived for the case that both the object and the reference beams are parallel to each other to form an in-line hologram. As seen here, the intensity of interference depends on the amplitudes and phases of the object and the reference waves. The first two terms in Eq. 2.18 bear the intensities of the object and reference beams. The third term indicates the relative phase difference between the object and the reference beams, which is highly important for recording the object information, which scatters the object beam.

$$U_{Object}(x, y) = A(x, y)exp(-j\psi[x, y]) \tag{2.16}$$

$$U_{Reference}(x, y) = a(x, y)exp(-j\varphi[x, y]) \tag{2.17}$$

$$I(x, y) = |A(x, y)|^2 + |a(x, y)|^2 + 2\,|A(x, y)|\,|a(x, y)|\,cos[\varphi(x, y) - \psi(x, y)] \tag{2.18}$$

After illumination of the holographic structure with the interfered light, we encounter a recorded intensity $t_A(x, y)$ as seen in Eq. 2.19. β' is a factor that stands for a relation between the interference intensity and exposure of the hologram, and t_b is a uniform bias transmittance established due to the factor β' and $|a(x, y)|^2$. To reconstruct the amplitude and phase information of the object wave recorded, we illuminate the same recorded hologram $t_A(x, y)$ by a coherent reconstruction wave $B(x, y)$.

The light transmitted by the hologram is equal to $t_A(x,y)B(x,y)$ (see Eq. 2.20). If $B(x,y)$ is simply an exact duplication of the original uniform reference wavefront $U_{Reference}(x,y)$, the forth term of Eq. 2.20 can be expressed as that in Eq. 2.21.

$$t_A(x,y) = t_b + \beta' \left(|A|^2 + A^*a + Aa^*\right) \tag{2.19}$$

$$\begin{aligned} t_A(x,y)B(x,y) &= t_bB + \beta' AA^*B + \beta' A^*aB + \beta' Aa^*B \\ &= U_1 + U_2 + U_3 + U_4 \end{aligned} \tag{2.20}$$

$$U_4(x,y) = \beta' A(x,y)|a|^2 \tag{2.21}$$

Once the intensity of the reference wave is uniform, the reconstructed wave component U_4 is an exact duplication of the original object wavefront $U_{Object}(x,y)$. Similarly, if $B(x,y)$ is chosen as the conjugate of the original reference wave $U^*_{Reference}(x,y)$, the third term of the reconstructed field $U_3(x,y)$ becomes like that in Eq. 2.22.

$$U_3(x,y) = \beta' A^*(x,y)|a|^2 \tag{2.22}$$

As seen in Eq. 2.22, $U_3(x,y)$ is linearly proportional to the conjugate of the object wavefront. Term U_3 is responsible for the construction of a virtual image, and the term U_4 recovers a real image. Both images are centered on the hologram axis. These so-called twin images are separated by an axial distance $2z$, where z is the distance between the recording medium and the object. Yet, for highly translucent objects, the quality of the real image is lowered by the conjugate image, which forms on the same hologram axis. This situation refers to the twin image issue. As said above, reconstruction of the hologram is prevented by the twin image problem. The twin image can be eliminated by the transport of intensity method [113], the three-exposure method [114], and angularly separation of the reconstruction [115]. In addition to the twin image issue, the recording of the holograms requires the variation of exposure in the interference pattern, which must stay within a linear region of the $t_A(x,y)$ vs exposure curve. Also, during recording the holograms, a light source with plane wavefronts is required not to contaminate the object details in the holograms with the light source information, and the plane wavefronts can be generated by a monochromatic point light source at infinity. The mentioned concerns prevent the widespread use of optical holography.

2.7 Diffraction efficiency of the holograms

The maximum diffraction efficiency of the holograms relies on the number of discrete phase levels in the CGHs, and the theoretical maximum diffraction efficiency is computed with Eq. 2.23 where n is diffraction order, and M is the number of phase levels. The holograms with binary phase levels can provide a maximum diffraction efficiency of 40.5%, while the holograms with four-phase levels allow an efficiency up to 81% [116]. The diffraction efficiency of the holograms shown on phase-only SLMs is maximal if the SLMs modulate the phase of the diffracted beam in a range between 0 and 2π. Yet, this ideal modulation range cannot be kept due to dispersion of the SLMs when operating wavelength changes or a broadband beam is utilized. This case leads to a lower diffraction efficiency and formation of an undesired intense zero diffraction order [117].

$$\eta = sinc^2\left(\pi n/M\right) \tag{2.23}$$

The performance of the CGHs improves with the number of CGHs pixels [118]. Also, when CGHs are developed for different wavelengths and incident angles of light, these parameters should be taken into consideration to enhance the overall performance of the CGHs. Unfortunately, computational and experimental design duration for the CGHs increases in parallel with the number of optimization parameters: the number of wavelengths of light sources, the number of incident angles of the light sources, and the number of CGHs pixels, etc. Considering the wide-area implementation of optical holography for retrieving object/hologram information and generating a holographic image, a versatile methodology with a short design/optimization duration is highly required. The CGHs can be optimized within a short design duration with enhanced performance by developing intelligence design approaches.

2.8 Theoretical glance on deep learning

Here, fundamental tools that play essential roles in designing a deep learning model are shared to understand the concept of deep learning fully. Many different deep learning structures exist as Artificial neural networks (ANN), Convolutional neural networks (CNN), Residual neural networks (RNN), etc. In this thesis, we concentrate on CNN architecture which is developed to process data that has a grid-like topology such as 2D images [95]. A typical CNN consists of many layers for convolution operation, activation function, pooling, fully connected, and dropout. Below details of them are given to be aware of the concept of deep learning.

2.8.1 Convolutional layer

The convolutional layers are a CNN's core building blocks that use convolution operation (represented by *). A convolutional layer catches features encountered within local regions of the input data that are joint throughout the input data. Convolution is a mathematical process conducted with two functions, and convolution operation is a matrix multiplication to extract helpful information from the input data. Convolution operation can be applied to images to achieve various transformations on the input images and provide feature maps. An example of a two-dimensional filter, a two-dimensional input, and a two-dimensional feature map are indicated in Fig. 2.2. This convolution operation is represented by $A * K$ and is mathematically given with Eq. 2.24. By utilizing a 2D image A and a 2D filter K, a 2D feature map F is received with Eq. 2.24. Here, the image A is convolved with the filter K, and the image builds the feature map F.

$$F(i,j) = (A * K)(i,j) = \sum_{m}\sum_{n} A(m,n)K(i-m, j-n) \tag{2.24}$$

Parameters of a convolutional layer are a set of learnable filters known as weights/kernels. The weights in each convolutional layer establish the convolution filters. Due to the complexness in the input images, there may be numerous filters in each convolutional layer. Each filter is slid across the width and height of input images, and feature

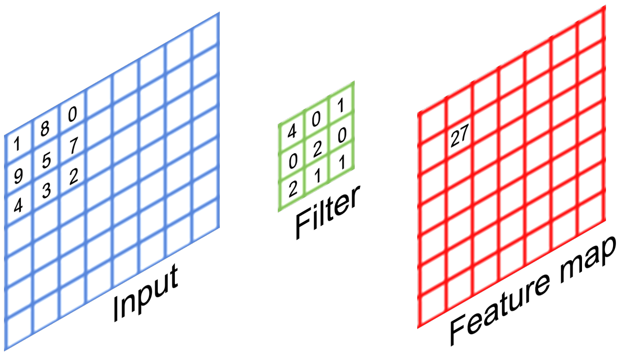

Figure 2.2: A sketch demonstrates a convolution operation on a 7-by-7 input matrix with a 3-by-3 filter to generate a feature map.

maps of that filter are induced. These feature maps show common characteristics like edge, corner, etc., in the input images.

Due to convolution operation, CNNs have three essential features: local receptive field, weight sharing, and subsampling. The input area used by a filter is called the local receptive field. Owing to the local receptive field, each weight can only link to a small region of the input data. This situation is accomplished by making the filter/weight matrix smaller than the input. With the local receptive field, neurons can extract elementary visual attributes like edges, corners, endpoints, etc. The size of the receptive field is the same as the size of the filter. Weight sharing means utilization of the same filter/weights for all receptive fields in a layer. In CNNs, since the filters' size is smaller than the input size, each filter is employed at every input position. Subsampling decreases the spatial dimension of the input data; thus, subsampling lowers the parameters in the network. There are few subsampling approaches available, and their details are noted later.

The CNNs architecture has many hyper-parameters used to regulate the performance of the model. Some of these hyper-parameters adjust the size of the output, while some are employed to adjust the model's running time and memory expense. The four noteworthy hyper-parameters in the convolution layer of the CNN are delivered below:

- Filter Size: A filter can be of any size greater than 2×2 and less than the input data size. The size of the filter is independent of the size of the input.

- Number of Filters: There can be any reasonable number of filters, but that causes to increase in the computational cost of a model.
- Stride: It is the number of pixels to move at a time to determine the local receptive field for a filter. Stride of one means to move across and down a single pixel. The value of stride should not be too small or too large. Too small a stride will cause heavily overlapping receptive fields, and too large a value will overlap less, and the resulting output volume will contain spatially smaller dimensions.
- Zero Padding: This hyper-parameter expresses the number of pixels to pad the input image with zeros. Zero padding is employed to manage the spatial size of the output volume.

2.8.2 Activation functions

The output of each convolutional layer is provided to an activation function layer. The activation function layer consists of an activation function that accepts the feature map made by the convolutional layer and yields the activation map as its output. The activation function is utilized to convert the activation level into an output signal. It sets the provided input to the output of the neuron. The activation function usually has a squashing effect which takes an input (a number), functions some mathematical operation on it, and outputs the activation level of a neuron between a given range 0 to 1 or -1 to 1.

Rectified Linear Unit (ReLU) is the most famous activation function for deep neural networks. The neural networks with the ReLU activation function train much quicker than others. The ReLU thresholds the input at zero. In other words, the ReLU delivers output 0 if the input is less than 0; otherwise, the ReLU delivers raw output value. It is mathematically shown with Eq. 2.25 and plotted as in Fig. 2.3a.

$$f(x) = \max(0, x) \tag{2.25}$$

The hyperbolic tangent activation function (tanh) is another activation function that provides outputs lie in the range [-1, 1]. The negative inputs to the tanh give negative numbers, and the positive inputs produce positive numbers as shown in Fig. 2.3b.

The sigmoid activation function is similar to the hyperbolic tangent activation function. It is mathematically described with Eq. 2.26, and it squashes the input values between [0, 1] as seen in Fig. 2.3c.

$$\sigma(x) = \frac{1}{1 + \mathrm{e}^{-x}} \tag{2.26}$$

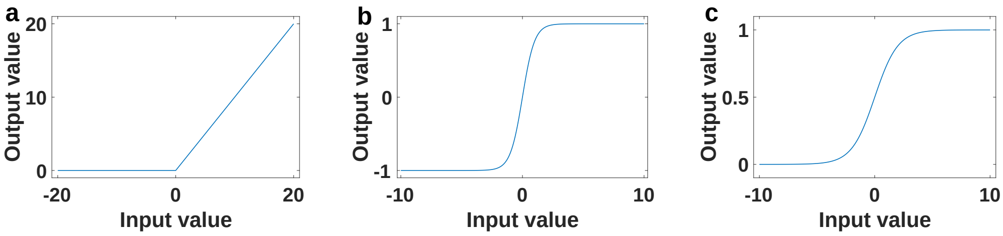

Figure 2.3: Outputs of three activation functions: (a) ReLU, (b) Tanh, (c) Sigmoid.

Softmax classifier is another activation function that is a mathematical function accepting an input vector and producing an output vector in a range between 0 and 1. The components of the output vector add up to 1. That is, the sum of all the outputs of the softmax function is 1. The softmax function is defined with Eq. 2.27 where $S\left(y_i\right)$ is the output of the classifier, and y_i is the input of the classifier. Since the softmax function outputs probability distribution, it is useful for multiclass classification in the final layer of deep neural networks.

$$S\left(y_i\right) = \frac{\mathrm{e}^{y_i}}{\sum_i \mathrm{e}^{y_i}} \tag{2.27}$$

2.8.3 Pooling

In a CNN architecture, the series of convolution layers and activation function layers are tracked by an optional pooling or down-sampling layer to decrease the spatial size of the input. In the meantime, the number of parameters in the network reduces.

The pooling layer summarizes a region of neurons in the previous layer and discards irrelevant neurons. There are few pooling methods available, and the most common pooling process is max-pooling. Max-pooling outputs the highest value in a subset of the previous layer output.

2.8.4 Fully connected layer

Each neuron from the previous layer is connected to every neuron in the next layer with a fully connected layer. Therefore, every neuron contributes to predicting how strongly a value matches a particular class. The fully connected layers can be stacked to learn even more sophisticated combinations of features. There can be more than one fully connected layer, and the output of the last fully connected layer is provided to a classifier that outputs the class scores.

2.8.5 Dropout

The fully connected layers are prone to overfitting, which refers to a problem when the model operates so well on training data, but the model's performance is low on new data. As a result, the model does not show generalizability. The dropout layer notably diminishes overfitting and enhances the generalization of the model.

A dropout layer can be introduced to a model where some neurons and connections are randomly dropped during training. Incoming and outgoing edges to a dropped-out node are also removed, leaving a reduced model. Only the reduced network is trained with the data in that stage. The removed nodes are then reinserted into the network with their original weights after the training, and the model's performance is assessed.

2.8.6 Cost function

A cost function is employed to compute the error (difference between prediction and ground truth labels) during the training process of a deep network. The weights of a network are then updated with their respective gradients. Depending upon applications, cost function changes. Here, the details of mean squared error and cross-entropy losses are shared for regression and classification problems.

2.8.6.1 Mean squared error loss function

The most commonly utilized loss function is Mean Squared Error (MSE) loss function. The MSE function, also known as L2 loss function, computes the squared average error of all the individual errors E, and is delivered with Eq. 2.28 where e_i equals to $\mathrm{target}(i) - \mathrm{output}(i)$ that denotes the individual error of ith output neuron.

$$E = \frac{1}{n} \sum_{i=1}^{n} \mathrm{e}_i^2 \tag{2.28}$$

2.8.6.2 Cross-entropy loss function

Cross-entropy loss is another loss function mainly employed in regression and classification problems. Cross-entropy loss is given with Eq. 2.29 where y_i' is the target label, and y_i is the output of the classifier. The cross-entropy loss function is utilized when the output is a probability distribution, and thus it is the preferred loss function for softmax classifier.

$$H(y) = -\sum_{i} y_i' \log\left(y_i\right) \tag{2.29}$$

CHAPTER 3

SPECTRALLY SPLITTING AND SPATIALLY CONCENTRATING THE BROADBAND LIGHT

3.1 Introduction

Miniaturized optical elements are an advancing research field aimed to reduce the size, weight, and cost of optical systems while enhancing their performance for various application areas. Controlling light phase, polarization [122], and absorption [123] in a medium with these optical elements provide superior results in spectroscopy [124], sensing [125], wavelength demultiplexing [126], particle tracking [127], imaging [128], image classification [129], quantum computing [130], and especially solar energy harvesting applications [131]. Traditional optical elements for controlling light, such as lenses, mirrors, lamellar gratings, etc., are too bulky and expensive for large-scale applications. However, modern approaches for using spatially controlled pixels close to the wavelength of light drastically increase our ability to control light. With the rise in energy demand, intelligent conversion of solar energy using miniaturized optical elements is becoming more demanded for superior performance and lowering the cost of solar modules.

Solar energy is one of the renewable energy sources, provides clean and sustainable energy [132, 133, 134, 135, 67]. The day-by-day growth of energy demand leads to an acceleration of research on the effective conversion of this energy source. Current research of solar cell technology focuses on improving the performance of solar cell materials. However, the theoretical conversion efficiency of the solar cells (30%) for

---

This chapter is published as three journal papers and two conference proceedings, see Refs. [8, 119, 84, 120, 121].

a single-junction is limited by spectrally bounded absorption of single-junction solar cells [136]. The small overlap between the emission spectrum of the sun and the absorption spectrum of a solar cell causes inefficient use of available energy. Also, that leads to the generation of thermal energy instead of electricity. There are a variety of solar cell materials to trigger the generation of electricity. Still, the amount of converted energy is low due to this small overlap of the spectra attained by solar cells and daily/seasonally variation in the incident angle of the sunlight.

Solar energy can be more effectively converted to electricity using smart design schemes. Ground-breaking performance is especially obtained with solar cells fabricated via tandem architecture [137]. However, the tandem solar cells are costly to fabricate due to the complicated epitaxial growth procedure of multiple layers that impose constraints on design and performance. In addition to enhancing the performance of the solar cell materials and design architectures, concentration, tracking, and spectral splitting of the sunlight are the main routes to increase solar energy from the solar cells. Laterally arranged solar cells system has a strong potential in the generation of electricity after incorporating spectral splitting elements [138, 139]. Laterally arranged solar cells that are made from two or more different materials produce increased energy output by enhancing spectral overlap between the absorption spectra of solar cells and the incident spectrum of the sunlight with the help of spectral splitting elements [67, 46, 68, 69, 13].

Spectral and spatial control of light has a strong influence in central fields such as imaging [1, 2], projection [140], sensing [3], communications [4], and solar energy [12, 13, 14, 15, 16] which directly affect the advancement of humanity. The commonly used spectral splitting methods involve prisms, dichroic mirrors [13], combinations of prism-cylindrical lenses, and phase plates [141, 121]. Among these elements, the phase plates have huge power to control light in both spatial and spectral domains [141, 142].

A phase plate can modulate direction, amplitude, phase, and polarization of the light or a combination of these properties, which makes them superior to conventional optical structures [19, 20, 21]. The multi-dimensional control provided by the phase plates yields to versatile performance increase in imaging [22], holography [5, 6], light focusing [7], spectral control [8], microscopy [9], aberration correction [10], wavelength-multiplexing [11], and solar energy [23]. Although the control on phase provides numerous advantages, the phase being sensitive at dimensions close to the wavelength of incident light brings extra challenges to overcome. The increased resolution requirement in designing the phase plates also increases the number of parameters to be optimized for efficient control of light. A diffractive optical element (DOE) is a special type of phase plate that modulates light by using diffraction and interference with preferably minimal light scattering [67, 46, 68, 69, 13].

The DOEs provide control over intensity, polarization, wavefront, and phase distribution of light with a high degree of freedom [8, 23]. Their importance is proven in plenty of application areas of science from improving beam quality of a laser [41], controlling modes of a light source [42], suppressing speckle in a compact laser projection [43], increasing numerical aperture in a confocal microscopy [44], to enhancing the performance of solar cells [45, 46, 13, 47]. Their outperforming functionalities are mainly required in spectrally splitting broadband light as conventional lenses lack control in spectral-domain [8, 120, 23].

Compared to refractive structures, the DOEs eliminate chromatic aberration via design and optimization of the geometric variables of the structures [48]. A variety of the DOEs exist as fork grating [49], diffractive axicon [50] supplying an extended depth of focus compared to Gaussian beams, and blazed diffractive optic [51]. Thanks to recent developments in science and technology, fabrication of the DOEs becomes more accessible using photolithography [52], E-beam lithography [53], and direct laser writing [54].

Being versatile, low-weight, compact, easy-to-fabrication, and cost-effective, the DOEs successfully steer the incident light to a target position while simultaneously achieving spectral control of light. The DOEs can spectrally disperse the sunlight and steer individual spectral bands to the relevant target solar cells. We classify these multi-functional diffractive optical elements as spectral splitters and concentrators (SpliCons) [23] to distinguish from the DOEs that can only achieve spectral splitting.

There are several design approaches to tune the structural parameters of the DOEs/SpliCons. These are direct binary search [143, 144], Gerchberg-Saxton [145, 146, 147], and Yang-Gu algorithms [148], genetic optimization [149], the local search optimization [120], and gradient-based electromagnetic field optimization [54]. Gerchberg-Saxton [147, 16] is one of them with a Fourier transform-based algorithm that yields phase patterns in short calculation time. However, the algorithm generates the DOEs with a texture that needs impractical precision. The local search algorithm can find an optimum phase pattern for applications of interest, and the algorithm has increased flexibility in design parameters and fabrication limits [121, 8, 142]. Unfortunately, the computational time of these algorithms increases in parallel with the number of optimization parameters: the number of wavelengths of light sources, the number of incident angles of light sources, the number of DOE pixels, etc. Thus, these high number of optimization parameters result in a long computation time that seriously hampers their implementation [103]. However, their performance increases with the number of controlled parameters that form the structural design of the DOEs.

Instead of iterative approaches, the inverse design of DOEs/SpliCons can decrease the optimization time. However, the inverse-design presents several significant challenges compared to the iterative: i) phase plates in each frequency of broadband spectrum are needed, ii) combination of these phase plates will still require intermediate phase plates to obtain desired intensity distribution, iii) one-to-many mapping problem [55]. One-to-many mapping is a big problem because a data point may be associated with multiple labels instead of a single class [56, 57]. Thus, spectrally splitting and concentrating the light using the inverse design is still an unaddressed challenge. The neural network architecture of deep learning could figure out one-to-many mapping problem faced in the inverse-design of DOEs/SpliCons and provide fast and accurate control over light beams. Compared to the computational tools, deep learning offers a fast inverse design path for the DOEs/SpliCons.

Deep neural networks consist of multiple layers that connect input data to output data by revealing the correlation between the output and the input. Higher-level information within a data set, presented as weights of the layers, is captured. Therefore, complex network relations between the input and output data can be understood. Deep learning proves its adaptability and multi-operational behaviour in various tasks especially in photonics for designing nanophotonic devices [150, 151], anti-reflective surfaces [152], and photonics systems [153, 103, 84, 154]. Also, physics-informed neural networks can provide a better understanding of the underlying physics in various tasks [155]. Moreover, deep learning enables us to inverse-design a DOE/SpliCon within a short time with performance scores that are extremely close to the ground-truth values.

3.2 Computational design of diffractive optical elements

Here, we introduce a new optimization algorithm that outperforms the local search optimization algorithm. With the accommodation of our algorithm, transmissive DOEs are designed for two purposes: solar concentrator and spectral splitter with broadband light. In our model, we take material dispersion into account and the solar spectrum to provide a realistic structure. We manage to spectrally split and concentrate the solar energy into designated regions using a single DOE. Later, we introduce a bandwidth approach to optimize the DOE for every 13 nm wavelength step within the 400 nm - 1100 nm bandwidth. We observe that optimizing the DOE for every 13 nm wavelength step rather than a 1 nm wavelength step within the target bandwidth results in similar splitting efficiency while the bandwidth approach provides 11 times faster computation.

3.2.1 The local search algorithm

The local search optimization algorithm essentially adjusts only the thickness of randomly generated DOE pixels to direct chosen frequencies to the target spots. However, the algorithm is sensitive to the choice of initial conditions. If the DOE thickness profile generated leads to a weak diffraction efficiency, the optimization algorithm may experience premature convergence, or the optimization will last longer to converge to a satisfactory optimization state. Either to minimize or to eliminate these drawbacks, we propose the so-called *OR*, *AND*, and *MEAN* logic operations as optimization criteria for tuning an initially random DOE structure. Considering the logic operations as *OR*, *AND*, and *MEAN*, the algorithm updates the thickness profile of the DOE.

This part is published as a journal paper, see Ref. [8].

The local search optimization algorithm operates as follows: considering the size of the DOE, it generates a random 2D thickness profile (here 40-by-40 elements in the lateral size). Then, we calculate the diffraction pattern using Eq(s). [3.1-3.4] (details of equations explained below). Next, we calculate the spectral optical efficiency (SOE) and the enhancement for each design wavelength considering the diffraction pattern at the target. We define the SOE as the percentage intensity at the target area compared to the total intensity over the diffraction plane for a particular wavelength, see Eq. 3.5. The numerator of the Eq. 3.5 is the total intensity in the target area, and the denominator of the equation is the total intensity at the whole output plane. S is the area, and $I_{ab}(\lambda)$ is the light intensity at a wavelength of λ at a position (a, b) of the target plane. Also, enhancement is defined as the ratio of SOE after and before the DOE. The optimization algorithm alters the thickness of each pixel from minimum pixel thickness to maximum one while monitoring increases in SOEs and enhancements for all design wavelengths. Each thickness scanning attempt of all pixels is called a sub-iteration, and all sub-iterations continue until the performance parameters are evaluated for each thickness of all pixels. The thickness profile of the DOE is updated in case a criterion which can be either *OR*, *AND*, and *MEAN* is satisfied. As a decision-making logic, *AND* leads the algorithm to increase SOEs/enhancements of all design wavelengths during each sub-iteration. However, the algorithm with *OR* criterion rises at least one of two design wavelengths during each sub-iteration. Lastly, the algorithm with *MEAN* criterion updates the DOE thickness profile if the mean of SOEs of all design wavelengths increases during a sub-iteration. After the contribution of all pixels is evaluated with scanning all thicknesses, we proceed to scan all pixels again until the enhancements/SOEs reach saturation providing no further increase in enhancement.

The DOEs in this study have 1600 pixels (40x40) with an individual pixel size of $5\,\mu\text{m}$. A phase delay of an impinging coherent light at a wavelength of λ at the output plane $\phi_{pq}(\lambda)$ is proportional to the thickness profile of the DOE h_{pq}, and it is expressed in Eq. 3.1 where λ is the wavelength of the light source, $n(\lambda)$ the refractive index of the DOE, and h_{pq} the thickness of the DOE at a position (p, q). The spatial profile of the DOE is discretized to 8 levels with a $1\,\mu\text{m}$ step size in thickness. Spectral splitting and beam concentration by the DOE depends on the step size, and the spectral splitting efficiency increases with the number of step size as well as the number of pixels given the increased degrees of freedom to control. Here, the ultimate limit is set by the wavelength. Yet, fabrication of large-area DOEs at this precision, that is, the wavelength of light (400 nm), is not feasible. In this study, we choose a 1 µm step size since this level of precision is easily achievable using direct laser writing [156].

$$\phi_{pq}(\lambda) = 2\pi h_{pq}[n(\lambda) - 1]/\lambda, \tag{3.1}$$

$$U_{ab}(\lambda) = \sum_{pq} U_{pq}(\lambda) * G_{pq}, \tag{3.2}$$

$$U_{pq}(\lambda) = A_{pq}(\lambda) * \text{exp}\,[j\phi_{pq}(\lambda)], \tag{3.3}$$

$$G_{pq} = \left(\frac{1}{j\lambda d}\right) * \text{exp}\left(\frac{j2\pi d}{\lambda}\right) * \text{exp}\left[j\pi\frac{\{(y_{pq} - Y_{ab})^2 + (x_{pq} - X_{ab})^2\}}{\lambda d}\right], \tag{3.4}$$

$$SOE(\lambda) = \frac{\int_S^{Target} I_{ab}(\lambda) dS}{\int_S^{Outputplane} I_{ab}(\lambda) dS} * 100. \tag{3.5}$$

The output intensity profile of the DOE is calculated by using a discrete electric field summation presented in Eq. 3.2. $U_{pq}(\lambda)$ is the electric field distribution at wavelength of λ at the incident plane, $U_{ab}(\lambda)$ is the electric field distribution at wavelength of λ at the target plane, and G_{pq} is the kernel transformation function at coordinates (p, q) in Eq. 3.2. The electric field profile at the incident plane $U_{pq}(\lambda)$ and the transfer function G_{pq} are defined in Eq. 3.3 and 3.4, respectively. In Eq. 3.3, A_{pq} is the complex-valued amplitude of the incident light wave at coordinates of (p, q), $\phi_{pq}(\lambda)$ is the phase delay at a wavelength of λ after the DOE. In Eq. 3.4, (X, Y) and (x, y) represent the position of pixels at the target plane and the input plane, respectively, and d is the distance between the input and the output planes.

In our calculations, we position the DOEs parallel to the output, and we do not take polarization, Fresnel reflection, absorption, and internal reflections within the DOEs into account. We include the dispersion curve of BK-7 for the DOE material [157] and normalized the Blackbody radiation curve of the Sun at the surface temperature of 5778 K. The blackbody radiation curve of the Sun is obtained at 5778 K by using Planck's law, and it is normalized considering the peak spectral radiance of the Sun at that temperature. The distance between the DOE and diffraction plane is chosen as $350\,\mu\mathrm{m}$.

3.2.2 Results and discussion

The performance of the aforementioned logic operations in the local search optimization algorithm is inspected by two light sources at first. The main goal is to disperse the broadband spectrum into two regions between 400 nm - 700 nm and 701 nm - 1100 nm over target regions of size 0.1 mm - 0.2 mm, each. In the first step, we spectrally split 700 nm and 1100 nm, which are the higher limits of the bands between 400 nm - 700 nm and 701 nm - 1100 nm, respectively. Since phase modulation of longer wavelengths is harder to manage (require thicker media for phase control), we choose first to control the longer wavelengths. We manage to spectrally split 700 nm and 1100 nm using a single DOE with a maximum thickness of $8\,\mu\mathrm{m}$.

In Fig. 3.1a thickness profile of the DOE guiding two monochromatic waves of 700 nm and 1100 nm to targets as a result of *MEAN* criterion is seen. Positions of concentrated light at the target plane and SOEs of these light sources are shown in Fig. 3.1b. It is clearly seen that two wavelengths (at 700 nm and 1100 nm) are successfully directed to desired targets with 45% and 63% SOE, respectively.

We first inspect *OR* logic operation to design a DOE to guide two continuous light sources with wavelengths of 700 nm and 1100 nm on two targets. Fig. 3.2a shows the result of enhancements/SOEs when the optimization is performed with *OR* logic operation. The algorithm with the *OR* case updates the DOE profile when SOE/enhancement of either one or both two light sources increases at each sub-iteration. Therefore, at each sub-iteration, the algorithm finds another local maximum for each wavelength. We do not observe saturation of the enhancements/SOEs after eight iterations (takes 4.6 hours on a desktop PC), and we obtain maximum enhancements around five iterations. At the end of the optimization, we conclude that enhancements

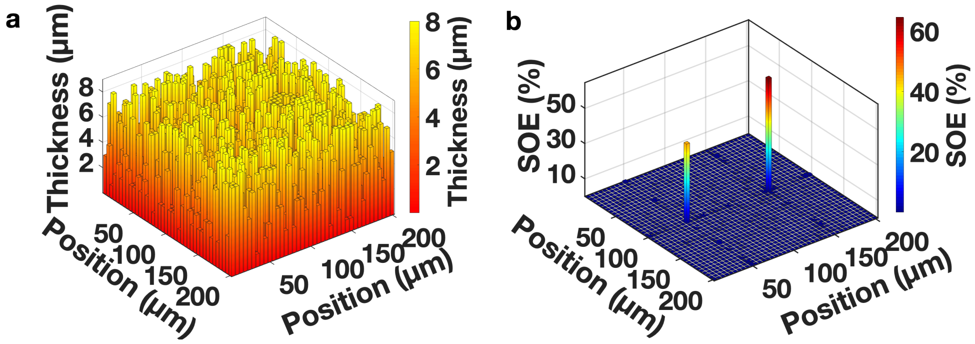

Figure 3.1: (a) Spatial distribution of DOE thickness for focusing two-color with the *MEAN* criterion (the optimization criterion is set to raise the mean of SOEs of two sources), (b) Distribution of SOEs of incoming light on the target plane. The 700 nm light is guided to the position of $(50\,\mu\mathrm{m}, 100\,\mu\mathrm{m})$ and of 1100 nm light is guided to the position of $(150\,\mu\mathrm{m}, 100\,\mu\mathrm{m})$. The incident light sources at 700 nm and 1100 nm are successfully focused with 45% and 63% SOEs, respectively. The figure is taken directly from Ref. [8].

of 303 and 316 are at wavelengths 700 nm and 1100 nm, respectively. In terms of SOE, we manage to direct 19% and 20% of the incident light at 700 nm and 1100 nm to a single pixel, respectively. The SOE values will increase if the target area is greater, which will be shown for the DOEs designed for broadband operation.

When DOE thickness profile is optimized with *AND* criterion at each sub-iteration, SOEs and enhancements at all design wavelengths are improved as seen in Fig. 3.2b. SOEs/enhancements at both light sources saturate at six iterations, and we concluded that 4 hours are sufficient to calculate an optimal DOE to concentrate two light sources with *AND* logic operation. At the end of the optimization, 676 and 656 enhancements (42% and 41% in terms of SOE) on the targets are achieved for 700 nm and 1100 nm, respectively.

Lastly, enhancements at two light sources with *MEAN* criterion are presented in Fig. 3.2c. The DOE thickness profile is updated when the average enhancement/SOE value at two light sources increases at each sub-iteration. That is, the mean value of SOE/enhancement of design wavelengths rises at each sub-iteration when *MEAN* criterion is applied to the algorithm. As expected, one of the two light sources is focused

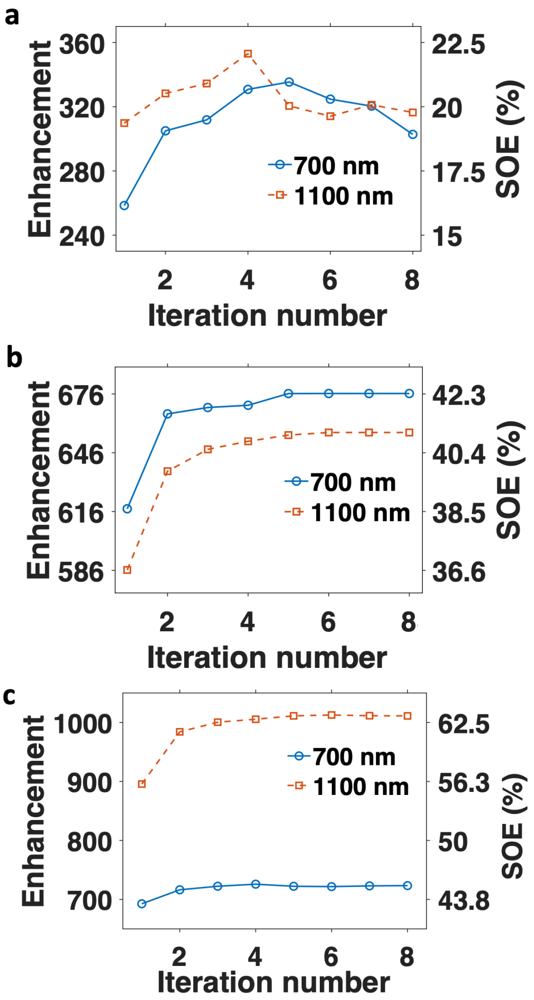

Figure 3.2: Results of (a) OR, (b) AND, and (c) MEAN logic operations. The blue circles represent the enhancement values for 700 nm, and the red squares represent enhancement values for 1100 nm light. The dashed and solid lines are guides to the eye. The figure is taken directly from Ref. [8].

more intensely than the other due to their mean increases at each sub-iteration. At the end of all the main iterations, enhancements of 723 and 1011 (45% and 63% in terms of SOE) are obtained for 700 nm and 1100 nm, respectively. Again SOEs/enhancements at both light sources saturate at the sixth iteration, and we concluded that 4 hours are sufficient to calculate an optimal DOE to concentrate two light sources with *MEAN* logic operation. It is observed that the *MEAN* criterion, among other logic operations, gives the highest average SOE/enhancement for these light sources (see Table 3.1). The enhancements we get here are approximately ten times better than the results obtained with the Gerchberg-Saxton algorithm using the same physical parameters for the DOE (a single-pixel concentration after eight iterations).

Table 3.1: Result of three logic operations for spatially concentrating and spectrally splitting the dichromatic light source.

Logic operation	**Enhancement at 700 nm**	**Enhancement at 1100 nm**
OR	303	316
AND	676	656
MEAN	723	1011

The ultimate pixel number is defined by S/λ^2, where S is the area of a DOE. Here, we use 1600 pixels (40x40) for our DOEs. The SOEs and enhancements values will undoubtedly increase with more pixels [118]. However, this would be beyond the precision limits of fabricating DOEs for the solar cells. Moreover, we obtain better SOE for the longer wavelength. It is expected that control over longer wavelengths is more problematic given that a thicker medium is required for getting a similar phase shift when compared to a shorter wavelength. However, in our case, we choose a $1\,\mu\mathrm{m}$ step size in DOE thickness optimization. This resolution is coarse for the shorter wavelength, whereas the thickness step size is sufficiently small for the long wavelength. As a result, both the SOE and the enhancement values are greater for the longer wavelengths. Here, we chose the number of pixels, DOE dimensions, and resolution limits considering the direct laser writing process, which can be applied to large-scale fabrication. The greater enhancement over the shorter wavelengths is definitively possible using more precise fabrication methods [156].

Next, we perform similar calculations to guide the same light sources (700 nm and 1100 nm) on a larger target (0.1x0.2 mm). The larger target area inherently involves more degree of freedom for the spectral splitting of the broadband light source. For this purpose, we use *AND* and *MEAN* logic operations. With the *MEAN* criterion, 700 nm and 1100 nm sources are focused with higher SOEs: 92% and 94%, respectively (Fig. 3.3). In Fig. 3.3a the DOE thickness profile is presented. In sub-figures (b) and (c) of Fig. 3.3, we present the distribution of light source at the target plane. We see that the light source at a wavelength of 1100 nm accumulates at the right half area of the target plane in Fig. 3.3b as planned. Simultaneously, the light source at a wavelength of 700 nm accumulates at the left half area of the target plane in Fig. 3.3c. In these sub-figures, it is obviously seen that the distribution of light outside the target areas is considerably weak, and amounts of light percentage outside the target areas are 8% and 6% for 700 nm and 1100 nm, respectively.

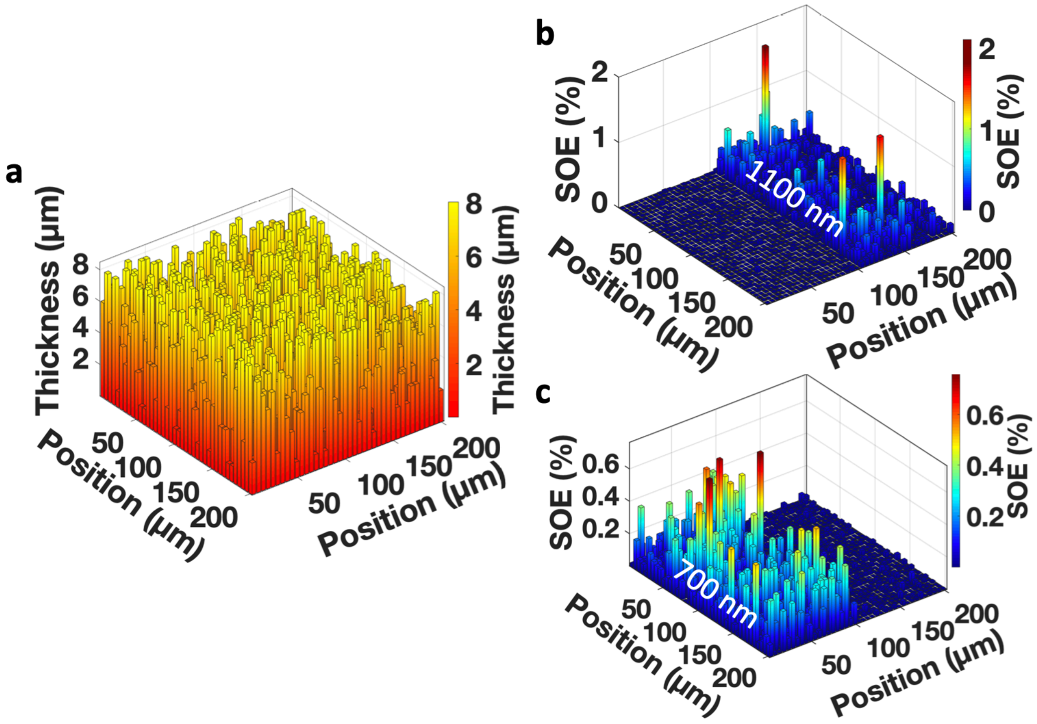

Figure 3.3: (a) DOE thickness profile, (b)&(c) Distributions of SOE at the target plane for two monochromatic light sources using *MEAN* criterion. (b) Distribution of SOE of a light source at 1100 nm. The light source is directed at the right half of the target plane. The cumulative SOE over the target is 94%. (c) Distribution of SOE of a light source at 700 nm. The light source is directed at the left half of the target plane. The cumulative SOE over the target plane is 92%. The figure is taken directly from Ref. [8].

Optimizing a DOE for broadband light is quite a challenge. Using a 1 nm wavelength step between 400 nm - 1100 nm with 40x40 pixels, each of which can obtain eight different thickness values results in minimum 9×10^6 variables to optimize, and this number grows exponentially with an increased number of optimization variables. The calculation of such optimization will take approximately 89 days on a desktop PC, which is computationally expensive for optimizing DOEs.

Here, we introduce the effective bandwidth approach to overcome the extremely lengthy computational duration. For this purpose, we first design a DOE for 1100 nm and then calculate its response for various input wavelengths. Fig. 3.4 shows the output spectrum of the DOE designed for 1100 nm. As can be seen in Fig. 3.4, the DOE has a response bandwidth of $\Delta\lambda$=26 nm (FWHM). In our bandwidth approach, we will incorporate half-width at half maximum (HWHM, $\Delta\lambda$=13 nm) as our wavelength step in the optimization process instead of optimizing the DOE at every 1 nm. As a result, the calculation time dramatically decreases while the performance of the DOE remains unaffected.

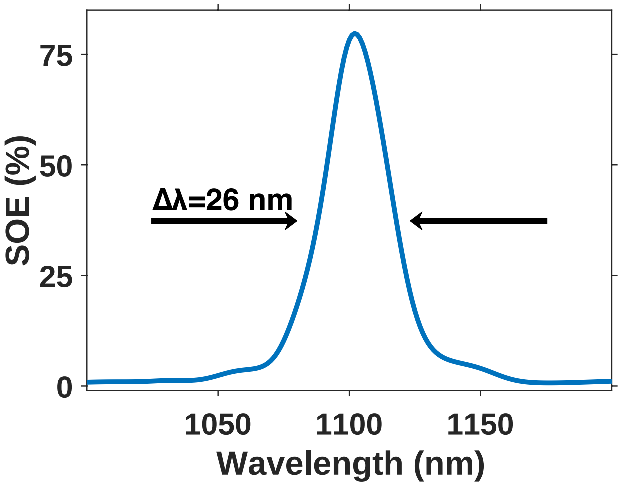

Figure 3.4: The broadband response of the DOE is designed for guiding light source at a wavelength of 1100 nm on a single pixel at the output plane. The figure is taken directly from Ref. [8].

To test the effectiveness of our bandwidth approach, we concentrate input wavelengths between 1051 nm and 1100 nm. We first optimize a DOE using a 1 nm wavelength step size, and then we compute another DOE with the bandwidth approach: a 13 nm wavelength step size. Later, the performance of both DOEs is tested under broadband illumination. The results are provided in Fig. 3.5. We observe that our bandwidth approach demonstrates similar results to the DOE optimized with a 1 nm wavelength step size. The reason is that the 1 nm wavelength step size intro-

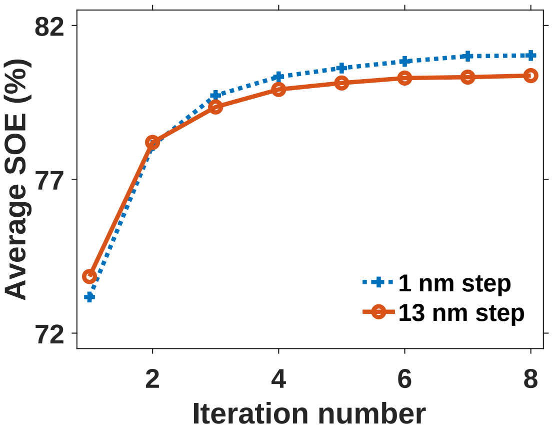

Figure 3.5: Evolution of average SOEs for band 1051 nm - 1100 nm with the bandwidth approach, which is 13 nm wavelength step size (red solid lines) and with a finer wavelength step size of 1 nm (blue dashed lines). The solid and dashed lines are guides to the eye. The figure is taken directly from Ref. [8].

duces too many parameters to optimize, and the optimization algorithm gets stuck in a local maximum rather than reaching a global maximum. With the bandwidth approach average SOE for the light band, 1051 nm - 1100 nm shows a similar value with the 1 nm wavelength step at each iteration. Thus, using the effective bandwidth approach, we are able to overcome the extensive computational time while retaining the performance.

Using a bandwidth of 13 nm, 54 distinct wavelengths between 400 nm - 1100 nm are controlled to direct wavelengths of light to a specified position at the target plane. To obtain a broadband DOE with these light sources, we use the *MEAN* criterion. The algorithm uses the average SOE of wavelengths between 400 nm - 700 nm as well as the average SOE of wavelengths within 701 nm - 1100 nm to optimize a single DOE structure. Considering a 13 nm step in wavelength, a single broadband DOE is obtained to spectrally split the broadband light within only eight days calculation time. Fig. 3.6 shows SOEs at each design wavelength. As a result of this study, the average SOEs of sub-bands are obtained as 56% for the band: 400 nm - 700 nm and 62% for the band: 701 nm - 1100 nm. The same figure presents the result of the same DOE used to spatially separate the broadband light with a 1 nm resolution. Average SOEs for the sub-bands between 400 nm - 700 nm and 701 nm -1100 nm are 56%

and 63%, respectively. Therefore, we conclude that the DOE designed for splitting 54 design wavelengths performs similarly with 701 wavelengths when illuminated with broadband light, as can be seen in Fig. 3.6.

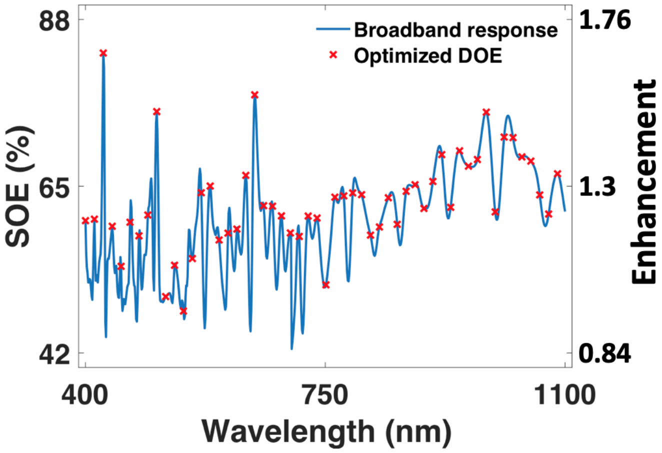

Figure 3.6: Wavelength-selective SOE and enhancement of a broadband DOE optimized with a 13 nm wavelength step to disperse the broadband light. The red cross points show SOE at each design wavelength. The blue solid line represents the broadband response of the same DOE with a 1 nm wavelength step. The figure is taken directly from Ref. [8].

In Fig. 3.7a the distribution of wavelengths of light sources having the highest SOE on each target pixel is demonstrated. Fig. 3.7a shows that we can spectrally split broadband light using our effective bandwidth approach. The separation of colors is distinctly visible at the target plane. In Fig. 3.7b quantitative value of SOE at each wavelength is presented. Blue dashed line peaks in the sub-band 400 nm - 700 nm at the blue region of the target plane and dips at the red region of the target plane. Red continuous line peaks in the sub-band 701 nm - 1100 nm at the red region of the target plane and dips at the blue region of the target plane. The average SOEs of sub-bands are obtained as 56% for the band: 400 nm - 700 nm and 63% for the band: 701 nm - 1100 nm.

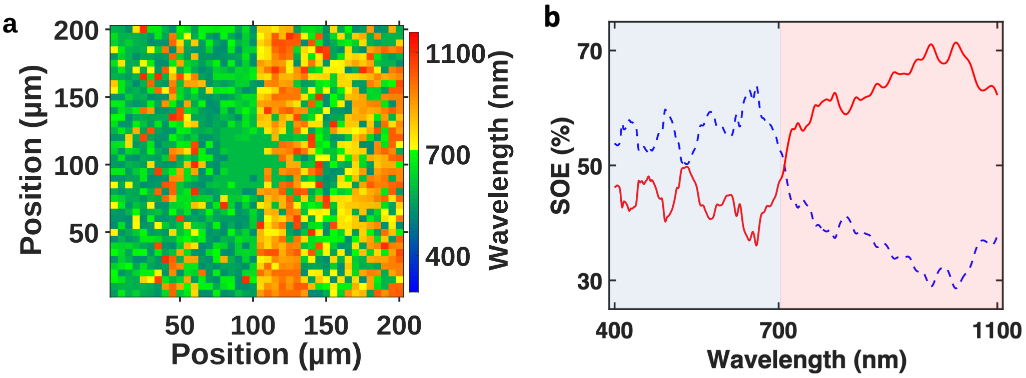

Figure 3.7: (a) The distribution of wavelength of the broadband light source having the highest SOE over the target. Each target pixel represents the wavelength of a monochromatic light source having maximum SOE on the corresponding target, (b) SOE at each wavelength using an optimized DOE with a 13 nm wavelength step. Blue dashed and red solid lines show SOE of each light source. The figure is taken directly from Ref. [8].

3.3 Deep learning-based diffractive optical elements

Here we present a hybrid design algorithm that combines deep learning and the local search optimization algorithm to speed up the optimization duration and enhance the DOE & SpliCon topography. We created a training data set to develop a deep learning model through optimization of a DOE/SpliCon with the local search optimization algorithm, which is a one-time effort. Using the DOEs/SpliCons generated via the local search optimization algorithm, we calculate the spatial and spectral distribution of the intensity pattern via the Fresnel-Kirchhoff diffraction integral at the target. Then we use deep learning-based optimization to reconstruct DOEs/SpliCons, which provides a much faster optimization. After that, we use hybrid optimization to further improve the performance of the DOEs/SpliCons for spectral splitting and spatial concentration of the broadband light. Our hybrid optimization procedure provides *fast* and *efficient* design of SpliCons for solar energy applications.

This part is published as a journal paper, see Ref. [119].

3.3.1 Method

3.3.1.1 The data set

We generate data sets for (i) concentrating dichromatic light source at two targets of the output plane with SpliCons, (ii) spectrally splitting the broadband light at two regions of the output plane with a broadband DOE, and (iii) spectrally splitting and spatially concentrating the broadband light at two target spots located at the output plane with a broadband SpliCon. For data set generation, we employed the Fresnel-Kirchhoff diffraction integral to calculate an intensity distribution formed by a DOE/SpliCon at the target plane, which is illuminated by a continuous plane wave. While optimizing a DOE/SpliCon, we used the local search optimization algorithm. The decision-making logic of the local search optimization algorithm is the AND, which improves fractional intensities at the targets at each wavelength/band simultaneously [8]. Training data set generation takes 26 minutes per design wavelength on a PC, which is a one-time effort.

Square-shaped DOEs/SpliCons are designed with a side length of $200\,\mu\mathrm{m}$. The DOEs/SpliCons consist of 1600 pixels with a $5\,\mu\mathrm{m}$ pixel size. The DOEs/SpliCons have multilevel discrete pixels where thickness profile varies spatially between $1\,\mu\mathrm{m}$ and $8\,\mu\mathrm{m}$ with a $1\,\mu\mathrm{m}$ step size. The design parameters of the DOEs/SpliCons are chosen based on what could be fabricated and used in compact solar cell modules. The distance between a DOE/SpliCon and an output plane is $350\,\mu\mathrm{m}$ to keep the diffraction pattern within the Fraunhofer field. For evaluating the performance of a DOE/SpliCon, we use spectral optical efficiency (SOE) at a wavelength as a metric that defines percentage intensity at the wavelength at a target of the output plane (see Eq. 3.5).

We create our training data set while concentrating dichromatic light source at wavelengths of 700 nm and 1100 nm on two individual pixels at the output plane as seen in Fig. 3.8a-b. Since phase modulation of a longer wavelength requires a thicker medium for phase control, we first chose to control the longer wavelength limits of the two bands that are chosen between 400 nm - 700 nm and 701 nm - 1100 nm. After optimization of a SpliCon, the algorithm yields 12800 distinct SOE profiles (Fig. 3.8a-b) and SpliCons (Fig. 3.8c). Then, the same dichromatic light source is concentrated to 25 alternating target positions. The output plane with size of 200 µm x 200 µm is pixelated, and size of a pixel is 20 µm x 20 µm at the output plane.

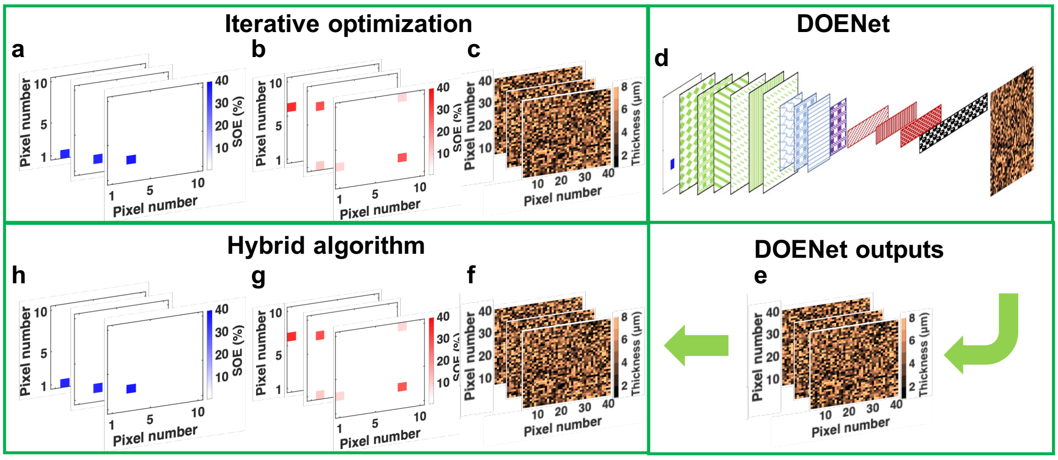

Figure 3.8: The flowchart of our hybrid algorithm. Input data sets which are SOE distributions at (a) 700 nm and (b) 1100 nm at the output plane for alternating target positions; (c) The SpliCons that produce the output patterns shown in (a) and (b); (d) The DOENet architecture. The first square shape represents intensity distributions input to the model. The following square shapes in the scheme are for extracted features through the DOENet. Each green square represents extracted features after a CNN layer with a ReLU activation function. Then, a max-pooling is performed, and the size of extracted features is reduced to half of the size of the input intensity distributions. Each blue square represents extracted features after a CNN layer with a ReLU activation function is performed. Then with a second max-pooling operation, the size of extracted features is again reduced. Violet square indicates extracted features after a CNN layer with a ReLU activation function. The first red rectangle represents extracted features after flattening extracted features in violet square and utilizing a dense layer with a ReLU activation function. The following two red rectangles represent extracted features after a dense layer with a ReLU activation function. After a drop-out and a dense layer, features are presented with a black rectangle. Then reshaping and softmax activation operations are performed before correlating extracted features with SpliCons (see details of the DOENet architecture); (e) DOENet outputs: reconstructed SpliCons; (f) Optimized SpliCons with the hybrid algorithm; Calculated SOE distributions of the SpliCons shown in (f) for input wavelengths (g) at 1100 nm, (h) at 700 nm. The figure is taken directly from Ref. [119].

Later we designed a broadband DOE to disperse the broadband light (400 nm - 1100 nm) into two bands that are the visible band (400 nm - 700 nm) and the short-IR band (701 nm - 1100 nm) on two regions at the output plane. The target region size is $100\,\mu\mathrm{m}$ x $200\,\mu\mathrm{m}$ for each band. Lastly, we optimized a broadband SpliCon to spectrally split the broadband light into the visible band and the short-IR band and simultaneously spatially concentrate on a target with a size of $50\,\mu\mathrm{m}$ x $100\,\mu\mathrm{m}$ for each band. The size of each pixel at the output plane is $5\,\mu\mathrm{m}$ x $5\,\mu\mathrm{m}$ for the broadband DOE/SpliCon. We use the bandwidth approach in our initial designs to minimize the computation time [8]. The bandwidth approach reduces the number of design wavelengths from 701 with a 1 nm wavelength step to 54 with a 13 nm wavelength step using the DOE/SpliCon dimension and resolution that we employ here. During the optimization, we improve the mean SOE at each band simultaneously at each iteration, so we decrease the degree of freedom in optimization for choosing proper DOE/SpliCon profile while keeping the performance of the DOE/SpliCon same. Through the optimization of the broadband DOE/SpliCon, the algorithm yields 12800 distinct DOEs/SpliCons and corresponding SOE distributions as a data set for developing a deep learning model.

3.3.1.2 Deep learning model: the DOENet

Fresnel-Kirchhoff diffraction integral is a vital tool to compute diffracted light patterns by a DOE/SpliCon. Tuning the topography of a DOE/SpliCon is a suitable problem that can be addressed using convolutional neural network (CNN) layers. Thus, in our deep learning model, we employed CNN layers to mimic relations between an intensity distribution of formed diffraction pattern and a corresponding DOE/SpliCon. The scheme of our deep learning model is presented in Fig. 3.8d that includes multiple CNN layers. The model has a sequence of 10 CNN layers, each of which has 64 filters with a filter size 3 x 3, three max-pooling layers, and four fully connected layers. The CNN layers have valid-padded convolutions. Between each CNN layer, the ReLU activation function is accommodated to ignite nonlinearity which is also seen between a DOE/SpliCon and its intensity distribution. This activation function squashes the intensity distribution by performing a mathematical operation that gives input value if the input value is greater than zero; otherwise, the ReLU gives zero.

Then, down-sampling with max-pooling is performed to reduce the spatial size of the intensity distributions after the 6th and 9th CNN layers. The number of parameters and computation load in the network are reduced after each max-pooling. Then, a flattening operation is performed to reshape extracted features. Later, three fully connected layers with 1600 units and three ReLU activation functions are used in our model, which concatenate features from all previous layers. Then another fully connected layer with 12800 units is employed to make the size of extracted features the same as the size of the output data (the DOEs/SpliCons). The fully connected layers eliminate extracted information after each CNN layer to wash out by time due to an intensity distribution that passes through many layers in the deep learning model. The fully connected layers link to all extracted features, and they are prone to over-fitting. Here, we use a dropout with a factor of 0.2 to eliminate over-fitting during the training before the last fully connected layer. Lastly, we reshape the size of extracted features into 40-by-40-by-8 to easily correlate them with the output data. We call our deep learning model diffractive optical element neural network (DOENet).

We normalized the intensity distributions obtained by the DOEs/SpliCons to arrange intensity values of the pixels between 0 and 1. The DOEs/SpliCons were converted to one-hot vectors with eight classes due to the eight-level thickness variation of a DOE/SpliCon. We call Keras, Tensorflow, and Numpy libraries to access deep learning operations and mathematical tools. We used the ADAM optimizer to minimize categorical cross-entropy loss function over the training samples. Through searching the weights of the model, we select a batch size of 100. Training of the model is completed in less than an hour using the Tensorflow library and an NVIDIA Quadro P5000 GPU. Once the training is completed, we test our model with validation data set, which is 10% of the input data set that is not part of the training set. The validation data set prevents the over-fitting of the network model to the training set. Compared to the local search optimization algorithm, the design duration of a DOE/SpliCon for concentrating the dichromatic light via the DOENet decreases from 52 minutes to a few seconds after training the model. The decline in design time is significant for broadband light that typically takes 24 hours using the local search optimization algorithm. The DOENet speeds up the design of a broadband DOE/SpliCon thickness profile from 24 hours to a few seconds.

3.3.1.3 The hybrid algorithm

The flowchart of the hybrid algorithm is described for concentrating the dichromatic light source in Fig. 3.8. The hybrid algorithm operates as follows: first, a DOE/SpliCon is reconstructed for light intensity distributions at two design wavelengths by using the DOENet (Fig. 3.8e). Then, the reconstructed DOE/SpliCon is further redesigned with the local search optimization algorithm and Fresnel-Kirchhoff diffraction integral (Fig. 3.8f). During further optimization, the local search optimization algorithm increases SOEs at two design wavelengths simultaneously at each thickness change attempt. Further optimization of the DOE/SpliCon is carried out for only one iteration, which lasts 52 minutes. By using the further optimized DOE/SpliCon, we obtained the SOE distributions at two design wavelengths (Fig. 3.8g-h). The same flowchart is extended to design a broadband DOE/SpliCon with our hybrid algorithm.

3.3.2 Results and discussion

3.3.2.1 SpliCons for Dichromatic Light

The local search optimization algorithm arranges pixel thicknesses of the SpliCons. At the end of optimization, the dichromatic light source is concentrated on two target pixels at the output plane. Later, the same light source is focused on alternating target positions with the same algorithm as seen in Fig. 3.8a-b. The SpliCon thickness profiles are presented in Fig. 3.8c. As a result of the local search optimization algorithm, we obtain a mean 35.6 ± 2.0% SOE at 700 nm and a mean 31.8 ± 2.7% SOE at 1100 nm on an individual pixel at the output plane (Fig. 3.9, Table 3.2). We concentrate the dichromatic light source on a pixel with a 100 times smaller area than the total area of the output plane. As expected, the highest enhancement we reach after optimization of a SpliCon is 100. However, due to selected optimization parameters such as the number of design wavelengths, the distance between the input and output planes, pixel size of the SpliCons, we obtained a mean 35.6 ± 2.0 enhancement at 700 nm and a mean 31.8 ± 2.7 enhancement at 1100 nm at the output plane.

After training the deep learning model, the DOENet (Fig. 3.8d), the model yields

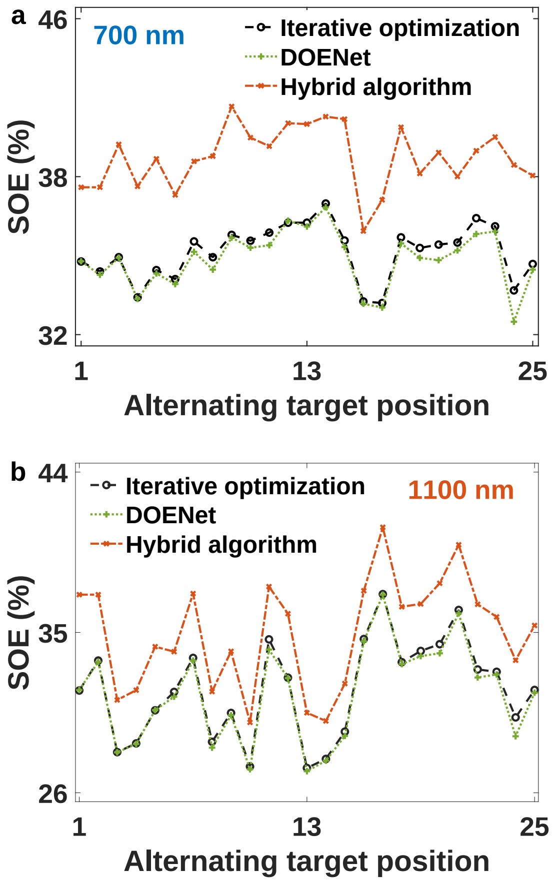

Figure 3.9: Concentrated light intensities in terms of SOE on alternating target positions computed for SpliCons which are obtained by the iterative algorithm, the DOENet, and the hybrid algorithm. (a) At a wavelength of 700 nm; (b) At a wavelength of 1100 nm. Lines are guides to the eye. The figure is taken directly from Ref. [119].

higher than 99% accuracy within a training duration of 20 minutes for concentrating dichromatic light source at 700 nm and 1100 nm. Then, we reconstructed SpliCons using the model to concentrate dichromatic light source. The SpliCons obtained with the DOENet demonstrate similarities ranging between 99.9% and 97.7% with ground-truth SpliCons. Corresponding SOEs at 700 nm and 1100 nm computed with the reconstructed SpliCons for alternating target positions are presented in Fig. 3.9. This figure shows that the DOENet generates the SpliCons, which show similar SOE results with the iterative optimization algorithm. We see an average 0.32% error in SOE at 700 nm (Fig. 3.9a) and an average 0.21% error in SOE value at 1100 nm (Fig.

Table 3.2: Average SOEs for the dichromatic light at 700 nm and 1100 nm are calculated for the территории SpliCons obtained by the iterative optimization, the DOENet, and hybrid algorithm. The table is taken directly from Ref. [119].

Design approach	**SOE (%) at 700 nm**	**SOE (%) at 1100 nm**	**Design duration**
Iterative optimization	35.6 ± 2.0%	31.8 ± 2.7%	52 minutes
The DOENet	35.3 ± 1.7%	31.6 ± 2.7%	2 seconds
Hybrid algorithm	39.8 ± 1.4%	35.0 ± 3.0%	52 minutes

3.9b). Moreover, with the DOENet, we could design a SpliCon yielding a mean SOE of 35.3 ± 1.2 at 700 nm and a mean SOE of 31.6 ± 2.7 at 1100 nm for the individual targets (see Table 3.2). These results highly overlap with mean SOEs received with the iterative optimization. Moreover, we could reconstruct a SpliCon using the DOENet that concentrates light on 100 times smaller solar cell areas. We managed to confine light energy on the target area of $20\,\mu\mathrm{m}$ x $20\,\mu\mathrm{m}$ with at least 31.6 times enhancement compared to the case where no SpliCon is used.

Next, we re-optimized the reconstructed SpliCons with the local search optimization algorithm to boost performance of the SpliCons in terms of SOE. As seen in Fig. 3.9 further optimization of the SpliCons results in higher SOEs for all alternating target positions. This optimization lasts 52 minutes on a PC and enhances concentrated light intensity up to 7.0% SOE at 700 nm (Fig. 3.9a) and 5.4% SOE at 1100 nm (Fig. 3.9b). We obtained an average 4.5 ± 0.9% SOE increase at 700 nm (Fig. 3.9a) and an average 3.8 ± 0.7% SOE increase at 1100 nm (see Fig. 3.9b and Table 3.2). Compared to the case without a SpliCon, we reached up to an excess 41.1% SOE. Considering the amount of energy received by the Sun, these excess increases that we achieve will lead to a significant rise in converted solar energy amount.

3.3.2.2 DOEs for Broadband Light

Later, we disperse the broadband light into two spectral regions: the visible band and the short-IR band. The thickness distribution of the DOE which shapes the incident light is shown in Fig. 3.10a. The dispersed visible band and short-IR band at two targets with sizes of 100 µm x 200 µm is shown in Fig. 3.10b. As observed here, the visible band of the light source accumulates at the left half area of the target plane, whereas the short IR band is concentrated at the right half of the target plane. The iterative optimization algorithm yields 60.0% SOE in the visible band and 62.6% SOE in the short-IR band for the targets (Fig. 3.11a, Table 3.3).

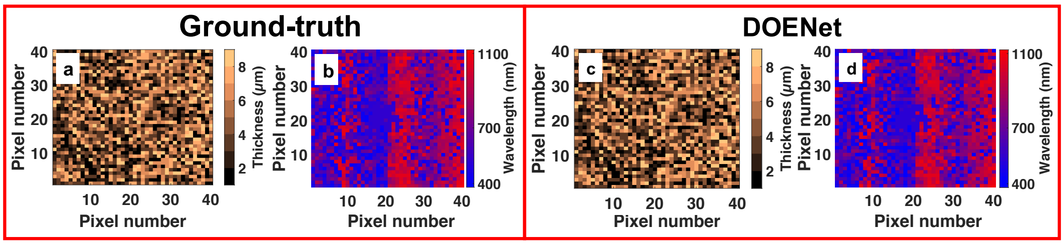

Figure 3.10: Spectral splitting of the broadband light into the visible and the short-IR bands. (a) Ground-truth thickness distribution of the DOE; (b) Wavelength distribution of the broadband light on the target; (c) Thickness distribution of the DOE obtained by the DOENet; (d) The wavelength distribution of the broadband light on the target achieved via the DOE that is designed with the DOENet architecture. The figure is taken directly from Ref. [119].

The generated data during the iterative optimization is inserted into our deep learning model, the DOENet, as a training data set. This model gives 94.8% accuracy with the training and validation data sets. Using the weights of the DOENet, we design a broadband DOE to spectrally split the broadband light, which lasts 2 seconds (Fig. 3.10c). There is a 93.7% correlation between the DOEs obtained by the iterative algorithm (ground-truth) and the DOENet. The wavelength distribution on the target with the DOE obtained by the DOENet is presented in Fig. 3.10d. As seen here, we reached a similar wavelength distribution at the target with that the iterative algorithm yields. By using the DOE designed by the DOENet, we presented the SOE spectrum of the broadband DOE in Fig. 3.11a. Here, the DOENet results indicate

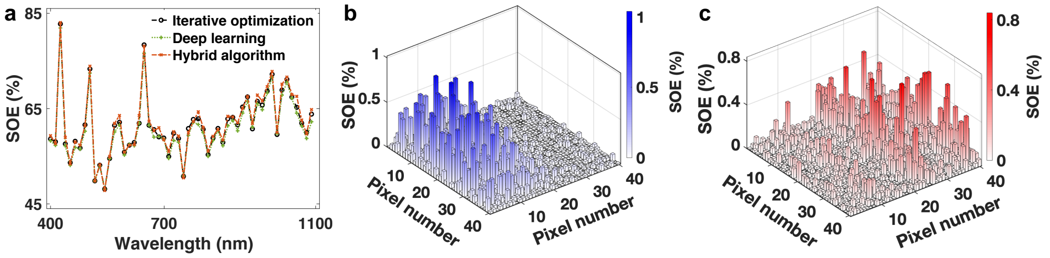

Figure 3.11: (a) The SOE spectrum for a DOE obtained with the iterative optimization, the DOENet, and the hybrid algorithm for spectral splitting the broadband light into the individual bands 400 nm - 700 nm (the visible band) and 701 nm - 1100 nm (the short-IR band). Lines are guides to the eye. The SOE distribution of the broadband light component is calculated for the DOE obtained with the hybrid algorithm, (b) at 426 nm, (c) at 985 nm. The figure is taken directly from Ref. [119].

good agreement with results attained by the iterative optimization. Quantitatively, we get a mean 59.5% SOE at the visible band and a mean 61.8% SOE at the short-IR band. Here, we see less than 1% SOE difference in the spectral splitting performance of the DOEs obtained via the iterative optimization algorithm and the DOENet. The results are summarized in Table 3.3.

We further improve the performance of the broadband DOE with the hybrid algorithm. At the end of the optimization with the hybrid algorithm, we reach a mean 60.4% SOE at the visible band and a mean 63.1% SOE at the short-IR band (Fig. 3.11a, Table 3.3). Comparing the results of our hybrid algorithm with that of the DOENet, we get 1.5% and 2.1% enhancements in performance of the DOE at the visible band and the short-IR band, respectively. In Fig. 3.11b-c, we present distributions of SOE at wavelengths of 426 nm and 985 nm, which are obtained via the hybrid algorithm. As clearly visualized in Fig. 3.11 the light source at the wavelength of 426 nm strongly generates signals on the left half area of the target plane with 83.1% cumulative SOE (Fig. 3.11b). In the meantime, the light at 985 nm strongly produces signals on the right half area of the target plane with 72.8% cumulative SOE (Fig. 3.11c).

Table 3.3: Mean SOEs for spectrally splitting the broadband light into the visible band and the short-IR band. The SOEs are calculated for the DOEs obtained by the iterative optimization, the DOENet, and the hybrid algorithm. The table is taken directly from Ref. [119].

Design approach	**SOE (%) at visible**	**SOE (%) at short-IR**	**Design duration**
Iterative optimization	60.0%	62.6%	1 day
The DOENet	59.5%	61.8%	2 seconds
Hybrid algorithm	60.4%	63.1%	1 day

3.3.2.3 SpliCons for Broadband Light Source

We first perform an iterative optimization to generate a broadband SpliCon using the local search algorithm to simultaneously spectrally split and spatially concentrate the broadband light on a small area at the target with dimensions 50 μm x 100 μm for each band. The SOE spectrum for the SpliCon is presented in Fig. 3.12. The optimized SpliCon results in a mean 19.3% SOE for the visible band and a mean 20.4% SOE for the short-IR band (Table 3.4). Compared to the lack of the SpliCon, we reach a 6.8% excess SOE for the visible band and a 7.9% excess SOE for the short-IR band with one-day SpliCon optimization. Using the data set acquired during the optimization of the broadband SpliCon, we tune weights of the DOENet to speed up the design process of a broadband SpliCon. This model gives 86.3% accuracies with the training and validation data sets. Later, we reconstructed a broadband SpliCon using weights of the model to spectrally split and spatially concentrate the broadband light. There is a 70.7% correlation in the SpliCons obtained by the iterative optimization and the DOENet. The SOE values at the design wavelengths of the SpliCon received via the DOENet are presented in Fig. 3.12. This figure shows a high correlation between light intensity at the target obtained by the iterative optimization and the DOENet. Using the reconstructed SpliCon via the DOENet within a few seconds, the SpliCon performs spectral splitting and spatially concentrating the broadband light with 16.0% and 16.8% mean SOEs for the visible band and the short-IR band, respectively (Table

3.4).

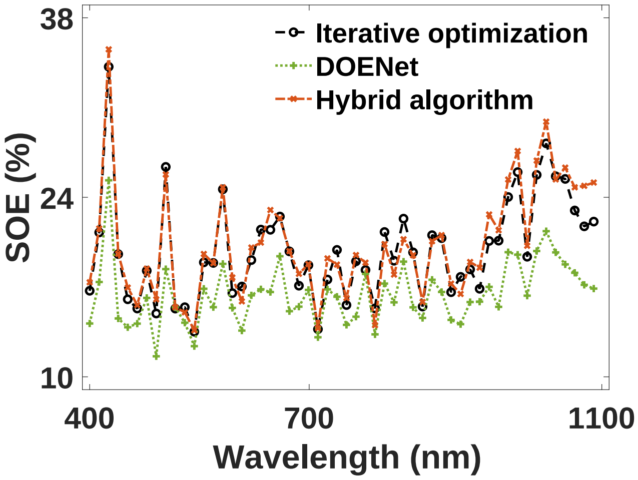

Figure 3.12: The SOE spectra for spectrally splitting and spatially concentrating the broadband light 400 nm - 1100 nm into the visible band 400 nm - 700 nm and the short-IR band 701 nm - 1100 nm on a small area of the target with dimensions $50\,\mu\mathrm{m}$ x $100\,\mu\mathrm{m}$ for each band. The SOE spectra are computed for the SpliCons, which are obtained with the iterative algorithm, the DOENet, and the hybrid algorithm. Lines are guides to the eye. The figure is taken directly from Ref. [119].

Next, we improve the performance of the SpliCon with the hybrid algorithm. Starting with the SpliCon topography obtained via the DOENet, we further optimize the SpliCon topography via the iterative search algorithm. Similar to earlier steps, our hybrid algorithm again provides improved performance. Thereby, the robustness of our hybrid algorithm is proven for different cases that are addressed in this study. As shown in Fig. 3.12 the hybrid algorithm yields higher results in the SOE spectrum while it significantly reduces the designing duration of the broadband SpliCon. The SpliCon designed via the hybrid algorithm shows a mean 19.6% SOE at the visible band and a mean 20.9% SOE at the short-IR band (Table 3.4). In terms of enhancement, the SpliCon demonstrates 57% and 67% excess light concentrations at the visible band and the short-IR band at the targets, respectively. Our hybrid algorithm increases the splitting and concentrating performance of the SpliCon by at least 22.4% compared to the DOENet based SpliCon reconstruction. With the hybrid algorithm, we design a broadband SpliCon which yields a 7.1% excess SOE at the visible band and an 8.4%

Table 3.4: Mean SOEs for spectral splitting and spatially concentrating the broadband light into the visible band and the short-IR band. The SOEs are calculated for the SpliCons obtained by the iterative optimization, the DOENet, and the hybrid algorithm. The table is taken directly from Ref. [119].

Design approach	**SOE (%) at visible**	**SOE (%) at short-IR**	**Design duration**
Iterative optimization	19.3%	20.4%	1 day
The DOENet	16.0%	16.8%	2 seconds
Hybrid algorithm	19.6%	20.9%	1 day

excess SOE at the short-IR band at a target area of $50\,\mu m$ x $100\,\mu m$ for each band.

The normalized intensity distribution at the output plane clearly indicates that the visible band of the broadband light is concentrated within the blue area in Fig. 3.13a. Since different light components of the broadband light show different phase shift through the same SpliCon, incoming light is directed outside the target area. With the hybrid algorithm, we limited to spread of the intensity distribution outside the target. The blue area bears 19.6% of the visible band intensity. The intensity distribution of the short-IR band is shown in Fig. 3.13b. 20.9% of the short-IR band is located within the red rectangular area. The diffraction nature of the light causes the generation of diverse orders and leads to light spread outside of the target. Despite that, we collect the short-IR portion of the broadband light with 20.9% SOE on the area, which is eight times smaller than the total area of the output plane.

3.4 Angle insensitive control

In this study, we design computationally cost-effective DOEs to disperse the broadband light into two bands as a visible band (400 nm - 700 nm) and a short-IR band (701 nm - 1100 nm). Our DOEs are calculated by considering the variation of incident angles of solar radiation. To optimize broadband DOEs, we take a bandwidth of 26

This part is published as a conference paper, see Ref. [120].

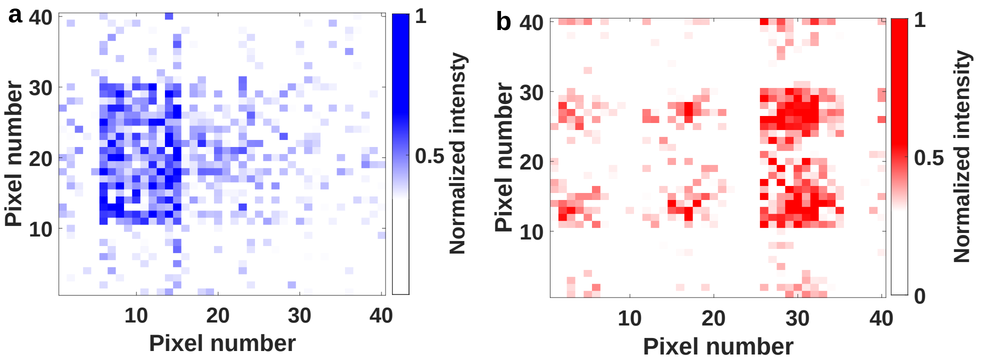

Figure 3.13: The normalized intensity distribution of the spectrally split and spatially concentrated broadband light is obtained with the SpliCon using the hybrid algorithm. (a) The intensity distribution for (a) the visible band (400 nm - 700 nm) and (b) the short-IR band (701 nm - 1100 nm). The figure is taken directly from Ref. [119].

nm into account to minimize the time of optimization. We tune the target area at the output plane where each spectral band is guided during the DOE designs. Thus, we do not increase optimization variables for different incident angles of solar radiation.

3.4.1 Problem statement

Like most other diffractive optical devices, the DOEs are designed to operate optimally at one wavelength [16, 121]. A change in wavelength modifies the diffraction pattern at the output plane; in this way, spectral optical efficiency (SOE), being fractional optical intensity at the target of the output plane, is affected. Consequently, these diffractive structures are aimed only for applications with monochromatic light sources. Operation of the DOEs under multi-wavelength is necessary for the concentration and spectrally splitting of solar radiation. In the research literature, calculated DOEs with a few hundred nanometers thickness show dispersion of the broadband light into its components [45]. In practice, the pixel thickness of DOEs cannot be adjusted with impractical precision. With the fabrication capabilities available to produce such diffractive structures, multilevel structures become more realistic, in which all of the pixel thicknesses in the design are selected from a small number of discrete thickness levels with a constant spacing (1 μm in our study as considering limit of direct laser writing [156]).

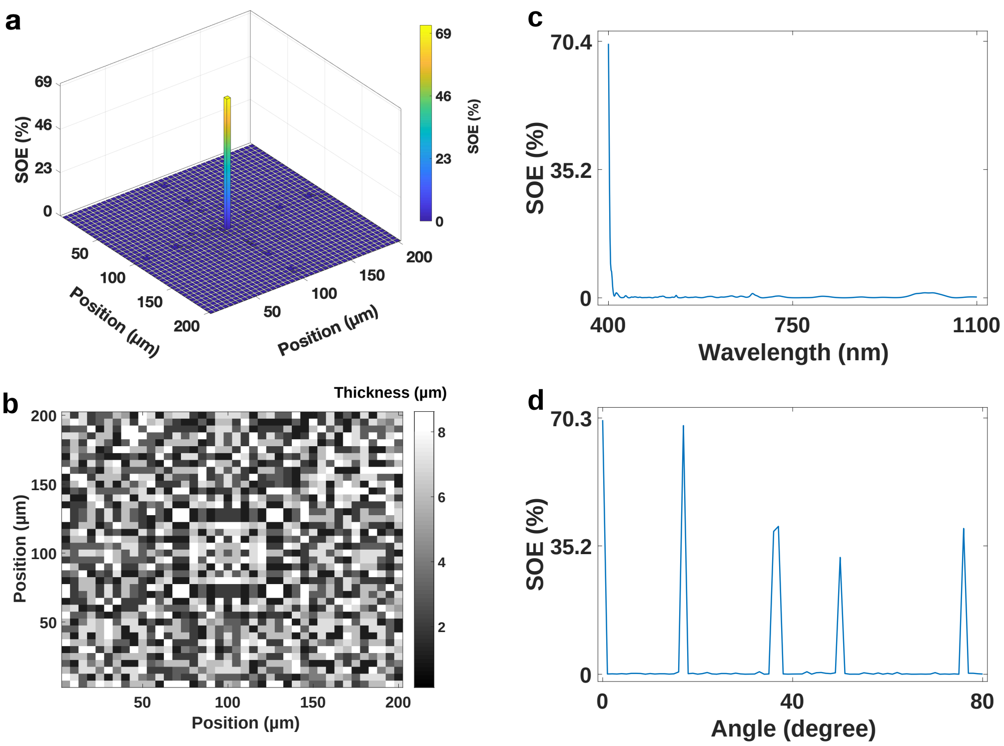

Figure 3.14: (a) The distribution of SOE at a wavelength of 400 nm and 0 degrees incident angle at the output plane; (b) Distribution of thickness value of the DOE for generating optical intensity in (a); (c) Wavelength-dependent SOE for the DOE presented in (b); (d) Variation of SOE at wavelength of 400 nm at the single target pixel of the output plan along with different incident angle of illumination (the DOE in (b) is used). The figure is taken directly from Ref. [120].

Once the waveband of the designed DOEs becomes wider, the SOE of DOEs dramatically decreases. Therefore, the SOE at a single wavelength cannot denote the broadband performance of DOEs, and the high SOE requirements cannot be satisfied. Furthermore, the SOE of DOEs drops with the variation of incident angle [40]. To verify these issues, we perform a preliminary work in which we aim to focus a light source at 400 nm at one pixel of the output plane as seen in Fig 3.14a. The resulted DOE is presented in Fig 3.14b. When the wavelength of the light source shifts to longer wavelengths, the same DOE cannot concentrate the input intensity and yield lower SOEs as seen in Fig 3.14c. Also, when the incident angle of the light source at 400 nm deviates from 0 degrees to 80 degrees, the SOE at the target pixel decreases with incident angles as shown in Fig 3.14d. With this work, we notice that all incident angles and operation wavelengths of the broadband DOEs must be considered in calculating the DOEs. However, the number of design parameters causes increased computational time of the DOEs. Our study has 701 design wavelengths with a 1 nm wavelength step within the band of 400 nm - 1100 nm. Therefore, the calculation of the broadband DOEs with this number of design wavelengths lasts 89 days. Instead of designing the broadband DOE with this huge computational expense, we apply for the bandwidth approach discovered in our previous study [121]. In this way, the computation time of the broadband DOEs is reduced to 4 days with this approach. Moreover, as an alternative to considering the number of incident angles, we tune fractional output area, which is a ratio of the target area to the output plane area, where the light source is directed while keeping SOE values high under the variation of incident angle of light.

3.4.2 Methods

The calculation of diffraction patterns is performed by the angular spectrum method of propagation. Based on Fourier optics and the scalar diffraction theory, we search for DOEs by using the local search optimization algorithm empowered by *MEAN* logic operation (detail is presented below). In our calculation, we do not consider material absorption, reflection within the DOEs, and scattering of the incident light. Also, we do not take polarization of light sources into account because the spectral splitting performance of DOEs is weakly affected by the polarization direction of light sources [54]. In addition, polarization directions of light sources do not contribute to the spectral splitting performance of DOEs more than 0.1%. Thus, here the illumination of DOEs is taken to be normally incident plane wave which covers the wavelengths of the light source (400 nm - 1100 nm) with 1 nm in wavelength resolution. The output electric field of the light after the incident light diffracted by the DOEs is computed by using the discrete summation expression of the Fresnel-Kirchhoff diffraction integral presented in Eq. 3.2. In our calculations, we take the distance d in Eq. 3.4 as $350\,\mu\mathrm{m}$ to keep diffraction patterns within the Fraunhofer regime.

The local search optimization algorithm operates as follows: it generates a random

DOE thickness profile considering the size of the DOE (here $200\,\mu\mathrm{m}$-by-$200\,\mu\mathrm{m}$ and consisting of 1600 pixels with a pixel size of $5\,\mu\mathrm{m}$). The thickness of the DOE varies spatially, and each pixel has an integer multiple of $1\,\mu\mathrm{m}$ thickness ranging between $1\,\mu\mathrm{m}$ and $8\,\mu\mathrm{m}$. Next, the algorithm calculates SOEs at design wavelengths decided with the bandwidth of 26 nm and obtains mean SOEs at two bands. Later the algorithm changes the thickness value of only the first pixel of the DOE from $1\,\mu\mathrm{m}$ to $8\,\mu\mathrm{m}$ with $1\,\mu\mathrm{m}$ step thickness. Then, the algorithm again performs the calculation of mean SOEs at two bands for each change in the first pixel of the DOE. The thickness value which yields the highest mean SOEs for both bands is accepted for the first pixel of the DOE. This is the decision-making part of our algorithm, and the logic operation is called *MEAN* (see our previous work [8]). We name calculation of SOEs for different thicknesses of each DOE pixel sub-iteration, and sub-iteration is repeated for the rest of the DOE pixels. The calculation of 1600 sub-iterations is called iteration, and we conduct eight iterations here. The calculations of DOEs are performed at various fractional output areas (target areas), and fractional output area changes between 1/8 and 1/2 (size of target area between $0.005\,\mathrm{mm}^2$ and $0.02\,\mathrm{mm}^2$) in this study.

3.4.3 Results and Discussion

In Fig. 3.15, the result of one of the target areas ($0.005\,\mathrm{mm}^2$; 1/8 in terms of fractional output area) is presented. Fig. 3.15a shows the SOE distribution at the visible band over the output plane, and the concentration of the visible band reveals at the left corner of the output plane. As a result, 24.9% SOE and 58.7% SOE at the visible band focus at the target area and the right half area of the output plane, respectively, seen in Fig. 3.15a. The short-IR band is directed to the right corner of the output plane, and almost 24.6% SOE of the incident light at this band is concentrated on the same target area ($0.005\,\mathrm{mm}^2$) as shown in Fig. 3.15b. At the right half area of the output plane, the SOE at the short-IR band becomes 60.5%.

When the DOEs are computed with the logic operation *MEAN*, mean SOEs at both bands (the visible band and the short-IR band) increase at each iteration as shown in Fig. 3.16 (this result is with the fractional output area of 1/2). Rearrangement of DOE thickness profile is continued for eight iterations, and this calculation takes four

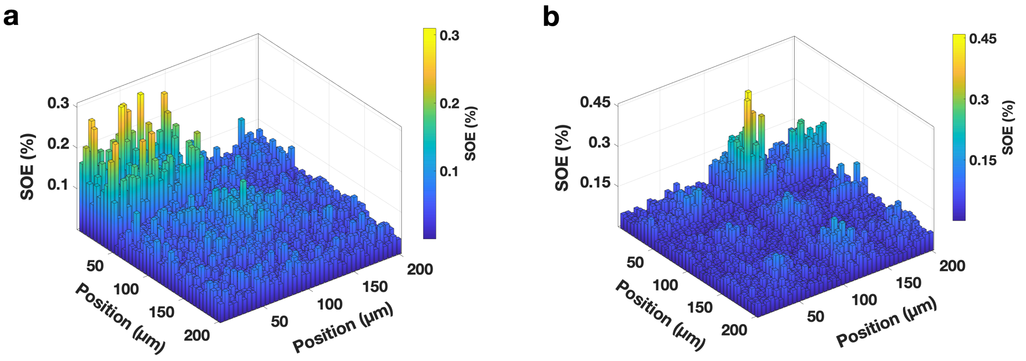

Figure 3.15: Distribution of SOE at the output plane (a) for visible band, (b) for short-IR band. In the figures, the x and y axes are position at the output plane, and the z-axis is for the SOE value. The fraction output area is 1/8 ($0.005\,\mathrm{mm}^2$ in terms of target area). The figure is taken directly from Ref. [120].

days. After eight iterations, mean SOEs become 66.3% at the visible band and 65.7% at the short-IR band, respectively, and these results do not reach saturation. Thus, the performance of the DOE will improve at both bands whether the optimization proceeds beyond eight iterations.

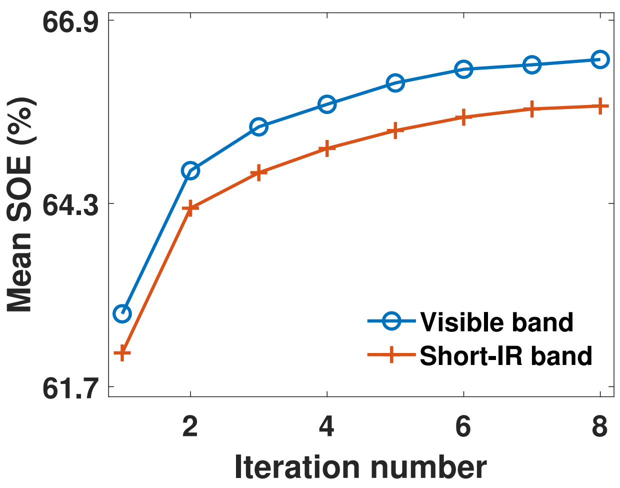

Figure 3.16: Evolution of mean SOEs at each band through 8 iterations. The blue line is for the visible band, and the red line is for the short-IR band. The fraction output area is 1/2 ($0.02\,\mathrm{mm}^2$ in terms of target area). The lines are a guide to the eye. The figure is taken directly from Ref. [120].

In Fig. 3.17a SOEs at design wavelengths after eight iterations are presented. Once the output plane area is divided into two equal units for two light bands, SOEs without a DOE become 50% at all optimization wavelengths as expected. With the optimized DOE, SOEs at many of the design wavelengths are more than 65%. This result shows that with the DOE, much more optical intensity at each wavelength is concentrated at the output plane area of $0.02\,\mathrm{mm}^2$. After the DOE was optimized, SOEs at wavelengths of the broadband light with a 1 nm wavelength step are computed within a few minutes. The SOE spectrum is presented in 3.17b. With a finer wavelength step, mean SOE reduces to 55.4% for the visible band and 60.9% for the short-IR band. 11% and 5% decreases in mean SOE are seen for the visible and short-IR bands, respectively. However, these results are superior to those without the DOEs, and an excess 5.4% and 10.9% SOEs are obtained for the visible band and the short-IR band, respectively. Moreover, these results are open to enhancing with the bandwidth value of 13 nm [8].

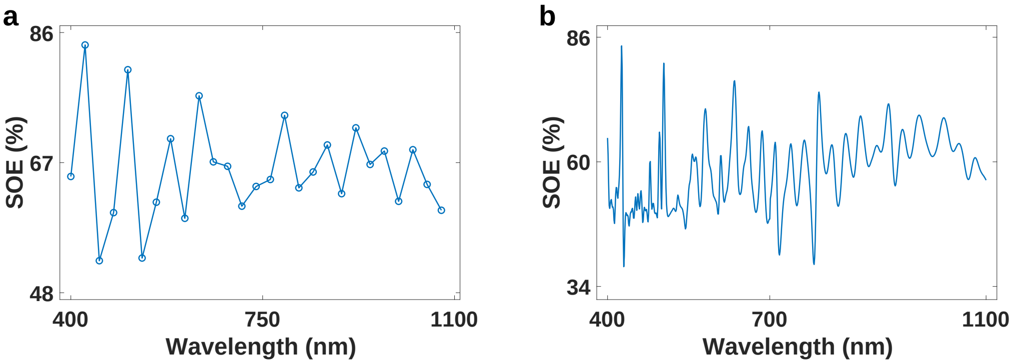

Figure 3.17: SOE spectrum at (a) design wavelengths, (b) all wavelengths of the broadband light with a 1 nm wavelength step. Fractional output area is 1/2 (target area is $0.02\,\mathrm{mm}^2$). The lines are a guide to the eye. The figure is taken directly from Ref. [120].

Next, the incident angle of the light source is deviated from 0 degrees to 80 degrees with a 1-degree step, and mean SOEs considering all wavelengths of the broadband light are computed as shown in Fig. 3.18a. Fig. 3.18a exhibits that mean SOE of the broadband light peaks 58.5% at 0 degrees and fluctuates around 57% beyond 6 degrees. The deviation in mean SOE through 80 degrees is 0.6%. Mean SOEs of two bands are depicted in Fig. 3.18b. Mean SOEs for the visible band and the short-IR band are 54% and 59.4% through 80 degrees, respectively. At the short-IR band, the DOE results in better spectral splitting as a result of higher mean SOE than that of the visible band.

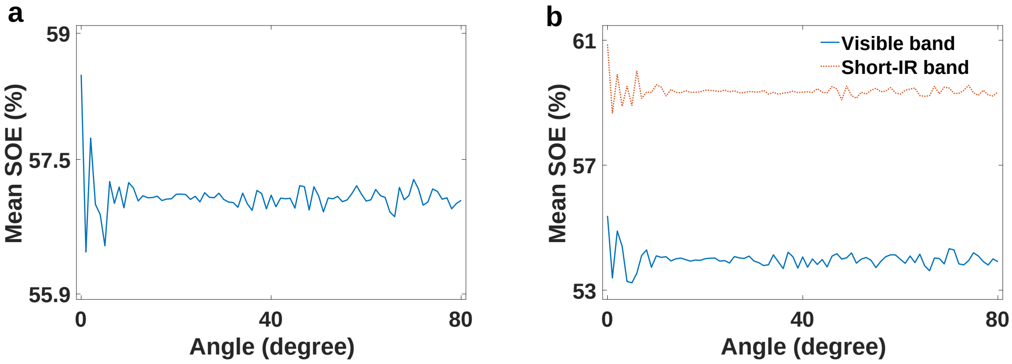

Figure 3.18: (a) Variation of mean SOE at the full band with different incident angles; (b) Variation of mean SOEs at both bands with different incident angles. Fractional output area is 1/2 (target area is $0.02\,\mathrm{mm}^2$). The figure is taken directly from Ref. [120].

Optimization of the DOEs is performed for various fractional output areas between 1/8 and 1/2 (between $0.005\,\mathrm{mm}^2$ and $0.02\,\mathrm{mm}^2$ in terms of target area). Different fractional output areas yield variation in mean SOEs of the bands (Fig. 3.19). It is easily seen in Fig. 3.19 that mean SOEs increase with a rise in fractional output areas. Among six fractional output areas, the best spectral splitting is achieved with the fractional output area of 1/2 ($0.02\,\mathrm{mm}^2$ in the target area). The mean SOEs at the visible band and the short-IR band are 54±0.3% and 59.4±0.2%, respectively. This fractional output area enables increased intensity of the solar radiation on the target as 8% for the visible band and 18% for the short-IR band compared to the case without DOEs. Further optimization of the DOEs can improve their spectral splitting efficiency. Also, reducing pixel size with keeping total size fixed can increase the efficiency by adding more degrees of freedom to the DOEs while allowing the diffracted light to bend at sharper angles.

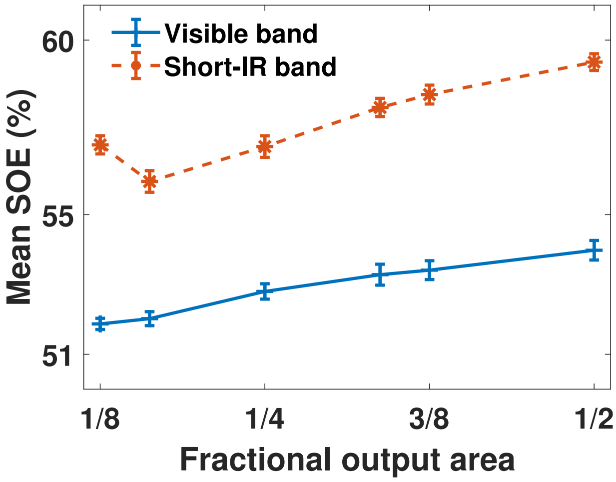

Figure 3.19: Mean SOEs at each band at different fractional output areas. The blue line is for the visible band, and the red line is for the short-IR band. Lines are a guide to the eye. The figure is taken directly from Ref. [120].

3.5 Experimental verification

This study includes the design of a reflective DOE for experimentally spectrally splitting and spatially concentrating the broadband light using a spatial light modulator (SLM), a broadband light source, and a color camera. Using the iterative search algorithm, we tune pixels of the SLM to modulate the incoherent light on the color camera. Our results show that two bands of the broadband light are effectively split and concentrated by using the local search algorithm in two hours.

3.5.1 The setup

The setup for spectral splitting and spatially concentrating the broadband light is presented in Fig. 3.20a. The broadband light source from a Tungsten-Halogen fiber-coupled light source (360 nm – 2600 nm, Optical power: 7 mW @ 535 nm, Optical power noise: 0.2%) first passes through an aspheric condenser lens (f: 16 mm). Next, a linear polarizer adjusts the polarization direction of the light so that it is aligned with the SLM modulation axis. Then the light is reflected by a mirror and incident on

---

This part is published as a journal paper, see Ref. [84].

the SLM (operating between 420 nm - 1100 nm, Holoeye Pluto-NIR-011 phase-only reflective LCOS, the frame rate of 60 Hz). The SLM is placed at a small angle to the reflected light from the mirror and acts as a pixel-wise phase controller object. The SLM that we use here is phase-only and has pixel dimensions $8\,\mu\mathrm{m}$ x $8\,\mu\mathrm{m}$ with a total 1920 x 1080 pixels. Due to the long optimization duration of a DOE to concentrate and spectrally split the broadband light, we grouped pixels of the SLM to a matrix size of 64-by-36 to reduce the number of optimized parameters. Each SLM pixel adds at max. 2.28π phase shift with a 0.23π phase step to the incident light. A DOE generated by the SLM in the setup controls the phase of the broadband light. The SLM-modulated light passes through a plano-convex lens (f=200 mm) and is collected by the CCD camera (Allied vision, Guppy Pro F-125, the spectral response of the camera chip is given in [158]). The color-CCD camera pixel dimensions are $3.75\,\mu\mathrm{m}$ x $3.75\,\mu\mathrm{m}$ with a total 1292 x 964 pixels. Our experimental setup shows 0.3% noise that includes back-reflections by the equipment, stray light, the light source noise (0.2%), the CCD camera quantification instability, and variation of experimental conditions. In our iterative optimization algorithm, we have targeted the beam of light between 420 nm - 535 nm (blue band) to the right spot and the light between 560 nm - 875 nm (red band) to the left spot at the diffraction plane. Here, we use percentage differential change (PDC) as a metric to indicate a percentage increase in intensity at the target plane. $PDC^x(\lambda)$ at a pixel position of x for color band wavelength λ is calculated via Eq. 3.6. $I_i^x(\lambda)$ and $I_f^x(\lambda)$ are the initial and final intensities at the pixel position of x and color band wavelength λ, respectively.

$$PDC^x(\lambda) = 100 * \frac{I_f^x(\lambda) - I_i^x(\lambda)}{I_i^x(\lambda)} \tag{3.6}$$

3.5.2 Results and discussion

We carried out comprehensive experiments to both concentrate and spectrally split the broadband light using a DOE with the experimental setup is seen in Fig. 3.20a. With the setup, we scan pixels of a DOE to concentrate red and blue bands of the broadband light source on two targets by using the local search algorithm. This procedure takes about 2 hours. The DOE that allows us to disperse the broadband light is presented

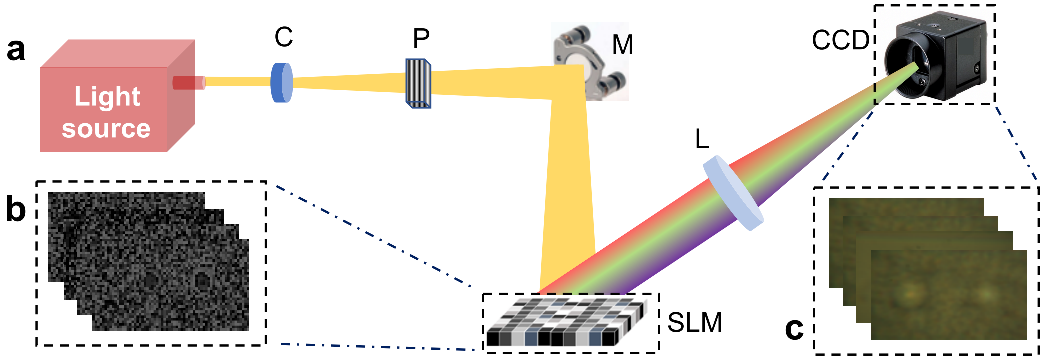

Figure 3.20: (a) The setup scheme for the spectral splitting and spatially concentrating the broadband light; C: condenser lens, P: linear polarizer, M: mirror, an SLM, L: lens with f= 200 mm, and a CCD camera; (b) The DOEs that are written on the SLM surface; (c) Intensity distributions measured via the CCD camera. The image is taken directly from Ref. [84].

in Fig. 3.21a. Using this DOE, we obtained the intensity distribution of the light source as seen in Fig. 3.21b. In Fig. 3.21b, we provide the intensity distribution of the broadband light that is split and concentrated into two separate regions. The red band is concentrated at the left of the target plane (Fig. 3.21c), and the blue band is concentrated at the right of the target plane (Fig. 3.21d). With this study, we obtained excess 63.1% enhancement in the red light band (Fig. 3.21c) and 64.1% enhancement in the blue light band (Fig. 3.21d) on the targets, respectively

Optimizing a diffractive optical element for broadband light is quite a time-consuming process. When the number of optimization parameters as the number of operating wavelength, number of pixels, etc., increase computation load is getting devastating. The calculation of a broadband DOE lasts approximately 89 days on a desktop PC, which is computationally unaffordable [8]. The number of parameters that we can control here reaches up to 2.5×10^4, and experimental optimization using the iterative method takes 2 hours in this study.

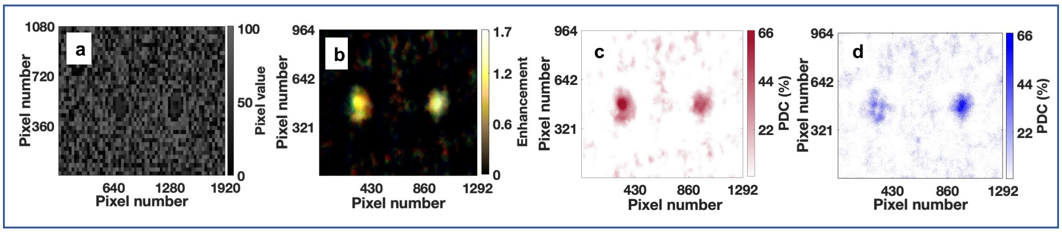

Figure 3.21: The DOE that spectrally splits and concentrates two frequency bands; (a) Iteratively optimized DOE to split the broadband light into two bands on two regions; (b) Iteratively obtained intensity distribution of the broadband light on the color CCD camera; (c-d) The intensity distributions of the broadband light for the red channel (between 560 nm - 875 nm) and blue channel (between 420 nm - 535 nm). PDC is a percentage differential increase in intensity described in Eq. 3.6. The figure is taken partially from Ref. [84].

3.6 Reconstruction of SpliCons via the SpliConNet

In this study, we develop for the first time, a neural network model to reconstruct phase patterns for spectrally splitting and spatially concentrating the broadband light and verify our designs experimentally using a spatial light modulator (SLM). In the training procedure of the neural networks, we use a set of known intensity distributions of diffraction patterns and their associated phase plates, where diffraction patterns serve as input and phase plates which structure light are given as output. The results indicate our neural network generates phase patterns for spectrally splitting and spatially concentrating light with high accuracy within a few seconds using a single graphics processing unit (GPU). Our network does not require a manual parameter search to optimize the performance of SpliCons and openly available (see our framework as well as the data set in supplementary [84]) to the community to further accelerate the transformation from uni-functional conventional structures to multi-functional diffraction optical elements.

This part is published as a journal paper, see Ref. [84].

3.6.1 Experimental data set

While optimizing the SLM for experimentally spectral splitting and spatially concentrating the broadband light, we generated a data set for developing a neural network using the setup in Fig. 3.20a. The data collection procedure is followed as: first, we start with all SLM pixels having 0 phase shift. The SLM pixels are grouped by 30 x 30, forming a superpixel, and a total 64 x 36 superpixels exist. The phase of a superpixel is scanned from 0 to 2.28π with a 0.23π phase step. In the meantime, we capture intensity distributions using the color camera. Later, we alter phase shift values of all SLM pixels sequentially and then collect intensity distributions by the color camera for each phase value of each SLM pixel. In order to perform iterative optimization, we write the phase value on the SLM that gives the highest intensity summation on red and blue target pixels. With this experimental configuration, we obtained 33796 phase plates (Fig. 3.20b) and corresponding intensity distributions (Fig. 3.20c) formed on the CCD camera. The experimental data set is collected within 1.7 hours and used for training the neural network only once. After the training neural network generation of a phase plate for an intensity distribution of interest reduces to 2 seconds via the neural network. Considering the training duration of a neural network, we reduced the pixel size of the phase plates obtained from the SLM by resulting in a 36-by-64 total number of pixels. Similarly, we reduced the size of intensity distributions to a matrix size of 36-by-64.

3.6.2 Neural network model: the SpliConNet

The neural network model the SpliConNet developed for spectrally splitting and spatially concentrating the broadband light is presented in Fig. 3.22a. Using the aforementioned data generation protocol with the experimental setup, we fine-tuned the hyper-parameters and meta-parameters of this model. This model includes 8 CNN layers with a filter size of 9-by-9 and a filter number of 32. The CNN layers in the model are the same-padded for keeping the size of feature maps invariant. After each CNN layer, an activation function of rectified linear unit (ReLU) is presented to reveal nonlinear relations between the intensity distributions and the phase plates. A ReLU activation function has an output of 0 if the input is less than 0; otherwise, the ReLU activation function gives a raw output. After the 4th CNN layer, a downsampling of the feature maps is performed with a max-pooling operation at each CNN layer. After each max-pooling operation, the number of parameters and computation load in the network are reduced. A fully connected layer with 25344 elements and a ReLU activation function are utilized after the flattening operation. Then, we reshaped generated feature maps of the intensity distributions to match the size of the phase patterns. For the classification of the phase values of the phase patterns, we used a softmax activation function. It is a more generalized logistic activation function used in the output layer of a neural network for multi-label classification. Our batch size is selected as 32 for the smooth optimization of model weights. We call the network that we develop Spectral Splitter and Concentrator Network (SpliConNet).

Using the versatile setup that we construct for training and testing SpliCons, we collect 33796 camera images for the training SpliConNet framework and use normalized intensity distributions in our model. We call Keras and Tensorflow open-source libraries, which provide tools of artificial neural networks in addition to GPU computing operation. We used the ADAM optimizer in Tensorflow to minimize categorical cross-entropy loss function over the training samples. Training of the model is completed in less than an hour using the Tensorflow library on an NVIDIA Quadro P5000 GPU. The latency of each training epoch is around 5 seconds. Once the training is completed, we test our model with validation data set, which is 10% of the input data set that is not part of the training set. The validation set prevents overfitting of the network model to the training set (Fig. 3.22b). After training, it takes only a few seconds to generate a phase plate for the desired intensity distribution.

3.6.3 Results and discussion

Our goal is to use a neural network model to determine a function of the phase values of the phase pattern, $\phi = f(I, w)$, where I is the intensity of wavefront shaped light, and f is a neural network model parametrized by a set of weights w. With the created data during the optimization of a phase plate, we trained the model in Fig. 3.22a. The model includes CNN layers to express function f in terms of weight w. Accuracies of the training and validation through epochs reach around 96.6 $\pm$ 2.3% (Fig. 3.22b).

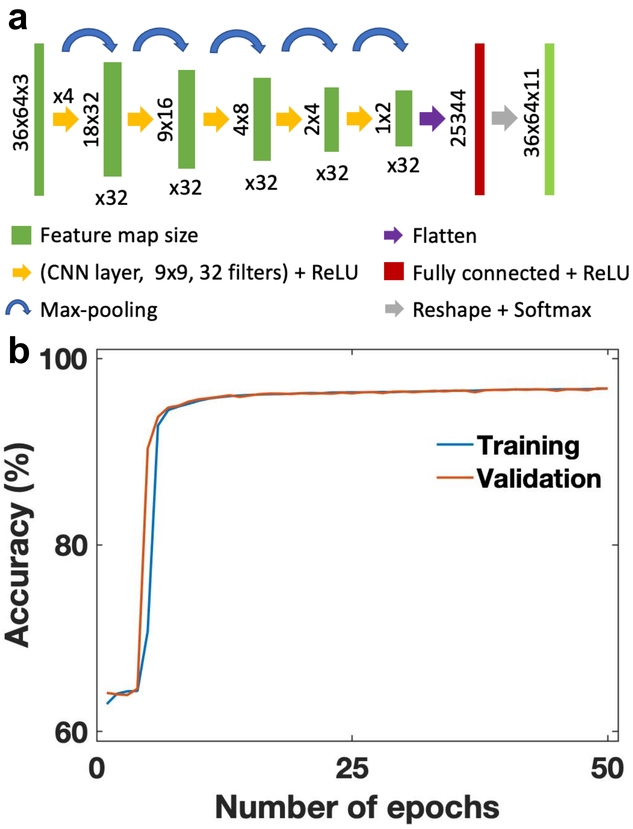

Figure 3.22: (a) Neural network model trained for experimentally spectral splitting and spatially concentrating the broadband light; (b) Training and validation accuracies of the neural network model with experimental data as a function of epochs, indicating that our model does not result in overfitting. The figure is taken directly from Ref. [84].

With the results of this figure, we concluded that the weights of the neural network model are well-optimized, and the model lacks over-fitting as we reached similar accuracies with training and validation data sets. We test the performance of our neural network for splitting and concentrating the broadband light. When we reconstruct a phase pattern for the ground-truth CCD image (Fig. 3.23b) by using weights of the neural network, we obtain a similar phase pattern (Fig. 3.23e) with the phase pattern obtained by the experimental study (Fig. 3.23a). The agreement between these phase plates reaches up to 94.9%, and this value depends on the model's accuracy, which is affected by the initialization of weights for the model. We saw 97.7 ± 2.7% mean correlation between the reconstructed phase plates for all intensity distributions in the

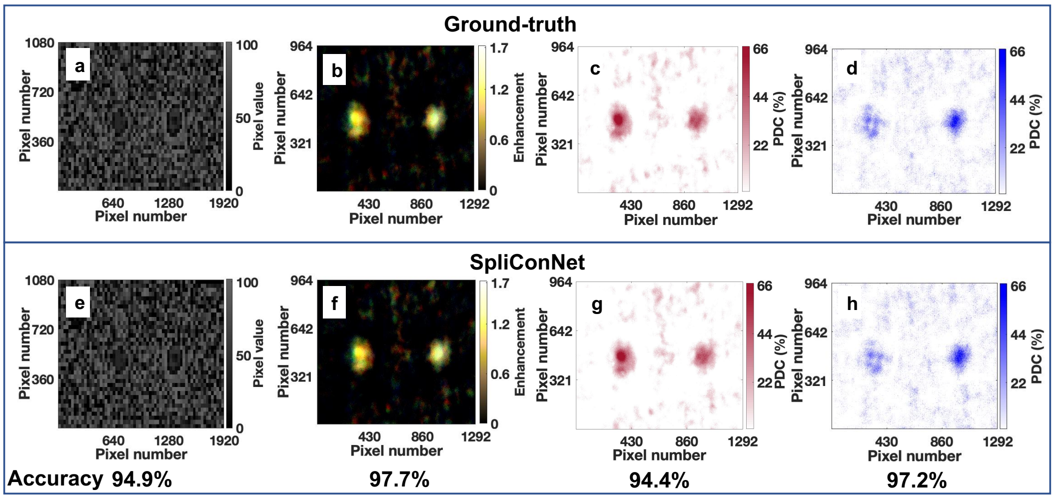

Figure 3.23: SpliCon that spectrally splits and concentrates two frequency bands; (a) Iteratively optimized phase pattern to split the broadband light into two bands on two regions; (b) Iteratively obtained intensity distribution of the broadband light on the color CCD camera; (c-d) The intensity distributions of the broadband light for the red channel (between 560 nm - 875 nm) and blue channel (between 420 nm - 535 nm); (e) SpliConNet-based phase pattern; (f) SpliConNet-based intensity distribution of the broadband light on the CCD camera; (g-h) SpliConNet-based intensity distributions of the broadband light channels. The colors of the figures indicate the color bands of the broadband light. PDC is a percentage differential increase in intensity described in Eq. 3.6. The figure is taken directly from Ref. [84].

data set and the ground-truth phase plates.

With the reconstructed phase plate, we obtained a high correlation between the ground-truth CCD image (Fig. 3.23b) and the neural network-based CCD image (Fig. 3.23f) reaching up to 97.7 ± 0.3% accuracy. The result that we obtain is limited by the setup noise of 0.3%. Therefore, the method that we develop succeeds in reaching the ground truth with unprecedented accuracy. With this neural network model, we obtained excess 62.2% enhancement in the red light band (Fig. 3.23g) and extra 61.0% enhancement in the blue light band (Fig. 3.23h) on the targets. We observe less than 4.8% error in enhancement values of the light bands with the neural network compared to the experimental results. Considering the experimental setup noise of 0.3%, the error we obtained in the CCD images is well in the expected regime.

In Fig. 3.24 we present variation of the intensities for two distinct frequency bands. Ground-truth results refer to color bands intensities of the iteratively obtained CCD image. SpliConNet in the same figure corresponds to color bands intensities of the CCD image attained via the SpliConNet developed. As can be seen in Fig. 3.24 we observe excellent agreement between the ground truth and the SpliConNet optimized intensity patterns.

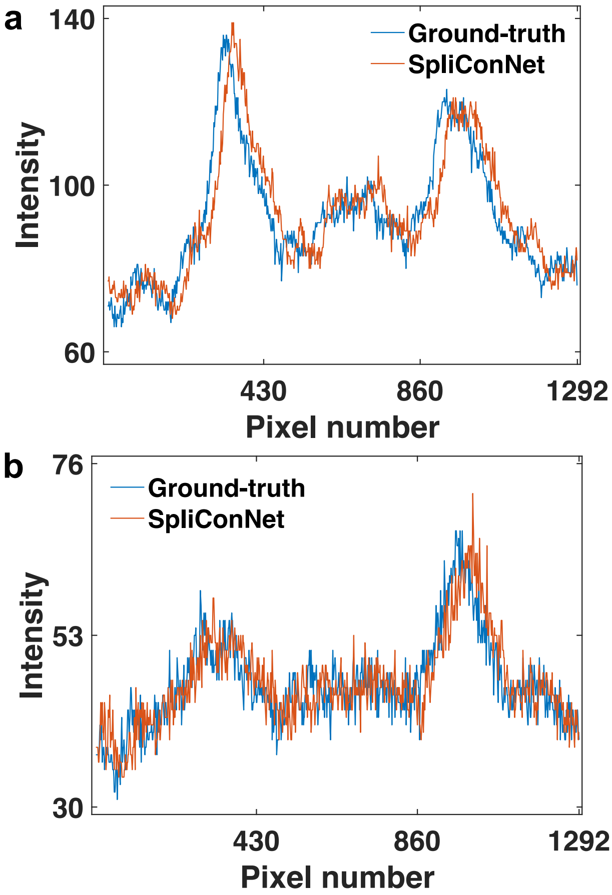

Figure 3.24: The output intensity patterns of the SpliCons for (a) red and (b) blue frequency bands that are optimized iteratively (Ground-truth) and via the SpliConNet. The cross-sectional views are obtained at y=480 pixel along where color bands are concentrated. The figure is taken directly from Ref. [84].

Our neural network models infer phase patterns from intensity distributions obtained by Fresnel-Kirchhoff integral without any need for a prior mathematical model of the diffraction within a few seconds. The current approach presented in this manuscript is embodied by using a data-driven approach, neural network architecture. Our neural network reveals hidden information between the input and the output data. Thus, spectral and spatial characteristic of broadband light does not affect the phase plate reconstruction capability of our neural network architecture. However, spatial coherence plays a crucial role in shaping the wavefront when a broadband light is used in measurements. The spatial coherence of the sunlight will provide the means to employ our method experimentally [159].

Neural networks can better understand the fundamental science and drive knowledge discovery in addition to generating useful scientific output using comprehensive data sets. Identifying the input variables that are relevant for estimating the underlying function can assist researchers in better understanding the output of the problem. However, this may not provide information about the underlying physics. We think that physics-informed neural networks can be more beneficial in understanding the underlying physics [151, 155].

With the transfer learning tool, we can significantly speed up the training procedure of our neural network model when new data set is fed from different setup schemes to reconstruct phase patterns for desired intensity distributions. Besides, we can inverse-design phase plates using our neural networks when the size of intensity distribution is up-scaled or down-scaled. Another important feature of our neural network-based spatial light concentration is to control the spot size of modulated light. Further iterative optimization of these phase plates designs yields enhanced efficiencies, and we called this a hybrid technique that constitutes the local search optimization algorithm and the neural network model to improve reconstructed phase patterns of phase plates.

3.7 Conclusion

We here put forward three logic operations for the local search optimization algorithm to design the DOEs for spectrally splitting broadband light. We demonstrate that two light sources are focused successfully to target areas using a single DOE via the *MEAN* logic operation especially. Our study aims to optimize the DOEs that are compatible with today's large-scale microfabrication methods, such as direct laser writing. By increasing the resolution in thickness of each pixel (similar to Ref(s). [54, 160, 141]) we can obtain greater SOE and enhancement values. By introducing the bandwidth approach, we designed a single broadband DOE that performs spectral splitting and concentration of broadband light. Our approach enables us to decrease computation time by 11 times while retaining the performance. Our results enable widespread usage of the DOEs in many fields, especially in solar energy and spectroscopy. The DOEs also promise to replace and outperform several optical elements such as lenses, filters, gratings, and metalenses [161]. We project that many applications that require control over broadband light can benefit from the DOEs that are now accessible using our bandwidth approach in a much shorter time.

Here, we also present an exceptional design scheme of a DOE/SpliCon with our hybrid algorithm that improves the performance of a DOE/SpliCon and greatly reduces its optimization duration. Using the deep learning architecture, the DOENet, we achieve *fast* and *efficient* design of diffractive structures that perform concentration and spectral splitting of light. The DOENet we develop here yields up to 99% accuracy in the design of a DOE/SpliCon topography. We spectrally split and spatially concentrate light using a SpliCon that provides up to a 41.1% increase in SOE efficiency with the presented hybrid approach. Thank to the hybrid approach, we reached an excess light intensity that helps in order to reduce our energy demand after harvesting much more solar energy with a DOE/SpliCon[68, 69, 46]. Our hybrid design approach may enable one to improve the spectral resolution of optical spectrometers, including a DOE/SpliCon designed for high spectral splitting within a short design duration. The presented approach is also applicable to tune structural parameters of complex photonic devices operating across a wide parameter space functionalized for various applications. We believe that using the DOENet, the design of photonic structure may be up-scaled to a higher pixel number that is required to achieve improved control on broadband light.

Moreover, we present the effect of the target area where incoming light is concentrated. Instead of including different angles of the incident light in the calculation, we modify the target area of the output plane for the normal incident of light. We show that by designing the target area of broadband light, the output of DOEs can be more angle independent. In our calculations, we observe that when each band of the light is concentrated to 1/2 of the output plane, deviation in mean SOE through 80 degrees becomes 0.6%. Also, the output intensity changes between 58.1% and 57% when the angle scans between 0 degrees and 80 degrees. As a result, 8% and 18% excess solar energy concentration can be achieved at the visible and short-IR light bands, respectively.

Besides, we presented an experimental design of DOEs using a spatial light modulator. Using an iteratively designed DOE, we concentrate more than an excess of 63.1% light on a target. Here, we also presented the design of SpliCons using a neural network model. Our model shows high accuracy in reconstructing phase patterns for spectrally splitting and spatially concentrating the broadband light. We obtained 97.7% accuracy in CCD images and 94.9% accuracy in phase plates. Using a reconstructed phase plate, we concentrate more than an excess of 61.0% light on a target. We believe that the spectral and spatial control that we achieve here will pave the way for advanced applications in holography, microscopy, and information technologies, in addition to solar energy harvesting. We openly share the fast and accurate framework that we develop in order to contribute to the design and implementation of diffractive optical elements that will lead to transformative effects in diverse fields that require spatial and spectral control of light.

CHAPTER 4

DIFFRACTIVE OPTICAL ELEMENT SPECTROMETER

4.1 Introduction

Optical spectroscopy is an important scientific field that plays roles in numerous applications such as medical diagnostics [71], chemical analysis of food constituents [72], trace amount of chemical detection [73], measurement of optical properties of pharmaceutical ingredient [74] and commonly used organic solvents [75], identification of biological materials [76, 77], and frequency-dependent absorption and transmission properties of atoms and molecules [163]. After interaction of light with materials, the optical spectrometers provide refractive indices and absorption coefficients of the materials [164]. As a type of spectrometer, atomic emission spectrometer accommodates inductively coupled plasma for spectral analysis of samples [165]. The samples exposed to the plasma radiate light, which demonstrates the spectral behavior of the samples. Other spectrometers contain a light source instead of a plasma source and yield spectral behavior of samples in reflective, transmissive, and absorptive modes. Conventional spectrometers usually include a spectral splitting element, a light detector, and a light source.

The need for portable optical spectrometers with high throughput, high spectral resolution, low weight, and low cost is of utmost importance. High spectral resolution and low detection limit from the optical spectrometers are required for trace sample/analyte detection. Performance of the spectrometers in terms of sensitivity and detection limit are strongly affected by specifications of the light source, the light detector, and the spectral splitting elements. By improving the performance of the spectral splitting

---

This chapter is filed as a patent, see Ref. [162]

elements, the optical spectrometers produce enhanced results without requiring improvement in the light sources and the detectors. Conventional spectrometers utilize diffraction gratings and prisms as spectral splitting elements to disperse the incident spectrum of the light into wavelength components. The diffraction gratings used in conventional spectrometers have a regular and repetitive structure and operate in a narrow light band determined by the groove size of the diffraction gratings. In addition, the surface of the diffraction gratings, which needs a sudden change, makes production difficult and increases production cost. Also, the prisms and diffraction gratings elevate the volume, weight, and cost of the spectrometers. Moreover, they cause the spectrometers to suffer from low photon throughput. Recent technology developments enable the construction of compact, portable, low-weight, and cheap optical spectrometers, but specifications of diffraction gratings and prisms restrict them.

Diffractive optical elements (DOEs) serve a similar purpose as diffraction gratings and prisms and show high photon throughput. Unlike the diffraction gratings, the DOEs do not have a repetitive structure and operate under a wider light band [120]. Although the DOEs look like having similar structures to the diffraction gratings, the DOEs split the light by using phenomena of interference and diffraction despite the Bragg diffraction gratings split light by employing only the diffraction phenomenon of light. Moreover, the DOEs show a 2D thickness profile, whereas the Bragg diffraction gratings have a 1D spatially varying structure. Also, the DOEs can be either transmissive or reflective, but the Bragg diffraction gratings operate only in reflective mode. Furthermore, the DOEs can steer and concentrate the light in addition to the spectral splitting of the light, so the DOEs perform the functions that a lens and a diffraction grating perform together. A high concentration of light is achieved by using the DOEs that are lighter and compact compared to conventional lenses. As mentioned in previous chapters, the DOEs have spatially thickness changes, and their structures are designed according to their functions and purposes.

The DOEs alter spatial and spectral information of light with their spatially varying thickness distributions. The DOEs create a diffraction pattern at an output plane after the incident light passes through or is reflected by them. The diffraction pattern seen at each pixel of the output plane is formed by the contribution of all incident light, which interacts with the DOEs. Considerations for designing DOEs are the path length difference between the DOEs and the output plane, wavelength components of light, pixel size of the DOEs, and refractive index of the DOE materials at light wavelengths. After determining the parameters mentioned above, the DOEs are designed by computational tools [8] or measured with experimental setups for applications of interest [84].

In this invention, we present a DOE spectrometer design performing spectral splitting a broadband light source [162]. The DOE spectrometer consists of many DOEs, each of them designed for each wavelength component of the broadband light. Then these DOEs that are located on a moving part to alter the position of the DOEs split the broadband light into desired wavelength component of the broadband light. Thanks to the moving part, the position of the DOEs providing spectral separation of the desired wavelength from the broadband light is easily adjusted. Due to a single wavelength-based design of the DOEs, the intensity of light at each wavelength of the broadband light will improve, and high throughput will be observed.

4.2 Spectrometer configuration

Here we presented the configuration of transmission DOE spectrometer with a linear moving stage as shown in Fig. 4.1. The beam from the light source passes through a series of entrance optical elements, so the light beam is adjusted for the proper operation of the DOE spectrometer. Afterward, the light beam reaches focusing and guiding elements. Then, the DOEs alter the spectral and spatial distribution of the broadband light on the photodetector. Later, the beam that passes through again focusing and guiding elements encounters the photodetector.

The incident light source in the spectrometer can be the sunlight, a laser, a light-emitting diode (LED), and a lamp. Additionally, the incident light can be reflected light from and transmitted light through a sample. The emission spectrum of incident light may bear ultraviolet, visible, and infrared regions of the electromagnetic spectrum, and the incident light can show pulsed and continuous emission. The entrance optical elements that adjust light specifications for better performance of the spectrometers may be an iris, a lens, a mirror, a telescope, a polarizer, a Glan-Thomson prism, a quarter-wave plate, and a half-wave plate. The entrance optical elements are auxiliary equipment to improve the performance of the DOE spectrometer.

The focusing and guiding elements that modulate the incident light may be a metalens, positive lens, Fresnel lens, spherical lens, cylindrical lens, dichroic mirror, concave mirror, convex mirror, fiber optic cable, and prism. The focusing and guiding elements are auxiliary equipment to improve the performance of the DOE spectrometer.

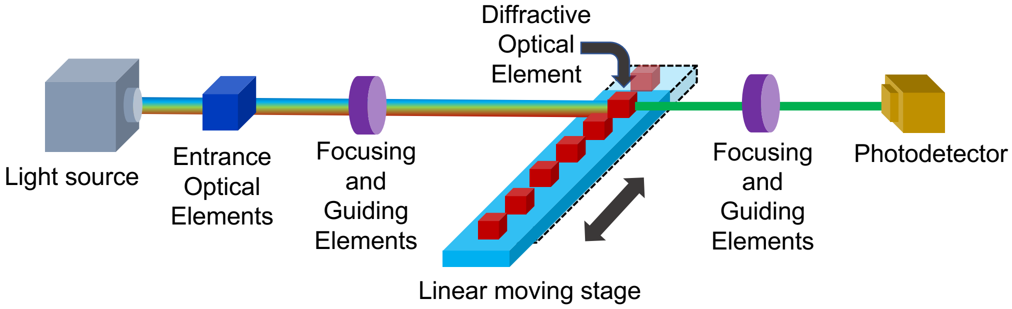

Figure 4.1: The set-up of the transmission DOE spectrometer with a linear moving stage.

As mentioned before, the DOEs can be produced with reflective or transmissive materials. The DOEs can be fabricated from metals, semiconductors, insulators, polymers, and a combination of these materials. As seen in Fig 4.1 the DOEs are located on a moving part which shows a linear motion. The linear moving part is used to change the position of the DOEs designed for each wavelength component of the broadband light. The moving part shows linear motion controlled by many mechanisms such as four-bar linkage, slider-crank, Watt linear motion, Chebyshev linear motion, Chebyshev Lambda, and Robert linear motion mechanisms. The DOEs can be reflective instead of transmissive. In that case, focusing and guiding elements and detector positions are off-axis. Instead of a linear moving stage, a rotating wheel can change the position of the DOEs located on the moving part. Rotational movement can be accessed by four-bar linkage and slider-crank mechanisms that are provided by a step motor.

The photodetector can be replaced with an avalanche photodetector (APD), photomultiplier tube, CCD camera, CMOS camera, and line array photodiodes. The spectral sensitivity of these detectors may become within ultraviolet, visible, and infrared regions of the electromagnetic spectrum.

4.3 Conclusion

In this invention, we present a DOE spectrometer design for dispersion of broadband light using the DOEs designed for each wavelength of broadband light. The position of the DOEs is altered for dispersion of the broadband light into a single wavelength using a moving part. Our DOE spectrometer will utilize almost all the incident photons owing to the high throughput of the DOEs designed for only individual wavelength. Thus, the DOE spectrometer will yield better performance compared to the diffraction gratings and prisms. Moreover, the DOE spectrometer is not restricted by narrowband operation and performs broadband spectral splitting of the light. Besides, the DOE spectrometer will provide spatially concentrating light in addition to spectral splitting and eliminate the necessity of any focusing elements. Our DOE spectrometer requires small volume and low cost while yielding high spectral resolution and throughput. This DOE spectrometer design primarily provides detection of a trace amount of chemical and biological samples. With this invention we have developed here, it is possible to turn mobile phones and computers into optical spectrometers, so toxic, explosive, and flammable chemicals can be detected everywhere with these compact optical spectrometers.

CHAPTER 5

3D COLOR HOLOGRAPHY

5.1 Introduction

Optical holography is a superior tool to retrieve phase and amplitude of light from an intensity image, which bears detailed information of the object as size, shape, and refractive index. Reconstructed object/hologram from an intensity image has important roles in high-security encryption [80, 167], microscopy [81], data storage [82], 3D object recognition [83], and planar solar concentrator [8, 23, 84]. Besides the information gained from intensity images is reversible, and the phase and amplitude information can be used to generate intensity images for numerous applications such as imaging [18, 96, 168], photostimulation [86], printing [87], optical beam steering [27], aberration correction [88], display [89, 90], and augmented reality [91]. Optical holography enables image formation at different observation planes or through a sample without requiring any focusing elements or mechanical scanning. For generation of a holographic image, fine-tuned phase/amplitude distribution of a hologram is required that increases the design duration of a hologram. Considering the wide-area implementation of optical holography for retrieving object/hologram information and generating a holographic image, a versatile methodology with a short design/optimization duration is highly demanded.

For generation of optical holographic images and object/hologram recovery, there are a variety of algorithms frequently used [169, 170, 171, 172, 173, 36]. These algorithms are easy to employ and yield good performance but require iterative optimization. Unfortunately, these algorithms lack full flexibility in design parameters, espe-

---

This chapter is published as a journal paper, see Ref. [166]

cially when the number of design wavelengths and the number of observation planes are more than one. Furthermore, a strong push to convergence for tolerable error may cause the algorithms to yield physically infeasible patterns. In contrast to these algorithms, deep learning correlates an intensity distribution to a hologram without reconstruction of phase and amplitude information from an intensity distribution thanks to its data-driven approach. Deep learning is a superior tool that presents important achievement especially in holography for imaging [174, 175, 176, 177, 93, 178, 179], microscopy [180, 181, 182, 183], optical trapping [184], and molecular diagnostics [185]. However, for the generation of optical holograms, which provide holographic images at different observation planes and wavelengths, versatile neural networks are required [186, 187, 188]. This issue is weakly addressed in the literature, and proper modalities are demanded for the generation of optical holographic images with diverse properties: different observation planes, wavelengths, and figures. Using a comprehensive neural network model, the design of holograms could be accelerated, leading to the generation of optical holographic images at different observation planes and wavelengths.

In this study, we present a method to compute color holographic images at multiple observation planes without cross-talk in detail. Later we share, for the first time to our knowledge, a single deep learning architecture that generates (i) multi-color images at a single observation plane, (ii) single color three images at multiple observation planes, (iii) multi-color images at multiple observation planes. In addition to the generation of holographic images, the deep learning model provides retrieval of object/hologram information from an intensity image without requiring phase and amplitude information of an intensity holographic image thanks to statistically retrieval behavior of deep learning. Moreover, we obtain holographic images with twin-image free by eliminating phase and amplitude retrieval. Training the deep learning model with a data set which is a one-time process lasting less than an hour, speeds up the generation of holographic images and object/hologram recovery from an intensity image down to two seconds.

5.2 Methods

5.2.1 Data set generation

A computer-generated hologram (CGH) could be a phase mask or a three-dimensional object where thickness value changes spatially. The thickness distribution of a CGH is also interpreted in a phase distribution with a refractive index value of a holographic plate and wavelength of light. With Fresnel-Kirchhoff diffraction integral (FKDI), intensity distribution of a holographic image at each light source wavelength is computed by considering the thickness distribution of a CGH. An electric field of light propagates from a hologram plane to a holographic image plane is calculated with Eqs. 5.1 - 5.3. The electric field of light at the hologram plane $U_{Hologram}$ is obtained with an incident amplitude of light $A_{incident}$, thickness distribution of the hologram $t_{Hologram}$, refractive index of the hologram material n, and wavelength of light source λ after utilizing Eq. 5.1. p and q in Eq. 5.1 are indices of spatially varying amplitude of light at the hologram plane. The light wave from the hologram plane transforms into the image plane with a kernel transformation function G in Eq. 5.2. The kernel transformation function has light propagation parameters as an observation plane distance from the hologram plane to the image plane d, location of pixels at the hologram plane (x, y) and the image plane (X, Y). a and b are indices at the image plane. Later, we obtain amplitude of light at the image plane U_{Image} with Eq. 5.3. The intensity of the holographic image I_{Image} is attained with a square of the light amplitude at the image plane U_{Image}.

We use correlation coefficient ρ as a metric to evaluate similarity between a ground-truth/ideal holographic image I_{Ideal} and a designed holographic image $I_{Designed}$ with the deep learning model/FKDI (see Eq. 5.4). The same metric evaluates similarity between a ground-truth hologram I_{Ideal} and a reconstructed hologram with the deep learning model $I_{Designed}$. N in Eq. 5.4 is number of pixels in the ideal image and the designed image; $I_{Ideal,i}$ and $I_{Designed,i}$ in Eq. 5.4 are intensity values of ith pixel of the ideal image and the designed image, respectively. The other terms in Eq. 5.4 are mean of the ideal image $\mu_{I_{Ideal}}$, mean of the designed image $\mu_{I_{Designed}}$, standard deviation of the ideal image $\sigma_{I_{Ideal}}$, and standard deviation of the designed image $\sigma_{I_{Designed}}$. We compute a correlation coefficient for a ground-truth/ideal holographic image I_{Ideal} and corresponding designed holographic image $I_{Designed}$ at each observation plane distance d and each wavelength of light λ.

$$U_{Hologram}(p,q,\lambda) = A_{incident}(p,q,\lambda) * \text{exp}(2\pi j * t_{Hologram}(p,q) * [n(\lambda)-1]/\lambda), \tag{5.1}$$

$$G(p,q,a,b,\lambda,d) = \left(\frac{1}{j\lambda d}\right) * \text{exp}\left(\frac{j2\pi d}{\lambda}\right) * \text{exp}\left[j\pi\frac{\{(y_{pq}-Y_{ab})^2+(x_{pq}-X_{ab})^2\}}{\lambda d}\right], \tag{5.2}$$

$$U_{Image}(a,b,\lambda,d) = \sum_{pq} U_{Hologram}(p,q,\lambda) * G(p,q,a,b,\lambda,d), \tag{5.3}$$

$$\rho(I_{Ideal}, I_{Designed}) = \frac{100}{N-1}\sum_{i=1}^{N}\frac{(I_{Ideal,i}-\mu_{I_{Ideal}}) * \left(I_{Designed,i}-\mu_{I_{Designed}}\right)}{\sigma_{I_{Ideal}} * \sigma_{I_{Designed}}}. \tag{5.4}$$

Using spatially varying 8-level thickness profile of a hologram, we tune phase of a light source to form a holographic image. The holographic image is designed with a linearly polarized continuous light at normal incidence. Resolutions of a hologram and a holographic image are 40-by-40. Each pixel of a hologram has a thickness value ranging from 1 μm to 8 μm, which is divided into 8 equal discrete steps. Here, we especially chose parameters that are experimentally achievable using large-area fabrication methods [156]. We evaluate performance of a hologram with a correlation coefficient ρ in terms of percent with Eq. 4 during organizing thickness distribution of the hologram with the local search optimization algorithm. The local search optimization algorithm sequentially changes thickness of each pixel in the hologram after generating a random hologram distribution to form desired intensity images at selected frequencies of the light and observation plane distances. We used two decision-making criteria: AND and MEAN, which are also called logic operations, in the algorithm to minimize difference between an ideal image (uniform and binary image distribution) I_{Ideal} and a designed image $I_{Designed}$. With AND logic operation, we organize a hologram thickness distribution considering increases in values of the correlation coefficient at each wavelength and each observation plane simultaneously. With MEAN logic operation, the hologram thickness distribution is tuned when average correlation coefficient computed with correlation coefficients at all wavelengths and all observation plane increases. At the end of designing a hologram, we obtained 51200 optical hologram distributions and corresponding holographic images at each light frequency/observation plane.

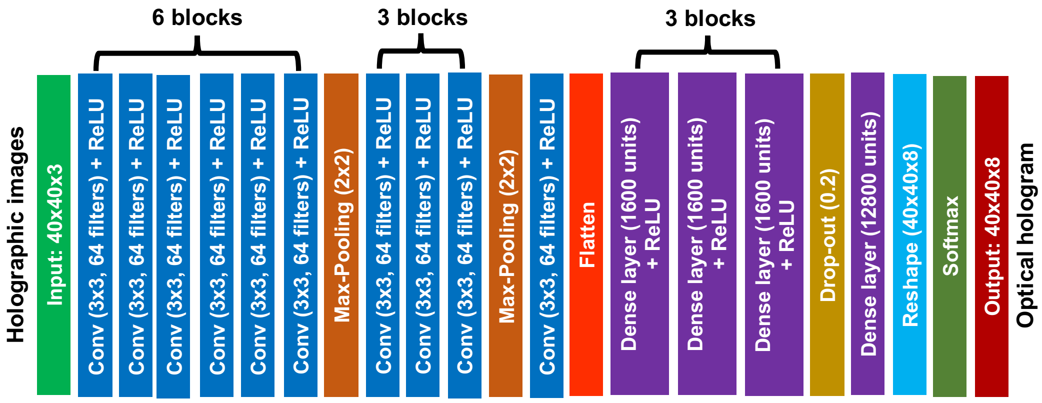

Figure 5.1: The CHoloNet architecture. Each color represents a different data operation. The model takes holographic images with a size of 40-by-40-by-3, performs feature extractions through several CNN layers, and correlates holographic images to holograms with a size of 40-by-40-by-8 by using detected features. The figure is taken directly from Ref. [166].

5.2.2 Deep learning model: the CHoloNet

In this manuscript, we employed the deep learning model the CHoloNet presented in our previous work [119] (see Fig 5.1). The CHoloNet demonstrates reconstruction of an object thickness distribution/hologram by using holographic intensity images at all wavelengths of light and observation planes. The framework uses holographic intensity images to train weights of the model and understands how to transform spectral and spatial information of incident light encoded within holographic images to optical holograms. The CHoloNet receives multiple images at different observation planes/colors as inputs and produces a hologram in terms of thickness that can reconstruct input images at predefined depths/colors. The model takes three-channel intensity distributions, two of which belong to the spatial size of intensity distributions, and the third is for either different wavelengths, observation planes, or wavelengths plus observation planes. The CHoloNet consists of 10 convolutional neural network (CNN) layers with 64 filters and a filter size of 3-by-3, two max-pooling layers with a size of 2-by-2, a flattening layer, three dense layers with 1600 units, one dense layer with 12800 units, a drop-out layer with a factor of 0.2, a reshaping operation, and a softmax activation function. For tuning weights of the model, we utilize 51200 holographic images at each frequency channel/observation plane and corresponding 8-bit thickness distribution of holograms as a training data set. Before tuning weights of the CHoloNet, we convert hologram information to a one-hot vector with eight classes for obtaining better performance with discrete hologram distributions. During training with 90% of all data, the CHoloNet minimizes categorical cross-entropy loss function. The CHoloNet iteratively updates the model's weights and biases using the adaptive moment estimation (Adam) optimizer with a learning rate of 10^{-4} and a batch size of 100 during back-propagation. The model is implemented using TensorFlow, an open-source deep-learning software package. The training and blind testing of the network were performed on a workstation with 32 GB RAM and an NVIDIA Quadro P5000 GPU. The training process lasts less than an hour for 50 epochs. Once the training was completed at each epoch, we test our model with a validation data set, which is 10% of the input data set. After the training, the network inference time for reconstruction of an object/hologram distribution with reversing one-hot vector operation is almost two seconds on average.

5.3 Results and discussion

The selection of design wavelengths is crucial to form holographic intensity images at the image plane without a cross-talk between images at different frequencies of light. For this concern, we first inspect spectral bandwidth, which a holographic image presents when a hologram designed for this image is illuminated by broadband light. We design a CGH that images an intensity distribution of letter A at a wavelength of 700 nm as seen in Fig. 5.2a. This image provides a correlation coefficient of 96.6% with a uniform and binary image of letter A after utilizing Eq. 5.4. As seen in this image, we generated a clear and almost uniform intensity distribution of letter A which is obtained with a hologram distribution having a thickness profile in Fig. 5.2b. When the same CGH is illuminated by a uniform broadband light (650 nm - 750 nm), the correlation coefficient varies through different illumination wavelengths of light as seen in Fig. 5.2c, and correlation coefficient peaks at the design wavelength of CGH, which is 700 nm as expected.

In Fig. 5.3, we present holographic images of letter A under different illumination wavelengths of light between 692 nm and 707 nm. As seen here beyond and before the design wavelength of the CGH (700 nm), holographic images lose clear shape of letter A, and diffraction orders appear in the images. Especially beyond the design wavelength of the CGH between 701 nm and 707 nm, diffraction orders in the holographic images are dominant. The diffraction orders can be eliminated by selecting a longer distance between the hologram plane and the image plane. In that case, the correlation coefficient at the illumination wavelength will change, and the same hologram may not form the image of letter A. These holographic images are acquired for the selected design parameters, and by considering updated design parameters, the hologram can be re-designed.

In Fig. 5.2c, we see that the correlation value is less than 10% when the illumination wavelength shifts 30 nm from the design wavelength of the CGH. With this figure, we understand that the intensity image of letter A is drastically distorted when the wavelength of light shows a 30 nm difference from the design wavelength of the optimized CGH. This wavelength shift is strongly affected by the distance between the CGH plane and the image plane, sizes of the CGH plane and the image plane, size of each pixel in the CGH plane and the image plane, and wavelength of the light source. As a result, we conclude that when the design wavelengths of a color holographic image are 30 nm apart, there is no overlap between the images. Therefore, a true multi-color hologram should work beyond 30 nm bandwidth.

At first, we tuned thickness distribution of a CGH for generation of a holographic color image at a single observation plane. The wavelengths of the color image are 670 nm for alphabet image of A, 700 nm for alphabet image of B, and 730 nm for alphabet image of C. The transmitted images from the hologram plane are projected

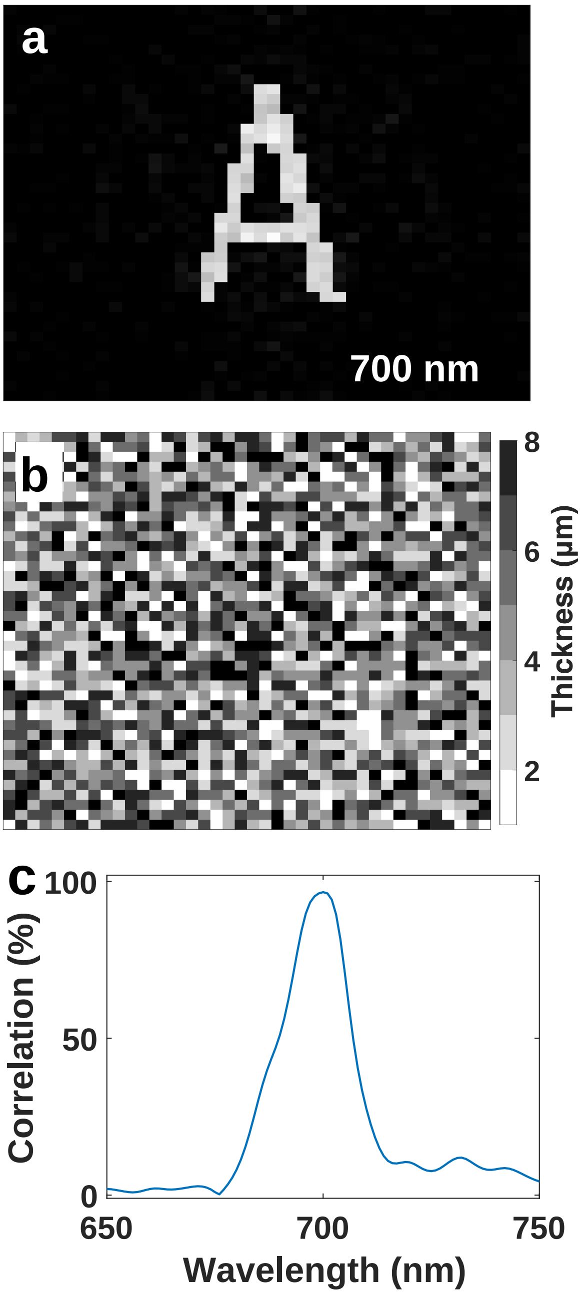

Figure 5.2: (a) The intensity image of letter A; (b) Thickness distribution of designed CGH which produces the image as seen in (a); (c) The correlation spectrum of holographic images at wavelengths between 650 nm - 750 nm obtained with the hologram presented in (b). The figure is taken directly from Ref. [166].

onto a white screen 350 μm away from the surface of the CGH. The thickness optimization of the hologram was performed for four full scannings of all the hologram pixels, which lasted 3.6 hours with the local search optimization algorithm. The holo-

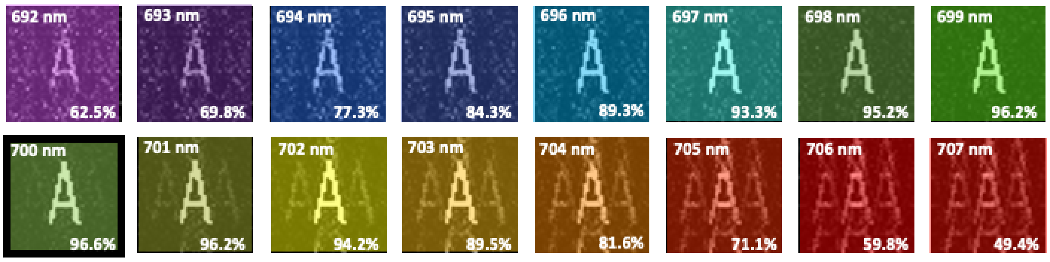

Figure 5.3: Variation of holographic images under different illumination wavelengths of light (692 nm - 707 nm) obtained with the hologram in Fig. 5.2b. The design wavelength of the holographic image A is 700 nm. The figure is taken directly from Ref. [166].

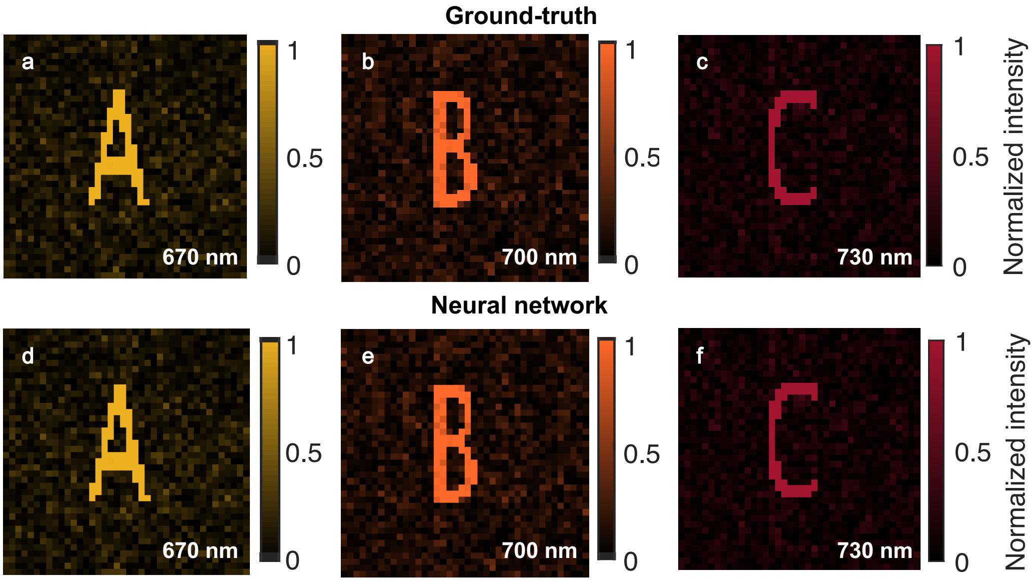

Figure 5.4: Generation of a holographic color image at a single observation plane. Ground-truth images of (a) letter A, (b) letter B, and (c) letter C. The CHoloNet based holographic images of (d) letter A, (e) letter B, and (f) letter C. The figure is taken directly from Ref. [166].

graphic images of letters are presented in Fig. 5.4a-c. The intensity values on pixels of the letter figures are higher than the background, and we observe formation of three holographic images with high contrast. For generation of these images, we use the equation of correlation coefficient in Eq. 5.4 as a cost function with MEAN logic operation. When AND logic operation is employed, the holographic images present

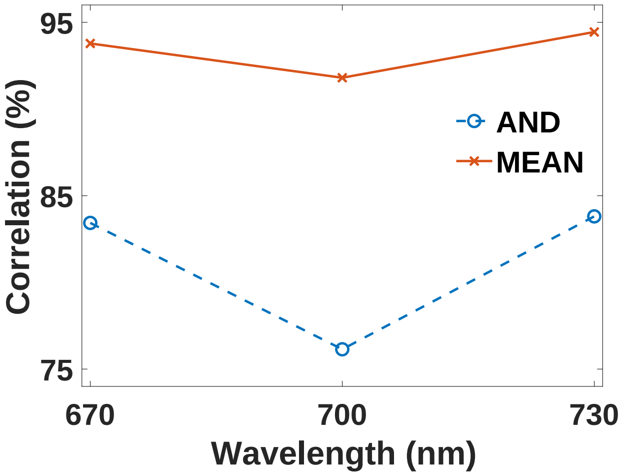

Figure 5.5: Change of correlation coefficients at design wavelengths of the holographic color image with two logic operations: AND and MEAN. The figure is taken directly from Ref. [166].

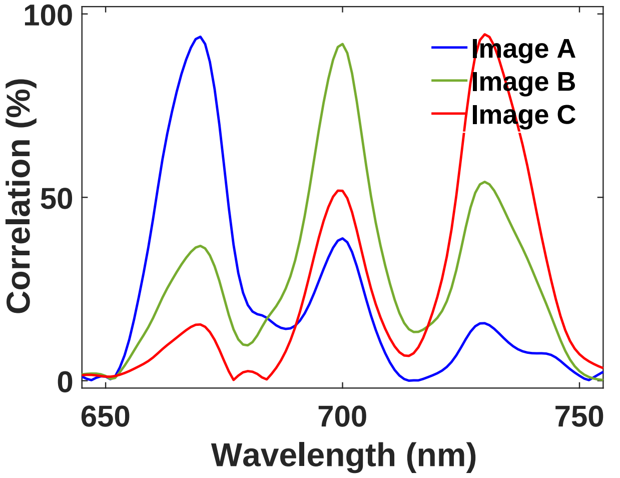

Figure 5.6: Correlation spectra of letter images A, B, and C when illumination wavelength spans between 650 nm and 750 nm. The figure is taken directly from Ref. [166].

a mean correlation of 81.1% (Fig. 5.5). With MEAN logic operation, we received a higher mean correlation value of 93.3% due to increasing mean of correlation coefficient calculated with correlation coefficients at all design wavelengths. The images of letters A, B, and C show correlation coefficients of 93.8%, 91.8%, and 94.4% in

Fig. 5.5, respectively.

When the designed hologram is illuminated by wavelength of light at 670 nm, we see low correlation coefficients of 36.8% and 15.3% between letters A and B and letters A and C at the image plane of letter A, respectively (Fig. 5.6). However, cross-talk in Fig. 5.4a is not visible even though there is a correlation of 36.8% between letters A and B, and we observe only formation of letter A without formation of letters B and C. The ideal, uniform, and binary holographic image of letter A shows correlation coefficients of 34.8% and 12.0% with letters B and C, respectively. These high values are due to the fact that a great portion of the intensity image pixels is formed with zero intensity values. Moreover, the spatial similarity of the letters leads to a correlation which is expected. Therefore, correlation coefficients of 36.8% and 15.3% between letters A and B and letters A and C are not surprising, respectively. A similar situation occurs for letters A and C when illumination wavelength of light is 700 nm. There is no sign for formation of letters A and C in Fig. 5.4b, but there are 51.8% and 38.8% correlation coefficients between letters B and A and letters B and C in Fig. 5.6, respectively. The ideal, uniform, and binary holographic image of letter B shows a correlation coefficient of 44.7% with letter C. Correlation coefficients between letters C and A and C and B are 54.2% and 15.7% in the same figure when the same hologram is illuminated with light at a wavelength of 730 nm, respectively. However, there is no sign for formation of letters A and B at the image plane of letter C in Fig. 5.4c.

While tuning the thickness profile of the hologram for holographic images of letters A, B, and C, we stored intensity images and holograms at each optimization attempt. With the collected data set, we tuned weights of the CHoloNet to reconstruct object information from an intensity color holographic image. The CHoloNet yields 99.7% accuracies with the training and the validation data sets. We reconstruct a hologram with the CHoloNet, which shows a correlation coefficient of 99.9% with the ground-truth hologram. The reconstructed hologram by the CHoloNet is high-fidelity object information obtained within two seconds. When the reconstructed hologram is illuminated with a light source at 670 nm, 700 nm, and 730 nm, we see holographic three images as presented in Fig. 5.4d-f. These three holographic letter images are obtained with the reconstructed hologram using FKDI and Eqs. 5.1 - 5.3. These holographic images present correlation coefficients of 99.9% with the ground-truth images. Using the CHoloNet, we reconstruct a hologram structure that provides a color image at a single observation plane within two seconds. This holographic structure behaves color filter to achieve a full-color holographic image with no cross-talk simultaneously. Moreover, we see twin image-free holographic intensity images due to the elimination of recovery of phase and amplitude information from the holographic intensity images.

Next, we reconstructed a hologram structure that images three different figures forming at different observation planes (Fig. 5.7). The holographic images are arranged in order from letter A (350 μm), letter B (400 μm) to letter C (450 μm), where letter A is the nearest to the hologram plane and letter C is the farthest to the hologram plane. The CHoloNet shows accuracies of 99.7% with the training and the validation data sets, and the reconstructed hologram with the CHoloNet has a correlation coefficient of 98.5% with the ground-truth hologram. Later, the reconstructed hologram is illuminated with a light source emitting at a single wavelength of 700 nm. With FKDI, we perform a numerical calculation for holographic intensity images seen at 700 nm and three observation planes. As seen in Fig. 5.7, we obtained clear and high contrast holographic images of letters formed at the same observation planes. We see the formation of letter images A, B, and C at 350 μm, 400 μm, and 450 μm, respectively. Moreover, holographic images cannot be formed out of predefined observation planes (Fig. 5.8). In this figure, we observe background correlation coefficients for images A and B and images A and C at the observation plane of image A, 350 μm away from the hologram plane. The same situation happens at the observation planes of images B and C. These three holographic images are almost the same as the ground-truth images and present correlation coefficients of 99.9% with the ground-truth images.

Lastly, the CHoloNet provides us reconstruction of a hologram that generates a color holographic image at three observation planes (Fig. 5.9). The letters A, B, and C are seen 390 μm, 370 μm, and 350 μm away from the hologram plane, respectively. Using the training data set of 51200 color images and holograms, the CHoloNet yields accuracies of 99.4% with the training and the validation data sets. The hologram designed with the CHoloNet has a correlation coefficient of 98.9% with the ground-truth hologram. When the reconstructed hologram is illuminated with a light source

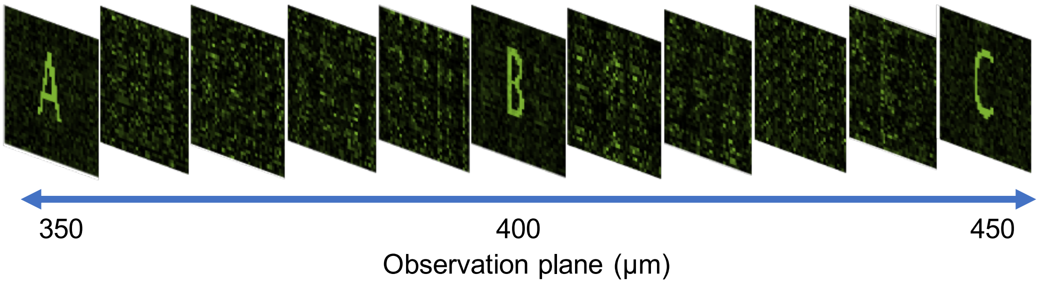

Figure 5.7: The CHoloNet based monochrome holographic images at a wavelength of 700 nm and different observation planes. The figure is taken directly from Ref. [166].

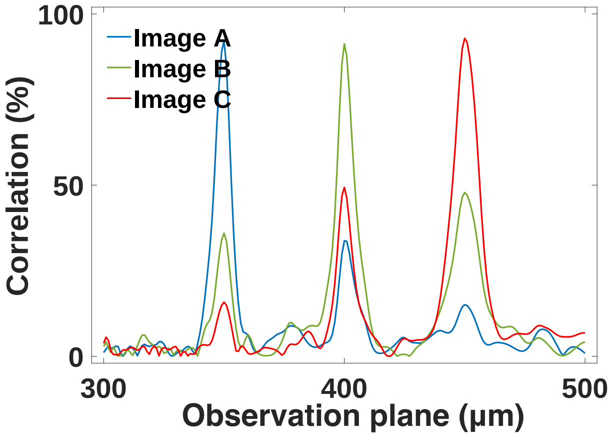

Figure 5.8: Variation of correlation coefficient for CHoloNet based monochrome holographic images with different observation planes. The figure is taken directly from Ref. [166].

emits at three wavelengths: 670 nm, 700 nm, and 730 nm, a color holographic image is seen at the aforementioned observation planes in Fig. 5.9. The letter A is formed at 390 μm away from the hologram plane at a wavelength of 670 nm due to encoded spatial and spectral information into the reconstructed hologram in the same figure. In the meantime, we see formation of letter B at a wavelength of 700 nm and an observation plane of 370 μm. The same hologram images letter C at a wavelength of 730 nm and an observation plane of 350 μm as seen in Fig. 5.9. These holographic images present high correlation coefficients of 99.9% with the ground-truth images. The formation of images is so sensitive to the design parameters, and the images are

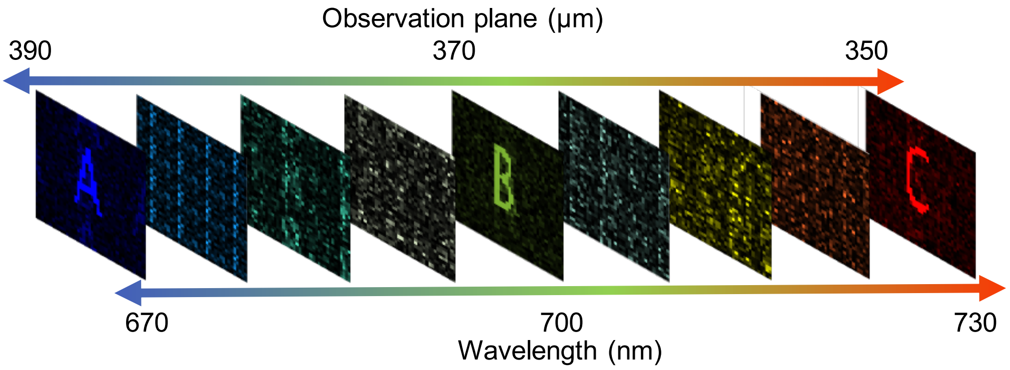

Figure 5.9: Variation of the CHoloNet based holographic images with wavelength and observation plane distance. The figure is taken directly from Ref. [166].

seen at the predefined observation planes (Fig. 5.10a). Fig. 5.10a shows that letters A, B, and C are only generated at the observation plane of 390 μm, 370 μm, and 350 μm, respectively. When the same hologram is illuminated by the broadband light source at between 630 nm and 770 nm, we observe formation of holographic images only at the predefined light wavelengths (Fig. 5.10b), and we have cross-talk free color holographic images at multiple observation planes.

The generalization ability of our model is proved with the data set used for the images in Fig. 5.4. As mentioned before, 51200 data are responsible for training our neural network. During the data set generation, different hologram structures are obtained to result in holographic images of the letters. Different holograms enable us to acquire different light intensity distributions at the image plane. Our model learns the relation between the holographic images and the holograms. Generalization of the model seems inherently possible with the model due to different intensity images within the data set. To prove our claim, we first reconstructed all the holograms that generate intensity images within the data set with our model. Then we calculate correlation values between the ground-truth and the neural network-based holograms. As seen in Fig. 5.11 our model reconstructs the holograms with correlation coefficients ranging between 95% and 100%, and we encounter a mean correlation of 99.7%. As a result, we conclude that our model reconstructs holograms for imaging letters and modulating incident light to obtain different intensity distributions at the output plane.

The deep learning model used in this study decodes three-dimensional information

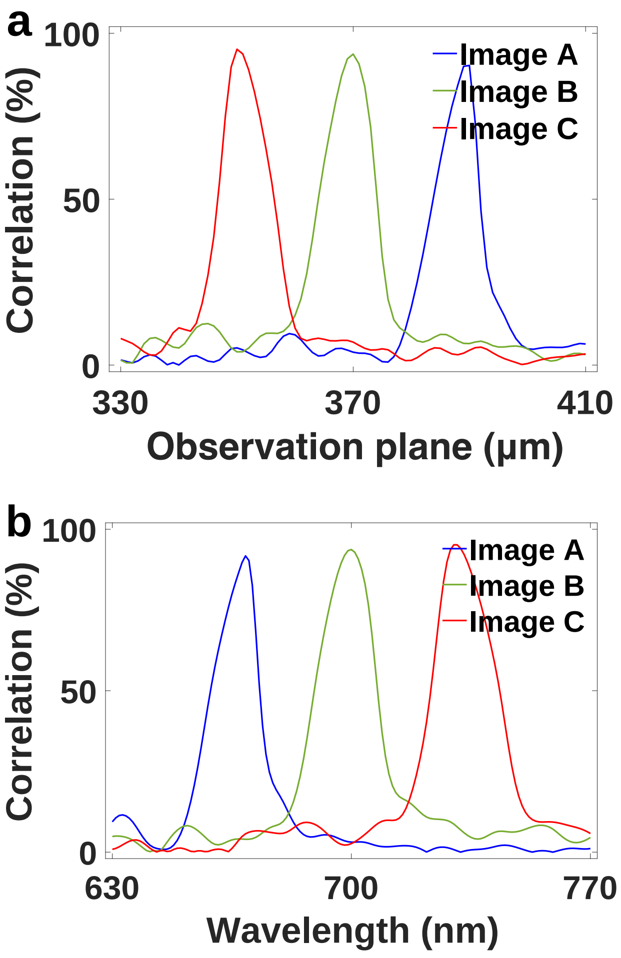

Figure 5.10: Correlation coefficient change of the CHoloNet based holographic images with (a) observation plane and (b) wavelength. The figure is taken directly from Ref. [166].

of an object from an intensity-only recording. Our results qualitatively and quantitatively with correlation coefficient demonstrate effectiveness of the CHoloNet framework for formation of holographic images having different properties as wavelength, figure, and display plane. The CHoloNet does not expand a possible solution set constrained by physics. Instead, the CHoloNet finds the best solution within the data set considering desired intensity distribution. Compared to exhaustive search algorithms, we create holograms by using the CHoloNet. The developed neural network architecture may boost design duration of a holographic image obtained by a hologram displayed on a spatial light modulator or a digital micro-mirror device. This work can be further improved to observe holographic images for multiple observers

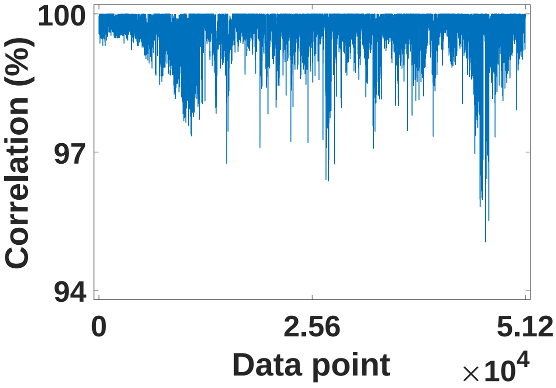

Figure 5.11: Correlation coefficients of all reconstructed holograms for the intensity images within the data set with the CHoloNet. The figure is taken directly from Ref. [166].

at oblique viewing circumference. Also, if a hologram's phase modulation capability is extended with an increasing number of thickness values in a hologram, the clarity of holographic images improves. We believe the CHoloNet can be used to retrieve imaginary (phase) and real (intensity) parts of light from an intensity-only holographic image. The model we develop may be used for hyperspectral image generation, which will increase the amount of data transfer rate. Similarly, the method can be applied to control optical microcavity arrays or quantum dot arrays that are placed at different longitudinal and lateral positions [189].

5.4 Conclusion

This work presents color holographic image generation with a 30 nm wavelength step to obtain cross-talk-free images. Using a single deep learning architecture, the CHoloNet, we demonstrate holographic image formation at different frequencies and different observation planes. The CHoloNet enables us to obtain phase-only holographic structures to generate holographic intensity images in two seconds. Moreover, thanks to the data-driven statistical retrieval behavior of deep learning, we reconstruct hologram/object information from holographic images without requiring phase and amplitude information of recorded holographic intensity images. Compared to the iterative optimization methodologies, our neural network produces holograms with several orders of magnitude faster and up to an accuracy of 99.9%. The reconstructed holograms give superior quality reproduced intensity patterns. We believe our work inspires a variety of fields as biomedical sensing, information encryption, and atomic-level imaging that benefit from frequent accommodation of optical holographic images and object/hologram recovery.

CHAPTER 6

CONCLUSION AND OUTLOOK

In this thesis, we share various methodologies and novel ideas for high efficient, fast, and high accurate control of broadband light both in spectral and spatial domains. We obtain excess light concentration/focusing and spectral splitting performance for solar energy using diffractive surfaces. Our bandwidth approach considers the bandwidth of the light spectrum around the design wavelength to tune the topography of diffractive surfaces and will speed up the design duration of them for various applications such as imaging, hologram, lens, filter, and grating generation. The neural network model, the DOENet we mention in this thesis, reconstructs the DOEs/SpliCons for desired intensity distributions. The DOENet gives high accurate the DOEs/SpliCons for modulation of the broadband light in two seconds. Moreover, the DOENet shows high performance for both narrowband and broadband light modulation. We believe that the DOENet could provide enhanced performance for incoherent broadband light modulation. Here we see that the concentration area on the target plane strongly affects the light intensity variation once the broadband light's incident angle changes. By modulating the concentration area, we diminish intensity fluctuation at the target plane for 80 degrees variation in the incident angle of the broadband light. We believe that control on the concentration area will increase converted solar energy by the solar cells. Next, we validate the performance of the SpliCons optimized with a spatial light modulator for spectrally splitting and spatially concentrating the incoherent broadband light with two hours optimization duration. Our neural network, the SpliConNet, provides to retrieve the SpliCons in two seconds that encrypts the broadband light modulation for solar energy and could be utilized for such as optical communications and quantum computing. Later, we propose the DOE spectrometer to split the broadband light into its wavelength components. The DOE spectrometer will yield high spectral resolution and enhanced throughput, which are required for many applications such as a trace amount of chemicals detection. Here we explain how holographic color images at multiple observation planes without cross-talk are generated with a computational tool. Also, we share the deep learning model the CHoloNet to obtain the holographic color images at multiple observation planes in two seconds. The CHoloNet retrieves hologram patterns for holographic images, which could be disrupted with the other algorithms. The imaging methods that we develop here can be used to spectrally resolve the emission from quantum sources at an increased resolution. We also believe that the CHoloNet could help to form images experimentally with incoherent light.

REFERENCES

[1] A. P. Mosk, A. Lagendijk, G. Lerosey, and M. Fink, “Controlling waves in space and time for imaging and focusing in complex media,” *Nature Photonics*, vol. 6, no. 5, pp. 283–292, 2012.

[2] B. Gjonaj, J. Aulbach, P. M. Johnson, A. P. Mosk, L. Kuipers, and A. Lagendijk, “Focusing and scanning microscopy with propagating surface plasmons,” *Physical Review Letters*, vol. 110, no. 26, p. 266804, 2013.

[3] G. Konstantatos and E. H. Sargent, “Nanostructured materials for photon detection,” *Nature Nanotechnology*, vol. 5, no. 6, pp. 391–400, 2010.

[4] X. Wan, Q. Zhang, T. Y. Chen, L. Zhang, W. Xu, H. Huang, C. K. Xiao, Q. Xiao, and T. J. Cui, “Multichannel direct transmissions of near-field information,” *Light: Science & Applications*, vol. 8, no. 1, p. 60, 2019.

[5] V. Mico, Z. Zalevsky, P. García-Martínez, and J. García, “Synthetic aperture superresolution with multiple off-axis holograms,” *Journal of the Optical Society of America A*, vol. 23, no. 12, p. 3162, 2006.

[6] V. Mico, Z. Zalevsky, P. García-Martínez, and J. García, “Superresolved imaging in digital holography by superposition of tilted wavefronts,” *Applied Optics*, vol. 45, no. 5, p. 822, 2006.

[7] B. K. Yildirim, E. Bor, H. Kurt, and M. Turduev, “Zones optimized multilevel diffractive lens for polarization-insensitive light focusing,” *Journal of Physics D: Applied Physics*, vol. 53, no. 49, p. 495109, 2020.

[8] A. Yolalmaz and E. Yüce, “Effective bandwidth approach for the spectral splitting of solar spectrum using diffractive optical elements,” *Optics Express*, vol. 28, no. 9, p. 12911, 2020.

[9] W. Bishara, T.-W. Su, A. F. Coskun, and A. Ozcan, “Lensfree on-chip mi-

croscopy over a wide field-of-view using pixel super-resolution," *Optics Express*, vol. 18, no. 11, p. 11181, 2010.

[10] F. Balli, M. Sultan, S. K. Lami, and J. T. Hastings, "A hybrid achromatic metalens," *Nature Communications*, vol. 11, p. 3892, 2020.

[11] Y. Ogura, N. Shirai, J. Tanida, and Y. Ichioka, "Wavelength-multiplexing diffractive phase elements: design, fabrication, and performance evaluation," *Journal of the Optical Society of America A*, vol. 18, no. 5, p. 1082, 2001.

[12] X. Ju, C. Xu, X. Han, X. Du, G. Wei, and Y. Yang, "A review of the concentrated photovoltaic/thermal (CPVT) hybrid solar systems based on the spectral beam splitting technology," *Applied Energy*, vol. 187, pp. 534–563, 2017.

[13] A. Mojiri, R. Taylor, E. Thomsen, and G. Rosengarten, "Spectral beam splitting for efficient conversion of solar energy—a review," *Renewable and Sustainable Energy Reviews*, vol. 28, pp. 654–663, 2013.

[14] D. Lan and M. A. Green, "Pathways towards a 50% efficiency spectrum-splitting photovoltaic system: Application of built-in filters and generalization of concept," *Energy Procedia*, vol. 150, pp. 83–86, 2018.

[15] S. D. Vorndran, L. Johnson, T. Milster, and R. K. Kostuk, "Measurement and analysis of algorithmically-designed diffractive optic for photovoltaic spectrum splitting," in *2016 IEEE 43rd Photovoltaic Specialists Conference (PVSC)*, pp. 3513–3517, IEEE, 2016.

[16] S. D. Vorndran, S. Ayala, Y. Wu, J. M. Russo, M. A. Zaverton, T. Milster, and R. K. Kostuk, "Freeform surface relief diffractive optic for photovoltaic spectrum splitting," in *2015 IEEE 42nd Photovoltaic Specialist Conference (PVSC)*, pp. 1–5, Proc. IEEE, 1-5, 2015.

[17] A. Tittl, A. Leitis, M. Liu, F. Yesilkoy, D.-Y. Choi, D. N. Neshev, Y. S. Kivshar, and H. Altug, "Imaging-based molecular barcoding with pixelated dielectric metasurfaces," *Science*, vol. 360, no. 6393, pp. 1105–1109, 2018.

[18] G. Zheng, H. Mühlenbernd, M. Kenney, G. Li, T. Zentgraf, and S. Zhang, "Metasurface holograms reaching 80% efficiency," *Nature Nanotechnology*, vol. 10, no. 4, pp. 308–312, 2015.

[19] F. Aieta, M. A. Kats, P. Genevet, and F. Capasso, “Multiwavelength achromatic metasurfaces by dispersive phase compensation,” *Science*, vol. 347, no. 6228, pp. 1342–1345, 2015.

[20] X. Wan, B. Shen, and R. Menon, “Diffractive lens design for optimized focusing,” *Journal of the Optical Society of America A*, vol. 31, no. 12, p. B27, 2014.

[21] F. Aieta, P. Genevet, M. A. Kats, N. Yu, R. Blanchard, Z. Gaburro, and F. Capasso, “Aberration-free ultrathin flat lenses and axicons at telecom wavelengths based on plasmonic metasurfaces,” *Nano Letters*, vol. 12, no. 9, pp. 4932–4936, 2012.

[22] M. Khorasaninejad, W. T. Chen, R. C. Devlin, J. Oh, A. Y. Zhu, and F. Capasso, “Metalenses at visible wavelengths: Diffraction-limited focusing and subwavelength resolution imaging,” *Science*, vol. 352, no. 6290, pp. 1190–1194, 2016.

[23] B. N. Gün and E. Yüce, “Wavefront shaping assisted design of spectral splitters and solar concentrators,” *Scientific Reports*, vol. 11, p. 2825, 2021.

[24] M. Parker, A. Cohen, and R. Mears, “Dynamic digital holographic wavelength filtering,” *Journal of Lightwave Technology*, vol. 16, no. 7, pp. 1259–1270, 1998.

[25] M. Makowski, I. Ducin, M. Sypek, A. Siemion, A. Siemion, J. Suszek, and A. Kolodziejczyk, “Color image projection based on fourier holograms,” *Optics Letters*, vol. 35, no. 8, p. 1227, 2010.

[26] P. J. Smith, C. M. Taylor, A. J. Shaw, and E. M. McCabe, “Programmable array microscopy with a ferroelectric liquid-crystal spatial light modulator,” *Applied Optics*, vol. 39, no. 16, p. 2664, 2000.

[27] Y. Hayasaki, M. Itoh, T. Yatagai, and N. Nishida, “Nonmechanical optical manipulation of microparticle using spatial light modulator,” *Optical Review*, vol. 6, no. 1, pp. 24–27, 1999.

[28] https://holoeye.com/slm-pluto-phase only/, Accessed: 15 August 2021.

[29] D. R. Pape and L. J. Hornbeck, “Characteristics of the deformable mirror device for optical information processing,” *Optical Engineering*, vol. 22, no. 6, 1983.

[30] S. A. Goorden, J. Bertolotti, and A. P. Mosk, “Superpixel-based spatial amplitude and phase modulation using a digital micromirror device,” *Optics Express*, vol. 22, no. 15, p. 17999, 2014.

[31] D. Akbulut, Measurements of strong correlations in the transport of light through strongly scattering materials. PhD thesis, University of Twente, 2013.

[32] D. Xu, T. Jiang, A. Li, B. Hu, Z. Feng, H. Gong, S. Zeng, and Q. Luo, “Fast optical sectioning obtained by structured illumination microscopy using a digital mirror device,” *Journal of Biomedical Optics*, vol. 18, no. 6, p. 060503, 2013.

[33] H. Wu, W. Hu, H. chao Hu, X. wen Lin, G. Zhu, J.-W. Choi, V. Chigrinov, and Y. qing Lu, “Arbitrary photo-patterning in liquid crystal alignments using DMD based lithography system,” *Optics Express*, vol. 20, no. 15, p. 16684, 2012.

[34] J. Jang, J. Lim, H. Yu, H. Choi, J. Ha, J.-H. Park, W.-Y. Oh, W. Jang, S. Lee, and Y. Park, “Complex wavefront shaping for optimal depth-selective focusing in optical coherence tomography,” *Optics Express*, vol. 21, no. 3, p. 2890, 2013.

[35] https://ibsen.com/technology/spectrometer-tutorial/dmd spectrometers/, Accessed: 15 Aug. 2021.

[36] G. Kim, J. A. Domínguez-Caballero, and R. Menon, “Design and analysis of multi-wavelength diffractive optics,” *Optics Express*, vol. 20, no. 3, p. 2814, 2012.

[37] Q. Huang, J. Wang, B. Quan, Q. Zhang, D. Zhang, D. Li, Q. Meng, L. Pan, Y. Wang, and G. Yang, “Design and fabrication of a diffractive optical element as a spectrum-splitting solar concentrator for lateral multijunction solar cells,” *Applied Optics*, vol. 52, no. 11, pp. 2312–2319, 2013.

[38] S. Banerji, M. Meem, A. Majumder, F. G. Vasquez, B. Sensale-Rodriguez, and R. Menon, “Imaging with flat optics: metalenses or diffractive lenses?,” *Optica*, vol. 6, no. 6, pp. 805–810, 2019.

[39] S. Mao, L. Zhao, and J. Zhao, “Integral diffraction efficiency model for multilayer diffractive optical elements with wide angles of incidence in case of polychromatic light,” *Optics Express*, vol. 27, no. 15, pp. 21497–21507, 2019.

[40] S. Mao and J. Zhao, “Diffractive optical element optimization under wide incident angle and waveband situations,” *Optics Communications*, vol. 458, p. 124762, 2020.

[41] N. Bao, Z. Chen, and J. Zhang, “Phase-only diffractive optical element for improving the beam quality of a vertical-cavity surface-emitting laser array,” *Optik*, vol. 115, no. 1, pp. 23–27, 2004.

[42] Z. Hu, J. Zhu, B. Yang, Y. Xiao, A. Zeng, and H. Huang, “Mixed multi-region design of diffractive optical element for projection exposure system,” *Optik*, vol. 124, no. 22, pp. 5573–5576, 2013.

[43] Z. Le, A. Lapchuk, I. Gorbov, Z. Lu, S. Yao, I. Kosyak, T. Kliuieva, Y. Guo, and O. Prygun, “Theory and experiments based on tracked moving flexible DOE loops for speckle suppression in compact laser projection,” *Optics and Lasers in Engineering*, vol. 124, p. 105845, 2020.

[44] Z. Li, M. Taphanel, T. Längle, and J. Beyerer, “Application of DOE in confocal microscopy for surface measurement,” in *Photonics and Education in Measurement Science 2019*, SPIE, 2019.

[45] M. N. Erim, N. Erim, and H. Kurt, “Spectral splitting for an InGaP/GaAs parallel junction solar cell,” *Applied Optics*, vol. 58, no. 16, pp. 4265–4270, 2019.

[46] G. Kim, J. A. Dominguez-Caballero, H. Lee, D. J. Friedman, and R. Menon, “Increased photovoltaic power output via diffractive spectrum separation,” *Physical Review Letters*, vol. 110, no. 12, p. 123901, 2013.

[47] A. Imenes and D. Mills, “Spectral beam splitting technology for increased conversion efficiency in solar concentrating systems: a review,” *Solar Energy Materials and Solar Cells*, vol. 84, pp. 19–69, 2004.

[48] E. Arbabi, A. Arbabi, S. M. Kamali, Y. Horie, and A. Faraon, "Multiwavelength polarization-insensitive lenses based on dielectric metasurfaces with meta-molecules," *Optica*, vol. 3, no. 6, pp. 628–633, 2016.

[49] R. Fernández, S. Gallego, A. Márquez, C. Neipp, E. M. Calzado, J. Francés, M. Morales-Vidal, and A. Beléndez, "Complex diffractive optical elements stored in photopolymers," *Polymers*, vol. 11, no. 12, p. 1920, 2019.

[50] X. Yu, Z.-X. Xie, J.-H. Liu, Y. Zhang, H.-B. Wang, and Y. Zhang, "Optimization design of a diffractive axicon for improving the performance of long focal depth," *Optics Communications*, vol. 330, pp. 1–5, 2014.

[51] M. B. Fleming and M. C. Hutley, "Blazed diffractive optics," *Applied Optics*, vol. 36, no. 20, pp. 4635–4643, 1997.

[52] R. Fernández, S. Gallego, A. Márquez, J. Francés, F. J. Marínez, and A. Beléndez, "Influence of index matching on AA/PVA photopolymers for low spatial frequency recording," *Applied Optics*, vol. 54, no. 11, pp. 3132–3140, 2015.

[53] T. Shiono and H. Ogawa, "Diffraction-limited blazed reflection diffractive microlenses for oblique incidence fabricated by electron-beam lithography," *Applied Optics*, vol. 30, no. 25, pp. 3643–3649, 1991.

[54] T. P. Xiao, O. S. Cifci, S. Bhargava, H. Chen, T. Gissibl, W. Zhou, H. Giessen, K. C. Toussaint, E. Yablonovitch, and P. V. Braun, "Diffractive spectral-splitting optical element designed by adjoint-based electromagnetic optimization and fabricated by femtosecond 3D direct laser writing," *ACS Photonics*, vol. 3, no. 5, pp. 886–894, 2016.

[55] D. Liu, Y. Tan, E. Khoram, and Z. Yu, "Training deep neural networks for the inverse design of nanophotonic structures," *ACS Photonics*, vol. 5, no. 4, p. 1365–1369, 2018.

[56] J. Read, B. Pfahringer, G. Holmes, and E. Frank, "Classifier chains for multi-label classification," *Machine Learning*, vol. 85, no. 3, pp. 333–359, 2011.

[57] J. Fürnkranz, E. Hüllermeier, E. L. Mencía, and K. Brinker, "Multilabel classification via calibrated label ranking," *Machine Learning*, vol. 73, no. 2, pp. 133–153, 2008.

[58] O. Schultz, S. W. Glunz, and G. P. Willeke, “SHORT COMMUNICATION: ACCELERATED PUBLICATION: Multicrystalline silicon solar cells exceeding 20% efficiency,” *Progress in Photovoltaics: Research and Applications*, vol. 12, no. 7, pp. 553–558, 2004.

[59] J. Zhao, A. Wang, M. A. Green, and F. Ferrazza, “19.8% efficient “honeycomb” textured multicrystalline and 24.4% monocrystalline silicon solar cells,” *Applied Physics Letters*, vol. 73, no. 14, pp. 1991–1993, 1998.

[60] E. Karabudak, E. Yüce, S. Schlautmann, O. Hansen, G. Mul, and H. J. Gardeniers, “On the pathway of photoexcited electrons: probing photon-to-electron and photon-to-phonon conversions in silicon by ATR-IR,” *Physical Chemistry Chemical Physics*, vol. 14, no. 31, p. 10882, 2012.

[61] A. Polman and H. A. Atwater, “Photonic design principles for ultrahigh-efficiency photovoltaics,” *Nature Materials*, vol. 11, no. 3, pp. 174–177, 2012.

[62] N. J. Liew and H.-J. Lee, “Numerical analysis of hybrid photovoltaic-thermal systems utilizing different spectral bandpass filters,” *Renewable Energy*, vol. 144, pp. 15–29, 2019.

[63] G. Wang, Y. Yao, J. Lin, Z. Chen, and P. Hu, “Design and thermodynamic analysis of a novel solar CPV and thermal combined system utilizing spectral beam splitter,” *Renewable Energy*, vol. 155, pp. 1091–1102, 2020.

[64] J. L. Stone, “Photovoltaics: Unlimited electrical energy from the sun,” *Physics Today*, vol. 46, no. 9, pp. 22–29, 1993.

[65] A. D. Vos, “Detailed balance limit of the efficiency of tandem solar cells,” *Journal of Physics D: Applied Physics*, vol. 13, no. 5, pp. 839–846, 1980.

[66] B.-Z. Dong, G.-Q. Zhang, G.-Z. Yang, B.-Y. Gu, S.-H. Zheng, D.-H. Li, Y.-S. Chen, X.-M. Cui, M.-L. Chen, and H.-D. Liu, “Design and fabrication of a diffractive phase element for wavelength demultiplexing and spatial focusing simultaneously,” *Applied Optics*, vol. 35, p. 6859, 1996.

[67] C. Stanley, A. Mojiri, and G. Rosengarten, “Spectral light management for solar energy conversion systems,” *Nanophotonics*, vol. 5, no. 1, p. 161, 2016.

[68] N. Mohammad, P. Wang, D. J. Friedman, and R. Menon, "Enhancing photovoltaic output power by 3-band spectrum-splitting and concentration using a diffractive micro-optic," *Optics Express*, vol. 22, no. S6, p. A1519, 2014.

[69] N. Mohammad, M. Schulz, P. Wang, and R. Menon, "Outdoor measurements of a photovoltaic system using diffractive spectrum-splitting and concentration," *AIP Advances*, vol. 6, no. 9, p. 095311, 2016.

[70] J. M. Hollas, *Modern Spectroscopy.* John Wiley & Sons, 2004.

[71] K. Kong, C. Kendall, N. Stone, and I. Notingher, "Raman spectroscopy for medical diagnostics — from in-vitro biofluid assays to in-vivo cancer detection," *Advanced Drug Delivery Reviews*, vol. 89, pp. 121–134, 2015.

[72] J. U. Porep, D. R. Kammerer, and R. Carle, "On-line application of near infrared (NIR) spectroscopy in food production," *Trends in Food Science & Technology*, vol. 46, no. 2, pp. 211–230, 2015.

[73] A. Yolalmaz, F. H. Sadroud, M. Danışman, and O. Esenturk, "Intracavity gas detection with fiber loop ring down spectroscopy," *Optics Communications*, vol. 396, pp. 141–145, 2017.

[74] Y. S. Aytekin, M. Köktürk, A. Zaczek, T. M. Korter, E. J. Heilweil, and O. Esenturk, "Optical properties of meloxicam in the far-infrared spectral region," *Chemical Physics*, vol. 512, pp. 36–43, 2018.

[75] A. Yolalmaz, M. F. Danışman, and O. Esenturk, "Discrimination of chemicals via refractive index by EF-FLRD," *Applied Physics B*, vol. 125, no. 9, 2019.

[76] A. Rygula, K. Majzner, K. M. Marzec, A. Kaczor, M. Pilarczyk, and M. Baranska, "Raman spectroscopy of proteins: a review," *Journal of Raman Spectroscopy*, vol. 44, no. 8, pp. 1061–1076, 2013.

[77] S. L. Jacques, "Optical properties of biological tissues: a review," *Physics in Medicine and Biology*, vol. 58, no. 11, pp. R37–R61, 2013.

[78] D. Gabor, "A new microscopic principle," *Nature*, vol. 161, no. 4098, pp. 777–778, 1948.

[79] D. Gabor, “Microscopy by reconstructed wave-fronts,” *Proceedings of the Royal Society of London. Series A. Mathematical and Physical Sciences*, vol. 197, no. 1051, pp. 454–487, 1949.

[80] X. Fang, H. Ren, and M. Gu, “Orbital angular momentum holography for high-security encryption,” *Nature Photonics*, vol. 14, no. 2, pp. 102–108, 2020.

[81] M. Liebel, N. Pazos-Perez, N. F. van Hulst, and R. A. Alvarez-Puebla, “Surface-enhanced raman scattering holography,” *Nature Nanotechnology*, vol. 15, no. 12, pp. 1005–1011, 2020.

[82] N. Yoneda, Y. Saita, and T. Nomura, “Binary computer-generated-hologram-based holographic data storage,” *Applied Optics*, vol. 58, no. 12, p. 3083, 2019.

[83] B. Javidi and E. Tajahuerce, “Three-dimensional object recognition by use of digital holography,” *Optics Letters*, vol. 25, no. 9, p. 610, 2000.

[84] A. Yolalmaz and E. Yüce, “Spectral splitting and concentration of broadband light using neural networks,” *APL Photonics*, vol. 6, no. 4, p. 046101, 2021.

[85] Y. Rivenson, Y. Zhang, H. Günaydın, D. Teng, and A. Ozcan, “Phase recovery and holographic image reconstruction using deep learning in neural networks,” *Light: Science & Applications*, vol. 7, no. 2, pp. 17141–17141, 2017.

[86] F. Anselmi, C. Ventalon, A. Begue, D. Ogden, and V. Emiliani, “Three-dimensional imaging and photostimulation by remote-focusing and holographic light patterning,” *Proceedings of the National Academy of Sciences*, vol. 108, no. 49, pp. 19504–19509, 2011.

[87] Y. Kim, E. Stoykova, H. Kang, S. Hong, J. Park, J. Park, and J. Hong, “Seamless full color holographic printing method based on spatial partitioning of SLM,” *Optics Express*, vol. 23, no. 1, p. 172, 2015.

[88] G. D. Love, “Wave-front correction and production of zernike modes with a liquid-crystal spatial light modulator,” *Applied Optics*, vol. 36, no. 7, p. 1517, 1997.

[89] E. Moon, M. Kim, J. Roh, H. Kim, and J. Hahn, “Holographic head-mounted

display with RGB light emitting diode light source," *Optics Express*, vol. 22, no. 6, p. 6526, 2014.

[90] R. Zhao, B. Sain, Q. Wei, C. Tang, X. Li, T. Weiss, L. Huang, Y. Wang, and T. Zentgraf, "Multichannel vectorial holographic display and encryption," *Light: Science & Applications*, vol. 7, no. 1, 2018.

[91] K. Hong, J. Yeom, C. Jang, J. Hong, and B. Lee, "Full-color lens-array holographic optical element for three-dimensional optical see-through augmented reality," *Optics Letters*, vol. 39, no. 1, p. 127, 2013.

[92] U. Schnars and W. Jueptner, *Digital Holography*. Springer, 2005.

[93] M. Schnell, P. S. Carney, and R. Hillenbrand, "Synthetic optical holography for rapid nanoimaging," *Nature Communications*, vol. 5, no. 3499, p. 3499, 2014.

[94] J. Rosen and G. Brooker, "Digital spatially incoherent fresnel holography," *Optics Letters*, vol. 32, no. 8, p. 912, 2007.

[95] M. A. Wani, F. A. Bhat, S. Afzal, and A. I. Khan, *Advances in Deep Learning*. Springer Singapore, 2020.

[96] Y. Rivenson, Z. Göröcs, H. Günaydin, Y. Zhang, H. Wang, and A. Ozcan, "Deep learning microscopy," *Optica*, vol. 4, no. 11, p. 1437, 2017.

[97] H. Wang, Y. Rivenson, Y. Jin, Z. Wei, R. Gao, H. Günaydın, L. A. Bentolila, C. Kural, and A. Ozcan, "Deep learning enables cross-modality super-resolution in fluorescence microscopy," *Nature Methods*, vol. 16, no. 1, pp. 103–110, 2018.

[98] Y. Rivenson, H. C. Koydemir, H. Wang, Z. Wei, Z. Ren, H. Günaydın, Y. Zhang, Z. Göröcs, K. Liang, D. Tseng, and A. Ozcan, "Deep learning enhanced mobile-phone microscopy," *ACS Photonics*, vol. 5, pp. 2354–2364, 2018.

[99] Y. Xue, S. Cheng, Y. Li, and L. Tian, "Reliable deep-learning-based phase imaging with uncertainty quantification," *Optica*, vol. 6, no. 5, p. 618, 2019.

[100] P. Caramazza, O. Moran, R. Murray-Smith, and D. Faccio, “Transmission of natural scene images through a multimode fibre,” *Nature Communications*, vol. 10, no. 1, 2019.

[101] C. F. Higham, R. Murray-Smith, M. J. Padgett, and M. P. Edgar, “Deep learning for real-time single-pixel video,” *Scientific Reports*, vol. 8, no. 1, 2018.

[102] A. Sinha, J. Lee, S. Li, and G. Barbastathis, “Lensless computational imaging through deep learning,” *Optica*, vol. 4, no. 9, p. 1117, 2017.

[103] J. Jiang, D. Sell, S. Hoyer, J. Hickey, J. Yang, and J. A. Fan, “Free-form diffractive metagrating design based on generative adversarial networks,” *ACS Nano*, vol. 13, no. 8, p. 8872–8878, 2019.

[104] C. C. Nadell, B. Huang, J. M. Malof, and W. J. Padilla, “Deep learning for accelerated all-dielectric metasurface design,” *Optics Express*, vol. 27, no. 20, p. 27523, 2019.

[105] J. Jiang and J. A. Fan, “Global optimization of dielectric metasurfaces using a physics-driven neural network,” *Nano Letters*, vol. 19, no. 8, p. 5366–5372, 2019.

[106] T. Zahavy, A. Dikopoltsev, D. Moss, G. I. Haham, O. Cohen, S. Mannor, and M. Segev, “Deep learning reconstruction of ultrashort pulses,” *Optica*, vol. 5, p. 666, 2018.

[107] A. Esteva, B. Kuprel, R. A. Novoa, J. Ko, S. M. Swetter, H. M. Blau, and S. Thrun, “Dermatologist-level classification of skin cancer with deep neural networks,” *Nature*, vol. 542, no. 7639, pp. 115–118, 2017.

[108] D. Mikhaylov, B. Zhou, T. Kiedrowski, R. Mikut, and A.-F. Lasagni, “High accuracy beam splitting using spatial light modulator combined with machine learning algorithms,” *Optics and Lasers in Engineering*, vol. 121, pp. 227–235, 2019.

[109] B. Mills, D. J. Heath, J. A. Grant-Jacob, and R. W. Eason, “Predictive capabilities for laser machining via a neural network,” *Optics Express*, vol. 26, no. 13, p. 17245, 2018.

[110] D. J. Heath, J. A. Grant-Jacob, Y. Xie, B. S. Mackay, J. A. G. Baker, R. W. Eason, and B. Mills, “Machine learning for 3d simulated visualization of laser machining,” *Optics Express*, vol. 26, no. 17, p. 21574, 2018.

[111] R. Velik, “Discrete fourier transform computation using neural networks,” in *2008 International Conference on Computational Intelligence and Security*, IEEE, 2008.

[112] J. W. Goodman, Introduction to Fourier optics. Roberts & Company, 1996.

[113] S. Y. Tong, H. Li, and H. Huang, “Energy extension in three-dimensional atomic imaging by electron emission holography,” *Physical Review Letters*, vol. 67, no. 22, pp. 3102–3105, 1991.

[114] D. Kim and B. Javidi, “Distortion-tolerant 3-d object recognition by using single exposure on-axis digital holography,” *Optics Express*, vol. 12, no. 22, p. 5539, 2004.

[115] H. Li, X. Chen, Z. Chi, C. Mann, and A. Razi, “Deep DIH: Single-shot digital in-line holography reconstruction by deep learning,” *IEEE Access*, vol. 8, pp. 202648–202659, 2020.

[116] D. H, “Spectral characteristics of stepped-phase gratings,” *Optik*, vol. 53, pp. 409–417, 1979.

[117] A. Jesacher, S. Bernet, and M. Ritsch-Marte, “Broadband suppression of the zero diffraction order of an SLM using its extended phase modulation range,” *Optics Express*, vol. 22, no. 14, p. 17590, 2014.

[118] I. M. Vellekoop, Controlling the propagation of light in disordered scattering media. PhD thesis, University of Twente, 2008.

[119] A. Yolalmaz and E. Yüce, “Hybrid design of spectral splitters and concentrators of light for solar cells using iterative search and neural networks,” *Photonics and Nanostructures - Fundamentals and Applications*, vol. 48, p. 100987, 2022.

[120] A. Yolalmaz and E. Yüce, “Angle-independent diffractive optical elements for efficient solar energy conversion,” in *Proc. SPIE 11366, 113660Q*, SPIE, 2020.

[121] A. Yolalmaz and E. Yüce, “Designs of diffractive optical elements for solar energy harvesting,” in *2019 International Conference on Power Generation Systems and Renewable Energy Technologies (PGSRET)*, Proc. IEEE, 1-5, 2019.

[122] A. Arbabi, Y. Horie, M. Bagheri, and A. Faraon, “Dielectric metasurfaces for complete control of phase and polarization with subwavelength spatial resolution and high transmission,” *Nature Nanotechnology*, vol. 10, p. 937–943, 2015.

[123] D. Sell, J. Yang, S. Doshay, K. Zhang, and J. A. Fan, “Visible light metasurfaces based on single-crystal silicon,” *ACS Photonics*, vol. 10, no. 3, pp. 1919–1925, 2016.

[124] M. Faraji-Dana, E. Arbabi, A. Arbabi, S. M. Kamali, H. Kwon, and A. Faraon, “Compact folded metasurface spectrometer,” *Nature Communications*, vol. 9, no. 4196, p. 960, 2018.

[125] V. S. Lin, “A porous silicon-based optical interferometric biosensor,” *Science*, vol. 278, no. 5339, pp. 840–843, 1997.

[126] A. Y. Piggott, J. Lu, K. G. Lagoudakis, J. Petykiewicz, T. M. Babinec, and J. Vučković, “Inverse design and demonstration of a compact and broadband on-chip wavelength demultiplexer,” *Nature Photonics*, vol. 9, no. 6, pp. 374–377, 2015.

[127] A. L. Holsteen, D. Lin, I. Kauvar, G. Wetzstein, and M. L. Brongersma, “A light-field metasurface for high-resolution single-particle tracking,” *Nano Letters*, vol. 19, no. 4, p. 2267–2271, 2019.

[128] N. Borhani, E. Kakkava, C. Moser, and D. Psaltis, “Learning to see through multimode fibers,” *Optica*, vol. 5, no. 8, p. 960, 2018.

[129] X. Lin, Y. Rivenson, N. T. Yardimci, M. Veli, Y. Luo, M. Jarrahi, and A. Ozcan, “All-optical machine learning using diffractive deep neural networks,” *Science*, vol. 361, no. 6406, pp. 1004–1008, 2018.

[130] P. Kok, W. J. Munro, K. Nemoto, T. C. Ralph, J. P. Dowling, and G. J. Milburn, “Linear optical quantum computing with photonic qubits,” *Reviews of Modern Physics*, vol. 79, no. 1, pp. 135–174, 2007.

[131] A. K. Azad, W. J. M. Kort-Kamp, M. Sykora, N. R. Weisse-Bernstein, T. S. Luk, A. J. Taylor, D. A. R. Dalvit, and H.-T. Chen, “Metasurface broadband solar absorber,” *Scientific Reports*, vol. 6, p. 20347, 2016.

[132] G. K. Mor, O. K. Varghese, M. Paulose, K. Shankar, and C. A. Grimes, “A review on highly ordered, vertically oriented TiO2 nanotube arrays: Fabrication, material properties, and solar energy applications,” *Solar Energy Materials and Solar Cells*, vol. 90, no. 14, pp. 2011–2075, 2006.

[133] J. You, L. Dou, K. Yoshimura, T. Kato, K. Ohya, T. Moriarty, K. Emery, C.-C. Chen, J. Gao, G. Li, and Y. Yang, “A polymer tandem solar cell with 10.6% power conversion efficiency,” *Nature Communications*, vol. 4, no. 1446, 2013.

[134] M. A. Green, A. Ho-Baillie, and H. J. Snaith, “The emergence of perovskite solar cells,” *Nature Photonics*, vol. 8, no. 7, pp. 506–514, 2014.

[135] Z. He, C. Zhong, S. Su, M. Xu, H. Wu, and Y. Cao, “Enhanced power-conversion efficiency in polymer solar cells using an inverted device structure,” *Nature Photonics*, vol. 6, no. 9, pp. 591–595, 2012.

[136] W. Shockley and H. J. Queisser, “Detailed balance limit of efficiency of p-n junction solar cells,” *Journal of Applied Physics*, vol. 32, no. 3, pp. 510–519, 1961.

[137] M. A. Green, K. Emery, Y. Hishikawa, W. Warta, and E. D. Dunlop, “Solar cell efficiency tables (version 42),” *Progress in Photovoltaics: Research and Applications*, vol. 21, no. 5, pp. 827–837, 2013.

[138] L. A. A. Bunthof, E. J. Haverkamp, D. van der Woude, G. J. Bauhuis, W. H. M. Corbeek, S. Veelenturf, E. Vlieg, and J. J. Schermer, “Influence of laterally split spectral illumination on multi-junction cpv solar cell performance,” *Solar Energy*, vol. 170, pp. 86–94, 2018.

[139] C. Stanleya, A. Mojiria, M. Rahata, A. Blakersb, and G. Rosengartena, “Performance testing of a spectral beam splitting hybrid pvt solar receiver for linear concentrators,” *Applied Energy*, vol. 168, pp. 303–313, 2016.

[140] A. Jesacher, S. Bernet, and M. Ritsch-Marte, “Colour hologram projection with an SLM by exploiting its full phase modulation range,” *Optics Express*, vol. 22, no. 17, p. 20530, 2014.

[141] Q. Huang, Q. Peng, J. Hu, H. Xu, C. Jiang, and Q. Liu, “Design of a high-efficiency and low-cost reflection-type diffractive optical element as the spectrum splitting solar concentrator for lateral multi-junction solar cells architecture,” in *Proc. IEEE*, pp. 1528–1532, IEEE, 2016.

[142] Y. Başay and E. Yüce, “Broadband spectral splitting of white light via 2D diffractive optical elements,” *Turkish Journal of Physics*, vol. 42, no. 5, pp. 501–508, 2018.

[143] M. A. Seldowitz, J. P. Allebach, and D. W. Sweeney, “Synthesis of digital holograms by direct binary search,” *Applied Optics*, vol. 26, no. 14, p. 2788, 1987.

[144] N. Mohammad, M. Meem, B. Shen, P. Wang, and R. Menon, “Broadband imaging with one planar diffractive lens,” *Scientific Reports*, vol. 8, no. 1, p. 2799, 2018.

[145] R. W. Gerchberg and W. O. Saxton, “A practical algorithm for the determination of phasefrom image and diffraction plane pictures,” *Optik*, vol. 35, no. 2, pp. 237–246, 1972.

[146] H. Wang, W. Yue, Q. Song, J. Liu, and G. Situ, “A hybrid gerchberg–saxton-like algorithm for DOE and CGH calculation,” *Optics and Lasers in Engineering*, vol. 89, pp. 109–115, 2017.

[147] S. Vorndran, J. M. Russo, Y. Wu, S. A. Pelaez, and R. K. Kostuk, “Broadband gerchberg-saxton algorithm for freeform diffractive spectral filter design,” *Optics Express*, vol. 23, no. 24, p. A1512, 2015.

[148] G.-Z. Yang, B.-Z. Dong, B.-Y. Gu, J.-Y. Zhuang, and O. K. Ersoy, “Gerchberg-Saxton and Yang-Gu algorithms for phase retrieval in a nonunitary transform system: a comparison,” *Applied Optics*, vol. 33, no. 2, p. 209, 1994.

[149] E. G. Johnson, A. D. Kathman, D. H. Hochmuth, A. L. Cook, D. R. Brown, and W. F. Delaney, “Advantages of genetic algorithm optimization methods in diffractive optic design,” in *Proc. SPIE 10271, 1027105*, 1993.

[150] M. Chen, J. Jiang, and J. A. Fan, “Design space reparameterization enforces hard geometric constraints in inverse-designed nanophotonic devices,” *ACS Photonics*, vol. 7, no. 11, pp. 3141–3151, 2020.

[151] P. R. Wiecha, A. Arbouet, C. Girard, and O. L. Muskens, “Deep learning in nano-photonics: inverse design and beyond,” *Photonics Research*, vol. 9, no. 5, p. B182, 2021.

[152] S. Haghanifar, M. McCourt, B. Cheng, J. Wuenschell, P. Ohodnicki, and P. W. Leu, “Discovering high-performance broadband and broad angle antireflection surfaces by machine learning,” *Optica*, vol. 7, p. 784, 2020.

[153] D. Zhu, Z. Liu, L. Raju, A. S. Kim, and W. Cai, “Multifunctional meta-optic systems: Inversely designed with artificial intelligence,.” arXiv:2007.00130 2020.

[154] S. Chugh, A. Gulistan, S. Ghosh, and B. M. A. Rahman, “Machine learning approach for computing optical properties of a photonic crystal fiber,” *Optics Express*, vol. 27, no. 25, p. 36414, 2019.

[155] M. Raissi, P. Perdikaris, and G. Karniadakis, “Physics-informed neural networks: A deep learning framework for solving forward and inverse problems involving nonlinear partial differential equations,” *Journal of Computational Physics*, vol. 378, pp. 686–707, 2019.

[156] O. Tokel, A. Turnalı, G. Makey, P. Elahi, T. Çolakoğlu, E. Ergeçen, Ŏ. Yavuz, R. Hübner, M. Z. Borra, I. Pavlov, A. Bek, R. Turan, D. K. Kesim, S. Tozburun, S. Ilday, and F. Ömer Ilday, “In-chip microstructures and photonic devices fabricated by nonlinear laser lithography deep inside silicon,” *Nature Photonics*, vol. 11, no. 10, pp. 639–645, 2017.

[157] “Refractive index of bk-7 glass.” https://www.schott.com, Accessed: 1 April 2019.

[158] "Guppy pro technical manual," *Allied Vis. Technol. GmbH Taschenweg 2a, 07646 Stadtroda / Ger.*, vol. v4.1.5, p. 49, 2019.

[159] S. Divitt and L. Novotny, "Spatial coherence of sunlight and its implications for light management in photovoltaics," *Optica*, vol. 2, p. 95, 2015.

[160] D.-F. Lin, B.-G. Quan, Q.-L. Zhang, D.-X. Zhang, X. Xu, J.-S. Ye, Y. Zhang, D.-M. Li, Q.-B. Meng, L. Pan, and G.-Z. Yang, "Spectrum-splitting diffractive optical element of high concentration factor and high optical efficiency for three-junction photovoltaics," *Chinese Physics Letters*, vol. 33, no. 9, p. 094207, 2016.

[161] W. T. Chen, A. Y. Zhu, V. Sanjeev, M. Khorasaninejad, Z. Shi, E. Lee, and F. Capasso, "A broadband achromatic metalens for focusing and imaging in the visible," *Nature Nanotechnology*, vol. 13, no. 3, pp. 220–226, 2018.

[162] E. Yüce, A. Yolalmaz, and Ç. A. Yüksel, "Optical spectrometer based on alternating diffractive optical elements," Turkish Patent 2020-GE-288969 2020.

[163] E. Kaya, N. Kakenov, H. Altan, C. Kocabas, and O. Esenturk, "Multilayer graphene broadband terahertz modulators with flexible substrate," *Journal of Infrared, Millimeter, and Terahertz Waves*, vol. 39, no. 5, pp. 483–491, 2018.

[164] C. P. Bacon, Y. Mattley, and R. DeFrece, "Miniature spectroscopic instrumentation: Applications to biology and chemistry," *Review of Scientific Instruments*, vol. 75, no. 1, pp. 1–16, 2004.

[165] N. R. McQuaker, P. D. Kluckner, and G. N. Chang, "Calibration of an inductively coupled plasma-atomic emission spectrometer for the analysis of environmental materials," *Analytical Chemistry*, vol. 51, no. 7, pp. 888–895, 1979.

[166] A. Yolalmaz and E. Yüce, "Comprehensive deep learning model for 3D color holography," *Scientific Reports*, vol. 12, no. 1, p. 2487, 2022.

[167] B. Javidi and T. Nomura, "Securing information by use of digital holography," *Optics Letters*, vol. 25, no. 1, p. 28, 2000.

[168] R. D. Leonardo and S. Bianchi, "Hologram transmission through multi-mode optical fibers," *Optics Express*, vol. 19, no. 1, p. 247, 2010.

[169] J. Zhang, N. Pégard, J. Zhong, H. Adesnik, and L. Waller, "3D computer-generated holography by non-convex optimization," *Optica*, vol. 4, no. 10, p. 1306, 2017.

[170] V. Kettunen, "Review of iterative Fourier-transform algorithms for beam shaping applications," *Optical Engineering*, vol. 43, no. 11, p. 2549, 2004.

[171] R. W. Gerchberg and W. O. Saxton, "A practical algorithm for the determination of phase from image and diffraction plane pictures," *Optik*, vol. 35, no. 2, pp. 237–246, 1972.

[172] G. Liu and P. D. Scott, "Phase retrieval and twin-image elimination for in-line Fresnel holograms," *Journal of the Optical Society of America A*, vol. 4, no. 1, p. 159, 1987.

[173] J. R. Fienup, "Phase retrieval algorithms: a comparison," *Applied Optics*, vol. 21, no. 15, p. 2758, 1982.

[174] Y. Wu, A. Ray, Q. Wei, A. Feizi, X. Tong, E. Chen, Y. Luo, and A. Ozcan, "Deep learning enables high-throughput analysis of particle-aggregation-based biosensors imaged using holography," *ACS Photonics*, vol. 6, no. 2, pp. 294–301, 2018.

[175] Y. Wu, Y. Luo, G. Chaudhari, Y. Rivenson, A. Calis, K. de Haan, and A. Ozcan, "Bright-field holography: cross-modality deep learning enables snapshot 3d imaging with bright-field contrast using a single hologram," *Light: Science & Applications*, vol. 8, p. 1, 2019.

[176] K. Jaferzadeh, S.-H. Hwang, I. Moon, and B. Javidi, "No-search focus prediction at the single cell level in digital holographic imaging with deep convolutional neural network," *Biomedical Optics Express*, vol. 10, no. 8, p. 4276, 2019.

[177] K. Ning, X. Zhang, X. Gao, T. Jiang, H. Wang, S. Chen, A. Li, and J. Yuan, "Deep-learning-based whole-brain imaging at single-neuron resolution," *Biomedical Optics Express*, vol. 11, no. 7, p. 3567, 2020.

[178] L. Shi, B. Li, C. Kim, P. Kellnhofer, and W. Matusik, “Towards real-time photorealistic 3d holography with deep neural networks,” *Nature*, vol. 591, no. 7849, pp. 234–239, 2021.

[179] Y. Peng, S. Choi, N. Padmanaban, and G. Wetzstein, “Neural holography with camera-in-the-loop training,” *ACM Transactions on Graphics*, vol. 39, no. 6, pp. 1–14, 2020.

[180] T. Pitkäaho, A. Manninen, and T. J. Naughton, “Focus prediction in digital holographic microscopy using deep convolutional neural networks,” *Applied Optics*, vol. 58, no. 5, p. A202, 2019.

[181] T. Liu, K. de Haan, B. Bai, Y. Rivenson, Y. Luo, H. Wang, D. Karalli, H. Fu, Y. Zhang, J. FitzGerald, and A. Ozcan, “Deep learning-based holographic polarization microscopy,” *ACS Photonics*, vol. 7, no. 11, pp. 3023–3034, 2020.

[182] T. Liu, Z. Wei, Y. Rivenson, K. Haan, Y. Zhang, Y. Wu, and A. Ozcan, “Deep learning-based color holographic microscopy,” *Journal of Biophotonics*, vol. 12, p. 11, 2019.

[183] Z. Luo, A. Yurt, R. Stahl, A. Lambrechts, V. Reumers, D. Braeken, and L. Lagae, “Pixel super-resolution for lens-free holographic microscopy using deep learning neural networks,” *Optics Express*, vol. 27, no. 10, p. 13581, 2019.

[184] G. David, K. Esat, I. Thanopulos, and R. Signorell, “Digital holography of optically-trapped aerosol particles,” *Communications Chemistry*, vol. 1, p. 46, 2018.

[185] S.-J. Kim, C. Wang, B. Zhao, H. Im, J. Min, H. J. Choi, J. Tadros, N. R. Choi, C. M. Castro, R. Weissleder, H. Lee, and K. Lee, “Deep transfer learning-based hologram classification for molecular diagnostics,” *Scientific Reports*, vol. 8, p. 1, 2018.

[186] R. Horisaki, R. Takagi, and J. Tanida, “Deep-learning-generated holography,” *Applied Optics*, vol. 57, no. 14, p. 3859, 2018.

[187] M. H. Eybposh, N. W. Caira, M. Atisa, P. Chakravarthula, and N. C. Pégard, “DeepCGH: 3D computer-generated holography using deep learning,” *Optics Express*, vol. 28, pp. 26636–26650, 2020.

[188] J. Lee, J. Jeong, J. Cho, D. Yoo, B. Lee, and B. Lee, “Deep neural network for multi-depth hologram generation and its training strategy,” *Optics Express*, vol. 28, no. 18, p. 27137, 2020.

[189] E. Yüce, J. Lian, S. Sokolov, J. Bertolotti, S. Combrié, G. Lehoucq, A. D. Rossi, and A. P. Mosk, “Adaptive control of necklace states in a photonic crystal waveguide,” *ACS Photonics*, vol. 5, no. 10, pp. 3984–3988, 2018.

CURRICULUM VITAE

ALİM YOLALMAZ

Education

Ph. D., Micro and Nanotechnology Program, Graduate School of Natural and Applied Science, Middle East Technical University, Ankara/Turkey (Sept. 2017 – Feb. 2022)

Thesis title:	Spectral and spatial control of broadband light using wavefront shaping
Advisor:	Assoc. Prof. Dr. Emre Yüce
Scholarship:	100-2000 Ph.D. Scholarship by Higher Education Council of Turkey
Group activities:	Supervision of B.Sc., M.Sc., and Ph.D. students Construction of our research lab

M. Sc., Micro and Nanotechnology Program, Graduate School of Natural and Applied Science, Middle East Technical University, Ankara/Turkey (Sept. 2014 – Aug. 2017)

Thesis title:	Utilization of fiber loop ring down (FLRD) technique for sensing applications
Advisor:	Assoc. Prof. Dr. M. Fatih Danışman
Scholarship:	Research funding for development of fiber loop ring down spectrometer for trace chemical detection by the Scientific and Technological Research Council of Turkey with COST-Action TD1105 EuNetAir (Project No: 212T079)
Group activities:	Supervision of B.Sc. and M.Sc. students

B. Sc., Mechanical Engineering (Double major), University of Gaziantep, Gaziantep/-

Turkey (Sept. 2010 – Aug. 2013)

B. Sc., Physics Engineering, University of Gaziantep, Gaziantep/Turkey (Sept. 2007 – June 2012)

B. Sc. (Erasmus), Applied Physics, Gdansk University of Technology, Gdansk/Poland (Feb. 2012 – June 2012)

Professional Experience

Research and Teaching Assistant, Department of Mechanical Engineering, Turkish-German University, İstanbul/Turkey (April 2017 – Sept. 2017)

Achievements & Awards

2019	Project funding for 6 months research study by the Scientific and Technological Research Council of Turkey (Program no: 2214/A)
2018	2211/A Ph.D. Fellowship by the Scientific and Technological Research Council of Turkey
2017	M. Sc. Thesis of the Year Award by Middle East Technical University Graduate School of Natural and Applied Sciences
2012	Graduate with first place in the Department of Physics Engineering
2012	Graduate with second place among 539 students in Engineering Faculty
2008-2012	Honor/High honor student within all undergraduate semesters

Refereeing activity

Journal of Applied Optics
Optics and Laser Technology
Scientific Reports

Computer Skills

Programming languages: C++, Python, MATLAB, LabView, C++ Builder, Wolfram Mathematica 8

CAD skills: Sketchup, AutoCAD, SolidWorks

Computer operating systems: macOS, Windows, Linux, CentOS

Others: MS Office, Origin 8.5, Gaussian, Zemax, Centaurus TCAD, ProEngineer, Ansys, XPS Peak Analysis, Photoshop, Arduino.

Memberships

Chamber of Mechanical Engineers

Member of First-Aid Society at Middle East Technical University

Member of Optical Society of America Student Chapter

Hobbies/Interests

Cooking, Chess, Puzzle, Hiking, Tennis, and Music.

SCIENTIFIC ACTIVITY

Publications

1. A. Yolalmaz, E. Yüce, “Comprehensive deep learning model for 3D color holography,” Scientific Reports **12**, 2487 (2022)

2. A. Yolalmaz, E. Yüce, “Hybrid design of spectral splitters and concentrators of light for solar cells using iterative search and neural networks,” Photonics and Nanostructures – Fundamentals and Applications **48**, 100987 (2022)

3. A. Yolalmaz, E. Yüce, “Spectral splitting and concentration of broadband light using neural networks,” APL Photonics **6**, 046101 (2021)

4. Ö. E. Aşırım, A. Yolalmaz, “Design of ultra-high gain optical micro-amplifiers via smart non-linear wave mixing,” Progress in Electromagnetic Research B **89**, 177-194 (2020)

5. Ö. E. Aşırım, A. Yolalmaz, M. Kuzuoğlu, “High-fidelity harmonic generation in optical-resonators using BFGS algorithm,” Micromachines **11**, 7, 686 (2020)

6. A. Yolalmaz, E. Yüce, “Effective bandwidth approach for spectral splitting of solar spectrum using diffractive optical elements,” Optics Express **28**, 9, 12911-12921 (2020)

7. A. Yolalmaz, M. F. Danışman, O. Esentürk, “Discrimination of chemicals via refractive index by EF-FLRD,” Applied Physics B **125**, 156 (2019)

8. A. Yolalmaz, F. H. Sadroud, M.F. Danışman, O. Esentürk, “Intracavity gas detection with fiber loop ring down spectroscopy,” Optics Communication **396**, 141-145 (2017)

Publication in preparation

1. A. Yolalmaz, E. Yüce, “Hyperspectral imaging through a multi-mode fiber,” in preparation

Patents

1. E. Yüce, B. N. Gün, A. Yolalmaz, "Phase control of light via digital micro-mirror device," Turkish Patent 2021-GE (Pending)

2. E. Yüce, A. Yolalmaz, Ç. A. Yüksel, "Optical spectrometer based on changeable diffractive optical elements," Turkish Patent 2020-GE-288969 (Pending)

Conference Proceedings

1. A. Yolalmaz, E. Yüce, "Angle-independent diffractive optical elements for efficient solar energy conversion," SPIE Proceedings Volume 11366, Photonics for Solar Energy Systems VIII; 113660Q (2020)

2. A. Yolalmaz, E. Yüce, "Designs of diffractive optical elements for solar energy harvesting," 2019 Conference on Power Generation Systems and Renewable Energy Technologies (PGSRET) 1-5 (IEEE, 2019)

Oral Presentations

1. A. Yolalmaz, "Deep learning-based spectral splitting and concentration of broadband light for solar cells applications," 2nd International Conference on Photovoltaic Science and Technologies, Ankara/Turkey (2020)

2. A. Yolalmaz, "Angle-independent diffractive optical elements for efficient solar energy conversion," SPIE Photonics Europe, France (2020)

3. A. Yolalmaz, "Designs of diffractive optical elements for solar energy harvesting," 2019 International Conference on Power Generation Systems and Renewable Energy Technologies (PGSRET), Istanbul Technical University, İstanbul/Turkey (2019)

Poster Presentations

1. A. Yolalmaz, E. Yüce, "Patterning the sunlight with diffractive optical elements for the lateral architecture of the solar cells," Photonics-2019, İstanbul/Turkey (2019)

2. O. Orakcı, A. Yolalmaz, E. Yüce, "Spatial concentration of light via diffractive optical elements powered by deep learning," Photonics-2019, İstanbul/Turkey (2019)

3. A. Yolalmaz, O. Esentürk, M. F. Danışman, F. H. Sadroud, “Fiber loop ring down spectrometer – optical-based sensor for trace chemical detection,” 14th IUVSTA School on Nano-Optics, Braga/Portugal (2016)

4. A. Yolalmaz, O. Esentürk, M. F. Danışman, “Chemical detection at 800 nm with fiber loop ring down technique,” Photonics-2015, Ankara/Turkey (2015)

5. A. Yolalmaz, F. H. Sadroud, O. Esentürk, M. F. Danışman, “Trace chemical detection with 1535 nm wavelength laser,” Photonics-2015, Ankara/Turkey (2015)

6. A. Yolalmaz, F. H. Sadroud, M. F. Danışman, O. Esentürk, “Fiber loop ring down spectrometer for chemical sensing,” NanoTr-2015, Ankara/Turkey (2015)

7. A. Yolalmaz, E. Torun, M. F. Danışman, O. Esentürk, “Taper-based fiber loop ring down spectrometer for chemical detection with high sensitivity,” NanoTr-2015, Ankara/Turkey (2015)

Projects

1. Project title: Wavefront shaping and light scattering in complex media with applications in, e.g., the enhancement of conversion efficiencies of solar cells

Principal Investigator in the project financially funded by the Scientific and Technological Research Council of Turkey (program no: 2214-A)

2. Project title: Enhancement of conversion efficiency of solar cells using spectral splitting and wavefront shaping

Scientific researcher in the project financially funded by the Scientific and Technological Research Council of Turkey (project no: 118F075)

3. Project title: Multimode fiber-based spectrometer using wavefront shaping

Scientific researcher in the project financially funded by the Scientific and Technological Research Council of Turkey (project no:118M199)

4. Project title: Development of a scanning confocal microscopy

Scientific researcher in Industrial innovation project funded by Nanomagnetics Incorporation

5. Project title: Development of fiber loop ring down spectrometer for trace chemical detection

Scientific researcher in the project financially funded by the Scientific and Technological Research Council of Turkey with COST-Action TD1105 EuNetAir (project no: 212T079)